



# **Politecnico di Torino**

## **Investigation of Wellbore stability in a Horizontal well drilled in interbedded Sandstone Reservoir of Zubair Field**

**Advisor:** Professor. Deangeli Chiara

**Second Advisor:** Ahmed Al-Hajaj

**By**

**JAWAD KADHIM DAWOOD**

The Thesis submitted to Politecnico Di Torino University in partial fulfilment of the requirements for the Master of Science in Petroleum and Mining Engineering.

Academic Year 2020

## **ABSTRACT**

Drilling a well in safe and cost-effective manner is the main target of drilling engineers. Thus, wellbore stability, especially in highly deviated and horizontal wells, is the major obstacle in well design and, consequently, investing in many oil and gas fields around the world. These impediments are varied, such as lack of hole cleaning due to accumulation of splintered, blocky or tabular fragments, hydraulic hammers, tight holes, pipe sticking, lost circulation, poor cementing, sand production, reservoir compaction, surface subsidence and many others. All these problems may cause a significant increase in nonproductive time of drilling or production.

The purpose of this thesis is to determine the safe mud window for a proposed horizontal well in one of the most stressful fields in the southern part of Iraqi oil fields. The study is based on real data of eleven wells, here a parameters were implemented depending on the data of Triaxial and Brazilian tests of four wells that have been drilled in Zubair field. On the other hand, a dynamic model was employed in order to determine the rock mechanical strength parameters along the entire wellbore. After running the dynamic and static models, a matching has been carried out to define the uncertainty. Further, one of the most important considerations that was taken into account is the selection of an appropriate mechanical failure criterion.

Formation pressures play a major role in any geomechanics study. Accordingly, direct method was used to determine the pore pressure in the permeable formations, while indirect techniques were exploited to define the pore pressure in impermeable lithologies. Subsequently, the geomechanical model was built by Schlumberger's Techlog to determine the mud window for a horizontal well. Finally, due to the uncertainty in some results of log derived parameters, probabilistic analysis was performed by using Monte Carlo method to create a more realistic study.

## ACKNOWLEDGEMENT

I would like to extend my sincere thanks to everyone who contributed in the accomplishment of this work and who inspired and gave me self-confidence. First and foremost, I would like to thank my advisor Professor DEANGELI CHIARA who helped me a lot. Without her assistance and valuable suggestions, the thesis could not have been written in this way. Special thanks to Mr. Ahmed Alhajaj for his collaboration with Professor DEANGELI. He provided and authorized using field data, so all respect and appreciation to this honorable person.

I am eternally grateful to the Iraqi Ministry of Oil and Basra Oil Company for their sponsorship and assistance during my study. Special thanks to Zubair field division (ZFOD/Eni) who allowed use of the field data.

Profound gratitude to my family, who have been patient for the duration of my academic journey to Europe and my absence from them for a long period of time. Many thanks and appreciation to all my colleagues who encouraged me to achieve my postgraduate studies, Shaban Dharb Shaban, Haider Kadhim, Ali Hasim, Hazim Sabah, Maher Faleh and many others who are not mentioned.

I cannot forget the favor offered by the Lead Well Designer in Halliburton, Doaa Albaaji, who helped me to use the Landmark software.

My deepest gratitude to the Production and Well Integrity Engineer in Schlumberger, Teba Majeed Alsuraafi. She made every effort to obtain an official license from Schlumberger for using the Techlog 2020.1 software.

Great credit regarding completion of this work belongs to a PhD candidate in Swansea University-UK, "Wafaa Abd Al-Ameer". She encouraged and inspired me to choose this topic and provided me with many precious academic papers. Last but not least, special thanks go to all my classmates, in particular Ahmed Mousa Alnaji, who was next to me whenever I needed him.

# TABLE OF CONTENTS

<b>ABSTRACT</b> .....	<b>I</b>
<b>ACKNOWLEDGEMENT</b> .....	<b>II</b>
<b>TABLE OF CONTENTS</b> .....	<b>III</b>
<b>LIST OF ILLUSTRATIONS</b> .....	<b>V</b>
<b>LIST OF TABLES</b> .....	<b>IX</b>
<b>NOMENCLATURES</b> .....	<b>X</b>
<b>INTRODUCTION TO WELLBORE STABILITY</b> .....	<b>1</b>
1.1 Objective of the Study .....	1
1.2 Geological and Tectonic Background of Zubair Field .....	1
1.3 Available data of Zubair Field .....	3
1.4 Mechanical Earth Model Flowchart .....	7
<b>LITERATURE REVIEW</b> .....	<b>8</b>
2.1 In situ stresses .....	8
2.1.1 Geostatic Vertical Stress .....	10
2.1.2 Geostatic Horizontal Stresses .....	11
2.2 Pore Pressure .....	16
2.2.1 Normal Compaction Trend (NCT).....	17
2.2.2 Eaton Method.....	18
2.2.3 Holbrook Method.....	18
2.3 Rock mechanical strength and deformation. ....	19
2.3.1 Theory of Elasticity & Biot Coefficient.....	20
2.3.2 Tensile strength (To).....	24
2.3.3 Uniaxial (Unconfined) Compressive Strength.....	25
2.3.4 Shear strength parameters (cohesion, friction angle).....	26
<b>ROCK FAILURE CRITERIA</b> .....	<b>28</b>
3.1 Mohr-Coulomb .....	28
3.2 Hoek-Brown .....	30
3.3 Weakness Plane Model (Jaeger, 1960).....	31
3.4 Mogi-Coulomb .....	32
3.5 Stresses around a wellbore .....	34
3.5.1 Lamé Solution.....	35
3.5.2 Kirsch Solution .....	36
<b>RESULTS AND DISCUSSIONS OF WELLBORE STABILITY ANALYSIS</b> .....	<b>38</b>
4.1 Model Parameters .....	38
4.1.1 Overburden stress calculations .....	38
4.1.2 Pore Pressure Estimation .....	40
4.1.3 Young’s modulus prediction.....	42
4.1.4 Poisson’s ratio estimation .....	44
4.1.5 Evaluation of Uniaxial Compressive Strength.....	45
4.1.6 Friction angle & Cohesion prediction.....	45
4.1.7 Tensile Strength assessment .....	47
4.1.8 Horizontal stresses calculation by Poro-Elastic Horizontal strain model	48
4.1.9 Horizontal stresses prediction by Mohr-Coulomb stress .....	50

4.1.10 Maximum Horizontal stress from frictional faulting theory.....	51
4.2 Direction of Horizontal stresses .....	53
4.3 Wellbore stability analysis with Mohr-Coulomb criterion.....	56
4.3.1 Stability analysis with Mohr-Coulomb at Dammam .....	58
4.3.2 Stability analysis with Mohr-Coulomb at Hartha formation .....	60
4.3.3 Stability analysis with Mohr-Coulomb at Tanuma & Khasib .....	62
4.3.4 Stability analysis with Mohr-Coulomb at Mishrif formation .....	64
4.3.5 Stability analysis with Mohr-Coulomb at Nahr Umr.....	66
4.3.6 Stability analysis with Mohr-Coulomb at Zubair formation.....	68
4.4 Wellbore stability analysis with Mogi-Coulomb criterion.....	70
4.4.1 Stability analysis with Mogi versus Mohr at Dammam.....	72
4.4.2 Stability analysis with Mogi versus Mohr at Hartha .....	74
4.4.3 Stability analysis with Mogi versus Mohr at Tanuma and Khasib Formations .....	76
4.4.4 Stability analysis with Mogi versus Mohr at Mishrif .....	78
4.4.5 Stability analysis with Mogi versus Mohr at Nahr Umr .....	80
4.4.6 Stability analysis with Mogi versus Mohr at Zubair.....	82
4.5 Wellbore stability analysis with Drucker-Prager criterion.....	83
4.6 Wellbore stability analysis with Stassi d'Alia Criterion .....	86
4.7 Horizontal Well Design .....	87
4.7.1 Well Trajectory .....	87
4.7.2 Equevalent circulation density in 12.25" hole section.....	88
4.7.3 Equevalent circulation density in 8.5" hole section.....	89
<b>CONCLUSIONS, RECOMMENDATIONS AND FUTURE WORK .....</b>	<b>91</b>
5.1 Conclusions and recommendations .....	91
5.2 Future Work.....	93
<b>REFERNCES .....</b>	<b>94</b>
<b>APPENDIX A: STRESS POLYGON OF TANUMA FORMATION.....</b>	<b>99</b>
<b>APPENDIX B: STRESS POLYGON OF MIDDLE SHALE FORMATION .....</b>	<b>101</b>

## LIST OF ILLUSTRATIONS

Figure 1. 1 Map shows the location of Zubair field and upper sandstone reservoir structural map (Al-Jafar and Al-Jaberi 2019). .....	1
Figure 1. 2 Faults network of (a) Cretaceous and (b) Jurassic (Geophysical Support 2013 and 2014 Seismic Horizons Interpretation, Field data). .....	2
Figure 1. 3 Faults network of (a) Cretaceous and (b) Jurassic (Geophysical Support 2013 and 2014 Seismic Horizons Interpretation, Field data)(a) .....	2
Figure 1. 4 MEM Workflow of proposed Horizontal Well. $\alpha$ .....	7
Figure 2. 1 Anderson’s Fault Classifications. adapted from (Vavryčuk 2014).....	8
Figure 2. 2 Frictional Faulting Theory (Markou and Papanastasiou 2018). .....	9
Figure 2. 3 Fracture orientation in the direction of maximum Horizontal stress, Image adapted from reference (Lin et al. 2018). .....	11
Figure 2. 4 Leak of Test Scheme (Raaen et al. 2006).....	12
Figure 2. 5 Various directions of wellbore and stress states (Aadnøy and Looyeh 2011). .....	13
Figure 2. 6 Natural Fracture on FMI, Resistivity and UBI. (b) 3D oriented caliper log. (c) Break out on FMI (Bailey et al., 2015, Field data).....	15
Figure 2. 7 Formation of fast and slow axes of shear wave (Ezati and Soleimani 2014). .....	16
Figure 2. 8 Normal compaction trend in Interval Transit Times versus Depth (Das and Mukherjee 2020).....	17
Figure 2. 9 The effect of flow direction on the fabric of rocks (MACAULAY et al. 2016). .....	20
Figure 2. 10 (a) Young’s modulus in stress strain relationship. (b) Axial & Radial strain - uniaxial stress, Images adapted from reference (Fjaer et al. 2008). .....	21
Figure 2. 11 Shear Modulus. (b) Bulk Modulus, images adapted from reference (environment.uwe.ac.uk/geocal/SoilMech/basic/stiffness.htm). .....	22
Figure 2. 12 Unloading-reloading round in static lab test (Fjaer et al., 2008).....	23
Figure 2. 13 Direct tensile test, (b) Brazilian test, images adapted from reference (Claesson and Bohloli 2002).....	24
Figure 2. 14 The concept of Friction angle, Images adapted from reference ( <a href="https://slideplayer.com/slide/5865222/">https://slideplayer.com/slide/5865222/</a> ). .....	27
Figure 3. 1 Shear stress and failure plane, adapted from (Bewick, Kaiser, and Amann 2019).....	28
Figure 3. 2 Mohr-Coulomb, (a) Shear stress and effective normal stress relationship, (b) Principal stress and UCS & UTS in the Mohr-Coulomb criterion envelope, figures adapted from reference (Zhang et al. 2015).....	29
Figure 3. 3 TXT at different bedding plane inclination: Experimental data (symbols), H&B (Solid lines) and dotted lines are weakness plane (Deangeli and Omwanghe 2018). .....	30
Figure 3. 4 (a), Weakness plane in TXT specimen, (b) Weakness plane model envelope, Shapes adapted from reference (Zhang et al. 2015).....	31

Figure 3. 5 TXT and Poly axial test data in $\tau_{oct}$ $\sigma_{oct}$ space to determine <i>a</i> and <i>b</i> , Image adapted from reference (Al-Ajmi and Zimmerman 2006).....	33
Figure 3. 6 Stresses distribution around wellbore and far field stresses in cylindrical coordinates, figure adapted from reference (Eide, H.S. 2012). .....	34
Figure 3. 7 Stresses distribution around wellbore for constant pore pressure in linear elastic rock, Shapes adapted from reference (Fjær et al., 2008). .....	35
Figure 3. 8 Stresses distribution around wellbore and far field stresses according to Kirsch Solution, Images adapted from reference (Wang et al. 2019).....	36
Figure 4. 1 Integrated Overburden stress, calculated based on bulk density log of Zubair field, Published with Techlog 2020.1.1.....	39
Figure 4. 2 Pore Pressure calculation according to Eaton’s Resistivity and Slowness logs, Published with Techlog 2020.1.1. ....	41
Figure 4. 3 Young’s modulus prediction, Published with Techlog 2020.1.1. ....	43
Figure 4. 4 Poisson’s ratio estimation, Published with Techlog 2020.1.1. ....	44
Figure 4. 5 UCS, Friction angle and cohesion prediction, Published with Techlog 2020.1.1.....	46
Figure 4. 6 Tensile strength, Published with Techlog 2020.1.1. ....	47
Figure 4. 7 Horizontal stresses in Poro-Elastic Horizontal strain model, Published with Techlog 2020.1.1. ....	49
Figure 4. 8 Horizontal stresses prediction by Mohr-Coulomb stress model, Published with Techlog 2020.1.1. ....	50
Figure 4. 9 Stress Polygon of Tanuma formation at 2224 m, Published with MATLAB® R2019b.....	51
Figure 4. 10 Stress Polygon of middle shale formation at 3376 m, Published with MATLAB® R2019b.....	52
Figure 4. 11 Stress map of Zubair field and surrounding area (World Stress Map Rel.2008).....	53
Figure 4. 12 FMI processing and horizontal stresses directions, processing at 12.25” hole section ZB-227, Published with Techlog 2020.1.1.....	54
Figure 4. 13 FMI processing and horizontal stresses directions, processing at 8.5” hole section, Published with Techlog 2020.1.1. ....	55
Figure 4. 14 Wellbore stability analysis with Mohr-Coulomb criterion Published with Techlog 2020.1.1. ....	57
Figure 4. 15 Wellbore stability analysis with Mohr-Coulomb criterion at Dammam formation, Published with Techlog 2020.1.1.....	58
Figure 4. 16 Sensitivity analysis with Mohr Coulomb criterion at Dammam formation, Published with Techlog 2020.1.1.....	59
Figure 4. 17 Wellbore stability analysis with Mohr-Coulomb criterion at Hartha formation, Published with Techlog 2020.1.1.....	60
Figure 4. 18 Sensitivity analysis with Mohr-Coulomb criterion at Hartha formation, Published with Techlog 2020.1.1.....	61
Figure 4. 19 Wellbore stability analysis with Mohr-Coulomb criterion at Tanuma and Khasib formation, Published with Techlog 2020.1.1. ....	62
Figure 4. 20 Sensitivity analysis with Mohr-Coulomb criterion at Tanuma and Khasib formations, Published with Techlog 2020.1.1. ....	63

Figure 4. 21 Wellbore stability analysis with Mohr-Coulomb criterion at Mishrif formation, Published with Techlog 2020.1.1.....	64
Figure 4. 22 Sensitivity analysis with Mohr-Coulomb criterion at Mishrif formations, Published with Techlog 2020.1.1.....	65
Figure 4. 23 Wellbore stability analysis with Mohr-Coulomb criterion at Nahr Umr formation , Published with Techlog 2020.1.1.....	66
Figure 4. 24 Sensitivity analysis with Mohr-Coulomb criterion at Nahr Umr formations, Published with Techlog 2020.1.1. ....	67
Figure 4. 25 Wellbore stability analysis with Mohr-Coulomb criterion at Zubair members formation, Published with Techlog 2020.1.1. ....	68
Figure 4. 26 Sensitivity analysis with Mohr-Coulomb criterion at Zubair members formations, Published with Techlog 2020.1.1. ....	69
Figure 4. 27 Wellbore stability analysis with Mogi-Coulomb criterion versus Mohr Coulomb criterion, Published with Techlog 2020.1.1. ....	71
Figure 4. 28 Wellbore stability analysis with Mogi-Coulomb versus Mohr Coulomb criterion in Dammam formation, Published with Techlog 2020.1.1. ....	72
Figure 4. 29 Sensitivity analysis with Mogi-Coulomb versus Mohr Coulomb criterion in Dammam formation, Published with Techlog 2020.1.1.....	73
Figure 4. 30 Wellbore stability analysis with Mogi-Coulomb versus Mohr Coulomb criterion in Hartha formation (Techlog). ....	74
Figure 4. 31 Sensitivity analysis with Mogi-Coulomb versus Mohr Coulomb criterion at Hartha formation, Published with Techlog 2020.1.1.....	75
Figure 4. 32 Wellbore stability analysis with Mogi-Coulomb versus Mohr Coulomb in Tanuma and Khasib formation, Published with Techlog 2020.1.1.....	76
Figure 4. 33 Sensitivity analysis with Mogi-Coulomb versus Mohr Coulomb criterion at Tanuma and Khasib formation, Published with Techlog 2020.1.1.....	77
Figure 4. 34 Wellbore stability analysis with Mogi-Coulomb versus Mohr Coulomb criterion in Mishrif formation, Published with Techlog 2020.1.1.....	78
Figure 4. 35 Sensitivity analysis with Mogi-Coulomb versus Mohr Coulomb criterion at Mishrif formation, Published with Techlog 2020.1.1.....	79
Figure 4. 36 Wellbore stability analysis with Mogi-Coulomb versus Mohr Coulomb criterion in Nahr Umr formation, Published with Techlog 2020.1.1.....	80
Figure 4. 37 Sensitivity analysis with Mogi-Coulomb versus Mohr Coulomb criterion at Nahr Umr formation, Published with Techlog 2020.1.1.....	81
Figure 4. 38 Wellbore stability analysis with Mogi-Coulomb versus Mohr Coulomb in Zubair members formation, Published with Techlog 2020.1.1. ....	82
Figure 4. 39 Sensitivity analysis with Mogi-Coulomb versus Mohr Coulomb criterion at Zubair members formation, Published with Techlog 2020.1.1.....	83
Figure 4. 40 Wellbore stability analysis with Drucker-Prager (circumscribed) versus Mogi Coulomb-Criterion, Published with Techlog 2020.1.1. ....	84
Figure 4. 41 Wellbore stability analysis with Drucker-Prager (inscribed) versus Mogi Coulomb-Criterion, Published with Techlog 2020.1.1.....	85
Figure 4. 42 Wellbore stability analysis with Stassi d'Alia versus Mogi-Coulomb Criterion, Published with Techlog 2020.1.1. ....	86
Figure 4. 43 Wellbore trajectory of Horizontal Well, Published with Landmark 5000.15.....	87

Figure 4. 44 Equivalent circulation density versus depth in 12.25", Published with Landmark 5000.15 .....	88
Figure 4. 45 Equivalent circulation density versus trip time close ended in 12.25", Published with Landmark 5000.15 .....	89
Figure 4. 46 Equivalent circulation density versus depth in 8.5", Published with Landmark 5000.15 .....	90
Figure 4. 47 Equivalent circulation density versus trip time close ended in 8.5", Published with Landmark 5000.15 .....	90

## LIST OF TABLES

Table 1 Available data of Zubair Field .....	3
Table 2. 1 Parameters used to determine pore pressure in Holbrook technique .....	19
Table 4. 1 Shear failure equations in vertical well based on Mohr Coulomb.....	56
Table 4. 2 Tensile failure equations in vertical well based on Mohr Coulomb .....	56
Table 4. 3 Shear failure equations in vertical well based on Mogi Coulomb.....	70
Table 4. 4 Tensile failure equations in vertical well based on Mogi Coulomb .....	70

## NOMENCLATURES

<b>Symbol</b>	<b>Meaning and unit</b>	<b>Symbol</b>	<b>Meaning and unit</b>
$C$	Formation cohesion (MPa)	$\sigma_1$	Major Principle Stress (MPa)
$E$	Young's modulus (GPa)	$\sigma_2$	Intermediate Principle stress (MPa)
$E_{dyn}$	Dynamic Young's modulus (GPa)	$\sigma_3$	Minor Principle stress (MPa)
$F$	Force, N (kg.m/s <sup>2</sup> )	$\sigma'$	Effective stress (MPa)
$F_n$	Normal force, N (kg.m/s <sup>2</sup> )	$\sigma_m$	Mean stress (MPa)
$F_s$	Parallel force, N (kg.m/s <sup>2</sup> )	$\sigma_n$	Normal Stress (MPa)
$G$	Shear modulus (GPa)	$\sigma_r$	Radial stress (MPa)
$G_{dyn}$	Dynamic shear modulus (GPa)	$\sigma_\theta$	Tangential stress (MPa)
$GR$	Gamma ray (gAPI)	$\sigma_z$	Axial Stress (MPa)
$g$	Gravitational acceleration (m/s <sup>2</sup> )	$\sigma_h$	Minimum Horizontal Stress (MPa)
$K$	Bulk modulus (GPa)	$\tau$	Shear Stress (MPa)
$K_{dyn}$	Dynamic Bulk modulus (GPa)	$\tau_{oct}$	Octahedral shear stress (MPa)
$P_{bg}$	Pore pressure gradient (MPa)	$\tau_{xy}$	shear stress in x-y plane (MPa)
$P_p$	Pore pressure (MPa)	$\tau_{xz}$	shear stress in x-z plane (MPa)
$P_w$	Wellbore pressure (MPa)	$\tau_{yz}$	shear stress in y-z plane (MPa)
$Sg$	Specific gravity (Unitless)	$\phi'$	Friction angle (deg)
$T_0$	Tensile strength (MPa)	$\emptyset$	Formation porosity (fraction)
$UCS$	Uniaxial compressive strength (MPa)	$\nu$	Poisson's ratio (Unitless)
$V_p$	Compressional-wave velocity (ft/sec)	$\sigma_H$	Maximum Horizontal Stress (MPa)
$V_s$	Shear-wave velocity (ft/sec)		
$Z$	Depth (ft)		
$Z_w$	Water depth (ft)		
$\alpha$	Biot's coefficient (Unitless)		
$\beta$	Coefficient of compaction strain-hardening (Unitless)		
$\beta_w$	Weakness plane angle (deg)		
$\gamma$	Borehole inclination (deg)		
$\Delta t_{co}$	Compressional-wave slowness (μsec/ft)		
$\Delta t_s$	Shear-wave slowness (μsec/ft)		
$\rho$	Bulk density (g/cm <sup>3</sup> )		
$\rho_w$	Water density (g/cm <sup>3</sup> )		
$\sigma$	Stress (MPa)		
$\sigma_v$	Vertical Stress (MPa)		

## Introduction to Wellbore Stability

### 1.1 Objective of the Study

Zubair has been producing oil and gas for more than fifty years. Thus, horizontal wells might help to increase production as a potential method to enhance the oil recovery and minimize the water cut phenomenon. Various service companies have therefore attempted to drill highly deviated and horizontal wells in Zubair field, but have faced many difficulties. The main reason was the absence of comprehensive geomechanical studies on this field despite the availability of data. On the other side, the geological and tectonic structure is rather complex, and affected as well by the existence of long shale sections extending from the surface layers until the production zones. Moreover, most of the shale intervals are of mechanically and chemically stressed lithology. Therefore, all these drawbacks provided great incentive to investigate the essence of stresses and rock mechanics of that field. Hence, the purpose of this study is to deeply understand all the obstacles that are experienced in the field, and the implications for drilling highly deviated and horizontal wells at feasible costs. Accordingly, a mechanical earth model of the Zubair's region was constructed, which may help in the future to drill two or even three-dimensional well profiles.

### 1.2 Geological and Tectonic Background of Zubair Field

Zubair field is located about twenty kilometers to the west of Basrah city. It extends from the Iraqi-Kuwaiti border in the south to the north-west of the city. The

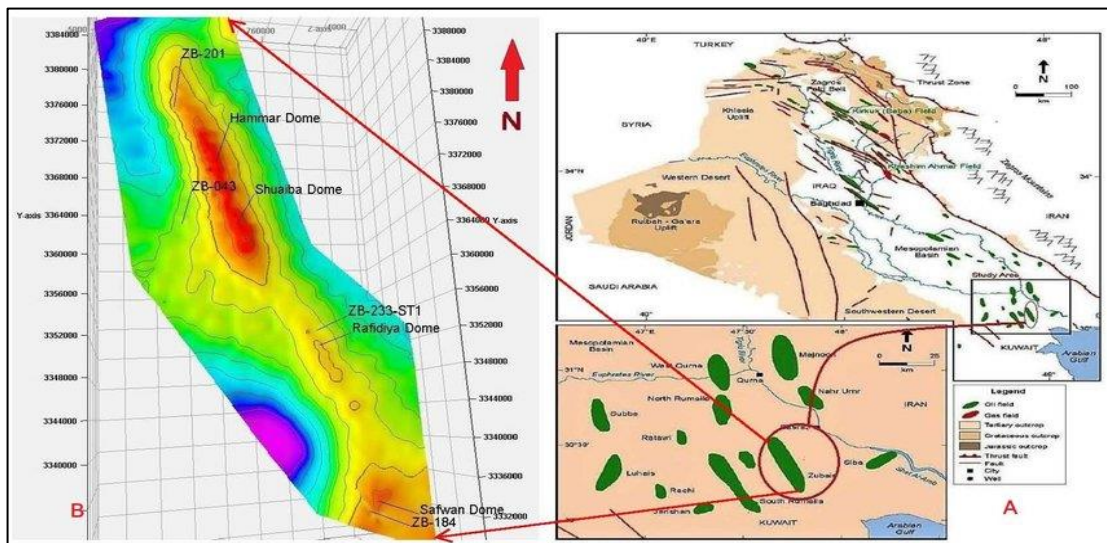


**Figure 1. 1 Map shows the location of Zubair field and upper sandstone reservoir structural map (Al-Jafar and Al-Jaberi 2019).**

region is the Sagged Basin of the *Mesopotamian* zone which is located in an unstable Arabian platform Figure 1.1. The structural analysis shows a symmetrical anticline and it is very flat. The anticline is slightly dipping (max dip angle:4-5°), over 60 km in length and about 10 km in width.

Oil traps were formed because of three reasons: The Alpine orogenic movement, salt tectonics (Hormuz salt structures), and reactivated basement faults. These three factors usually contribute together in the formation of subsurface anticline structures, and each of them may help the others (AL-Mutury and Al-Mayahi 2015). Zubair's structural aspects that are related to the tectonic activities probably are connected with the Zagros compressional phase. This is associated with the basement faults and fractures by which the field subsurface is bounded, Figure 1.2. Furthermore, there is significant difference in the shape, dimensions, displacement and density of the faults' structure between Jurassic and Cretaceous sequences of the field (Geophysical Support 2013 and 2014 Seismic Horizons Interpretation, Field data).

The general substructure of the field region is characterized by dissimilar anticline construction, where it is narrow in Jurassic and wider in Cretaceous. In addition, the distributions of faults are intensive in the middle of Jurassic, while there are few faults at the top, Figure 1.2 (Geophysical Support 2013 and 2014 Seismic Horizons Interpretation, Field data).

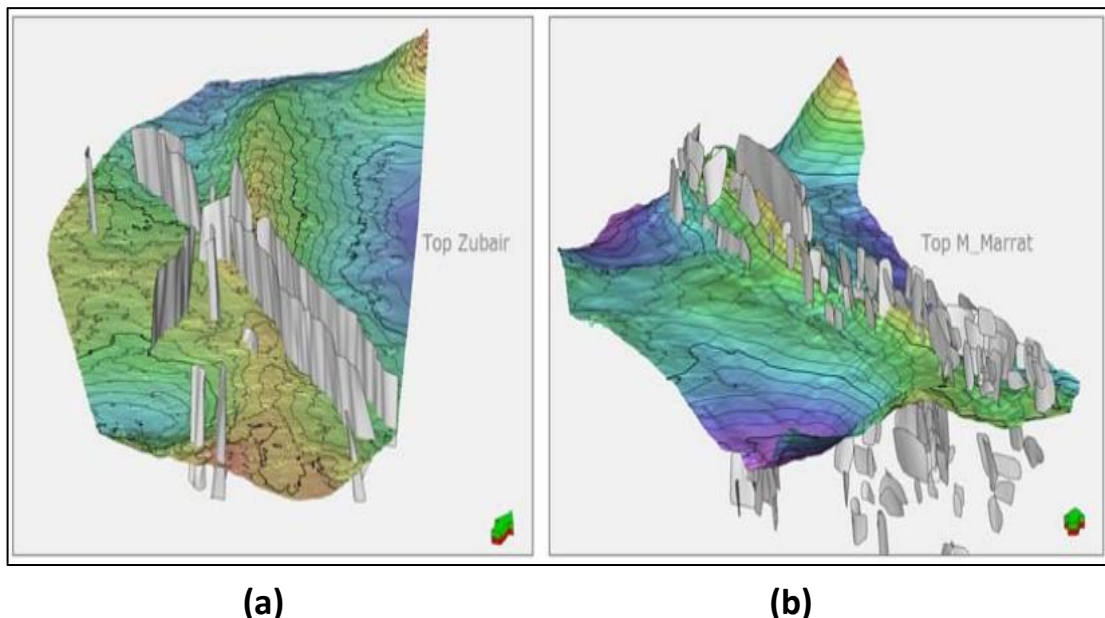


**Figure 1. 2 Faults network of (a) Cretaceous and (b) Jurassic (Geophysical Support 2013 and 2014 Seismic Horizons Interpretation, Field data).**

The existence of deformations in the middle Jurassic (Specifically in Qotnia Layer) are results of ductile flow of Evaporates. The salt layers are mainly composed of Halite and Anhydrite with minor streaks of (Limestone and Shale). Hormuz salt structure plays a major role in tectonic perturbations of the field. However, according to the recent studies and seismic interpretation, the salt structure outcrops into a salt dike creating “Jabal Sanam”. Where Jabal stands for mountain in Arabic language and Sanam is camel’s hump Figure 1.3 (a, b) (K. Sissakian et al. 2017).

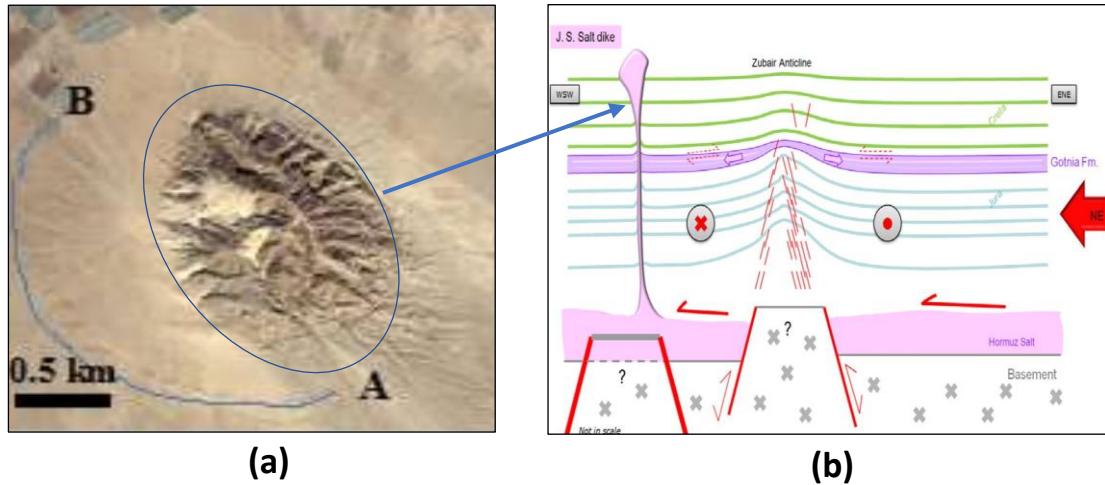


**Figure 1. 3 (a) Intruded Body, (b) Structure of field with outcrop. (Geophysical Support 2013 and 2014 Seismic Horizons Interpretation, Field data).**

It is fundamental that the stiffness of the salt (outcrop) and the adjacent rocks is different. This variation in stiffness makes the displacement not only in a vertical direction but also horizontally (Dusseault et al. 2004). Moreover, the salt interface cannot support shear stress, which causes reverberation of the stresses’ orientation from vertical and horizontal directions (D. Zoback 2007). For these reasons, the presence of “Jabal Sanam” may cause local perturbation and can influence the field stresses. Subsequently, neglecting the effect of the salt layer and the outcrop may lead to severe consequences in drilling operations. Therefore, the presence of these geological structures that surround the oil reservoirs has been discussed briefly.

### 1.3 Available data of Zubair Field

One of the most common obstacles that the engineers encounter when trying to write about the geomechanics of any oil field on the globe is finding sufficient accurate data. Even if these data are available, it is rare to find inclusive technical reports on one well. That is why the researchers may seek to collect these data from more than one well, and this may have a remarkable impact on the reliability of their study. This thesis

is based on taking advantage of the obtainable reports and records that are illustrated in table 1.1, where the quality of each single data set is defined.

**Table 1.1 Available data of Zubair Field.**

Data	Well Number										
	199	201	202	227	232	233	236	245	247	254	265
Daily Drilling Reports	Green	Green	Green	Green	Green	Green	Green	Green	Green	Green	Green
Mud Reports	Green	Green	Green	Green	Green	Green	Green	Green	Green	Green	Green
Master Logs	Green	Green	Green	Green	Green	Green	Green	Green	Green	Green	Green
Triaxial Tests	Yellow	Yellow	Red	Red	Yellow	Red	Red	Red	Red	Red	Red
Brazilian Tests	Yellow	Yellow	Red	Red	Yellow	Red	Red	Red	Red	Red	Red
Formation Micro Imager	Red	Red	Yellow	Yellow	Yellow	Yellow	Yellow	Red	Red	Yellow	Yellow
Density Logs	Red	Green	Green	Yellow	Green	Green	Yellow	Green	Green	Yellow	Yellow
Delta- T Compressional	Red	Green	Green	Green	Green	Green	Yellow	Green	Green	Yellow	Yellow
Delta- T Shear (DTSM)	Red	Green	Green	Red	Green	Yellow	Yellow	Green	Green	Yellow	Yellow
Pore Pressure points	Red	Red	Green	Green	Green	Green	Yellow	Green	Green	Yellow	Yellow
Hydraulic Fracturing	Red	Red	Red	Green	Red	Green	Red	Green	Green	Red	Red
Caliper Log	Red	Yellow	Green	Green	Green	Yellow	Yellow	Green	Green	Green	Green
Available in good quality > <span style="display: inline-block; width: 15px; height: 15px; background-color: #4CAF50; border: 1px solid black;"></span> Available in acceptable quality > <span style="display: inline-block; width: 15px; height: 15px; background-color: #FFEB3B; border: 1px solid black;"></span> Unavailable > <span style="display: inline-block; width: 15px; height: 15px; background-color: #F44336; border: 1px solid black;"></span>											

**Daily Drilling Reports:** DDRs are of indispensable importance in conducting any wellbore stability analysis. If the reports contain the entire details, they will be more valuable. Therefore, many of the symptoms that appear while drilling must be mentioned in the drilling reports. For instance, tight holes, torque and drag during tripping in or out, and manifestation of large quantities of shale fragments on shale shakers, may give indications of hole status. These hole problems can help in identifying the intervals which may suffer from mechanical stresses. Therefore, revising the reports may facilitate the achievement of better conclusions. Accordingly, information from DDRs of eleven vertical and inclined wells were rationally selected and utilized in this thesis.

**Mud Reports:** Drilling fluids have two impacts on rock strength. Firstly, the inconvenient design of mud properties in water-based mud (WBM) can influence the formation strength. For example, unsuitable fluid parameters such as fluid loss (API filtration), Cation exchange capacity (CEC), chlorides concentration and methylene blue test (MBT) can lead to water interaction between rocks and mud. On that account,

the water activity might give rise to hydration or dehydration when the exposure time of the rock is exceeded (Schlemmer et al. 2002).

The other influence is related to mud circulation which alters the bottom hole temperature. This temperature variations may result in shrinkage or expansion of the rocks (*thermoelasticity*), which in turn reform the rock strength (Fjaer et al. 2008). This topic is beyond the scope of this thesis, but reviewing the reports may help in comprehensively covering all the effects which may motivate the deterioration of rocks' mechanical specifications.

**Master Log:** This report provides extensive details about the rock lithology for almost every meter drilled. It is compiled in conjunction with Gamma ray (GR), continuous recording of penetration rate (ROP) and Sonic logs. These parameters (GR, ROP, sonic and Lithology) may help to evaluate or at least emphasize the measurement of unconfined rock strength which is assessed in dynamic and static models (Adebayo, Opafunso, and Akande 2010).

**Lab Test:** Due to the high cost of taking core samples, it is imperative that the oil companies take limited quantities at the depths at which the hydrocarbons exist. While most of the wellbore stability problems are in shale sections, oil companies rarely take core from this formation. This is the substantial stumbling block that researchers face. Therefore, triaxial and Brazilian tests of four wells in two intervals of different depths have been utilized in this study for the purpose of matching with log derived parameters. It is highlighted that the data of the Brazilian and Triaxial tests are in acceptable quality as illustrated in table 1.1. The reason is the integrity of rock samples and there was significant delay between core retrieving and lab tests.

**Formation Imager & Calliper Logs:** The formation imager is one of the most substantial logging tools. It is a multipurpose log that enables reservoir, production and drilling engineers as well as geologists to use the recorded data to design their wells and field. Geologists can use these tools to determine the dipping and orientation of layers and bedding planes, which is very crucial to locate the azimuth and inclinations of wells. While drilling and geomechanics engineers can use the data to define the directions of minimum and maximum horizontal stresses and finally optimize the wellbore trajectory. Thus, high resolution formation imager data from Schlumberger and Baker Hughes were exploited in construction of this study. Moreover, 4 arms caliper logs of some wells have been employed for model validation and to define the agreement between predicted failures and log status.

**Wire line logging data:** Density log, Delta-T Compressional (DTCO) and Delta-T Shear (DTSM), are the pioneer logging tools in geomechanics. They were used in calculating the subsurface stresses, as well as the rock's mechanical properties. The readings are continuous for hundreds of meters of drilled rock, so they have been utilized for inclusive design of the geomechanical model. On the other hand, the core measurements were somehow used for comparison objectives with log-derived strength parameters. Sometimes, gaps were diagnosed between the two models and the inconsistencies could be quite large for several reasons. These reasons will be discussed with details in the next chapters.

**Pore Pressure points (MDT, RDT):** The predicted pore pressure was validated according to the pressure points from nine wells of two production zones in sandstone and carbonate reservoirs. The pore pressure was measured by different tools such as Modular Dynamic Tools (MDT), Reservoir Description Tools (RDT) and Repeated Formation Tester (RFT). All pressure points were compared with the indirect methods which estimated a continuous profile of pore pressure from 569-3500 m.

**Hydraulic Fracturing data:** Hydraulic fracturing occurs when the confined mud pressure surpasses the combination of the least principal stress and rock tensile strength (Nauroy 2011). This concept can be exploited to determine the minimum horizontal stress. Therefore, Frac-jobs data of four wells were used as reference points to determine  $\sigma_h$  and calibrate the same with the log-derived continuous line of minimum horizontal stress.

# 1.4 Mechanical Earth Model Flowchart

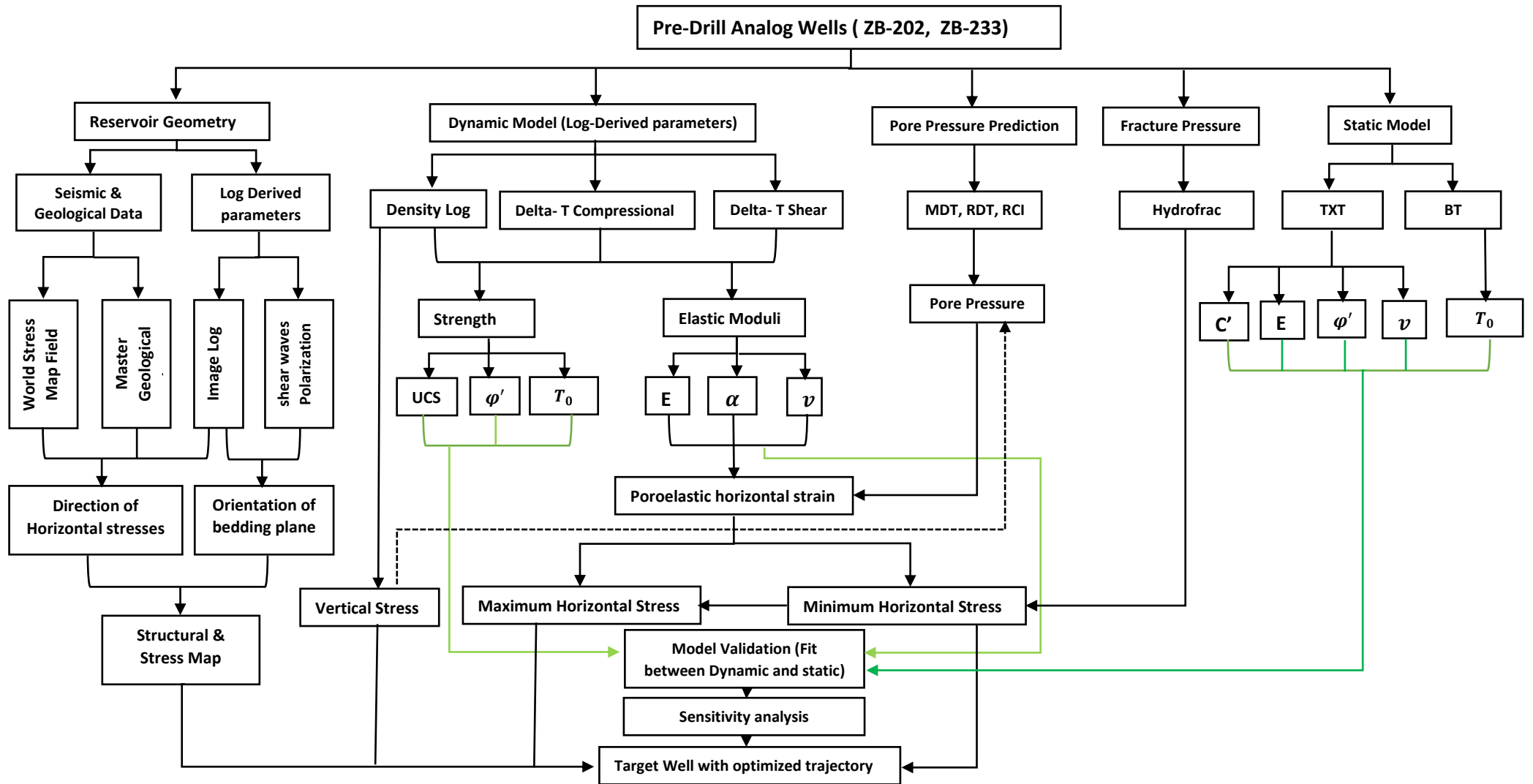


Figure 1. 4 MEM Workflow of proposed Horizontal Well.

## Literature Review

The subsurface conditions are governed by several complicated variables. These variables include stress path and geological history, tectonic activities, lateral heterogeneity of the rocks, topography and many others that have a powerful impact on the geomechanical parameters. Therefore, knowing these parameters and the situations that control them provides effective leverage in building a mechanical earth model as close as possible to the reality. In this chapter, all the features related to the wellbore stability and geomechanics are discussed with sufficient explanation.

### 2.1 In situ stresses

Mostly, the in-situ stresses are compatible with the vertical and horizontal directions. This concept can be utilized to classify the stresses into: 1. vertical stress and 2. horizontal stresses (Aadnøy and Looyeh 2011). In some regions, the geological structures are more troublesome due to the existence of salt domes, so the stresses distribution is radically dissimilar (Aadnøy and Looyeh 2011). Hence, based on Anderson classification, vertical stress can be greater or smaller than horizontal stresses. This aspect characterizes the type of fault that is currently active in the area of interest. There are three types of faulting regime as simplified in Figure 2.1: Normal fault (NF) when ( $\sigma_v > \sigma_H > \sigma_h$ ), Strike Slip fault (SSF) when ( $\sigma_H > \sigma_v > \sigma_h$ ), and Reverse Fault (RF) in case of ( $\sigma_H > \sigma_h > \sigma_v$ ).

As per frictional faulting theory, friction is the main player which determines the magnitude of stresses that are required to activate the fault and define the orientation of the fault's strike (Beeler, Hirth, and Thomas 2016).

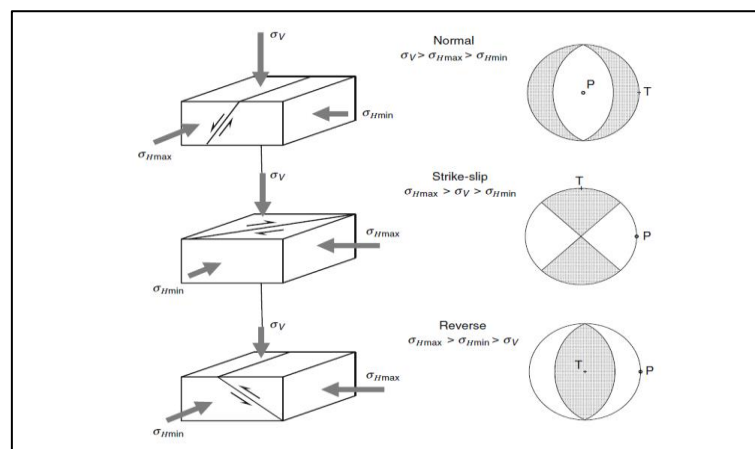


**Figure 2. 1 Anderson's Fault Classifications. Image adapted from (Vavryčuk 2014).**

Anderson's theory indicated that the fractures and faults are ruled by the Coulomb criterion, Figure 2.2. A fault is triggered when the difference in the effective principal stresses approaches Coulomb, and slip is supposed to be along the direction of the shear stress. Furthermore, the failure plane is normal on the intermediate principal stress (Celerier 2008).

$$\sigma_n = 0.5(\sigma_1 + \sigma_3) + 0.5(\sigma_1 - \sigma_3)\cos 2\beta \quad (2.1)$$

$$\tau = 0.5(\sigma_1 - \sigma_3)\sin 2\beta \quad (2.2)$$

Failure will happen where

$$\tau = C' + \mu\sigma_n \quad (2.3)$$

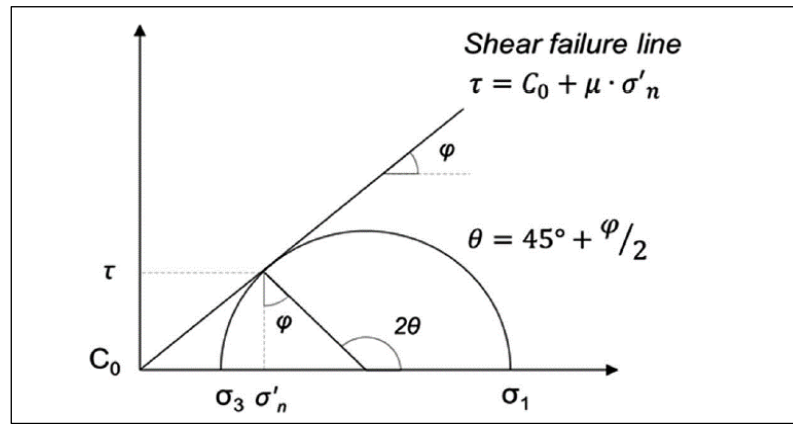


**Figure 2. 2 Frictional Faulting Theory (Markou and Papanastasiou 2018).**

There is another type of fault that does not fall within Anderson's categorization. This kind of fault occurs in the ground at a depth of more than thirty kilometers and is named oblique slip. It happens due to the coincidence of the horizontal and vertical movement. Vertical and horizontal motions take place simultaneously when the principal stresses are not coinciding with the vertical and horizontal directions (Celerier 2008).

On the other hand, with increasing depth and due to the existence of abnormal pressure zones, the difference between effective stresses shrinks dramatically. This may induce the fault to be triggered as per frictional faulting theory. Moreover, in terms of Mohr circles, the elevated pore pressure makes the Mohr's circle smaller. Thus, the gap between maximum and minimum effective principal stresses which is required to stimulate fault slip becomes smaller. Hence, production or injection on account of pore pressure constancy have a considerable influence on the size and position of Mohr's Circle. This effect may extend to the region's rock mechanical demeanor, which may motivate faults or fractures in a reservoir and its boundaries. This behavior is common in normal faulting systems (Krupnick and Echarte 2017).

### 2.1.1 Geostatic Vertical Stress

Simply, vertical stress is caused by the cumulative bulk density of the rocks. It is determined when the ground is horizontally leveled and the soil/rock nature is homogeneous in horizontal direction, otherwise it is utterly complex. Furthermore, it is supposed to consider the vertical stress as the principal stress in oil fields (Jaeger, Cook, and Zimmerman 2007). According to the equilibrium equation in soil and rock mechanics the overburden stress equation can be written:

$$\frac{\partial \sigma_z}{\partial z} + \frac{\partial \tau_{zx}}{\partial x} + \frac{\partial \tau_{zy}}{\partial y} - Sg = 0 \quad (2.4)$$

$$\frac{\partial \sigma_z}{\partial z} - Sg = 0 \quad (2.5)$$

$$\sigma_z = Sg \cdot z \quad (2.6)$$

In Equation (2.4), the shear stresses in (ZX) and (ZY) directions are assumed to be zero based on the above-mentioned concept. Therefore, the semi-final equation is (2.6) where  $Z$  is vertical depth and  $Sg$  is specific gravity (Jaeger et al. 2007). Finally, the formula to calculate the vertical stress in onshore fields will be equation (2.7):

$$\sigma_v = \int_0^Z \rho(Z)gdz \quad (2.7)$$

Where  $\rho$  is rock density,  $g$  is ground acceleration (Jaeger et al. 2007). Generally, density logs can be exploited for computation of the overburden stress.

Normally, density logs are not available from the surface and this is the most serious challenge in the overburden stress calculations. That is why the evaluation of *psuedodensity* in shallow depths is required. There are many procedures to determine a synthetic density of the surface layers, such as Amoco, Gardner's, Miller's formulas and Extrapolation (Rana and Chandrashekar 2015). Amoco method is an empirical equation, while Gardner's formula is based on sonic log or seismic velocity data. Eventually, Miller's equation is derived from rock porosity (Sen et al. 2017).

Obviously, differences between the results of the three aforesaid techniques can be seen when all methods are implemented on the same data. These variations, in turn, affect the results of the overburden stress calculation in shallow depths. Therefore, the most accurate method must be adopted. Extrapolation is the most common way to define the vertical stress in shallow depth. This procedure assumes that the density of sedimentary rock is in the range of  $1.8 - 2.0 \text{ g/cm}^3$ , porosity is 50-38 % and the bulk density of  $2.6 \text{ g/cm}^3$  (Fjaer et al. 2008). Essentially, consideration must be given to the influence of geological events such as sedimentation, erosion, deglaciation and uplifting. Furthermore, stress paths have a significant influence on the compaction and

consequently the density of the first few hundred meters of soil/rocks (D. Zoback 2007). More details will be provided in chapter four.

### 2.1.2 Geostatic Horizontal Stresses

Horizontal stresses are of vital importance for wellbore stability modeling. Unluckily, the prediction of stresses magnitude and orientation is a perplexing mission. Therefore, the uncertainty of measurement is extremely large. The reason for such a difficulty is that the stresses are dependent on the sedimentation and stress history (Guangzhi, He, and Xuefu 1988). Many techniques are applied for the purpose of horizontal stress estimation, such as anelastic strain recovery, differential strain curve and differential wave velocity analysis. However, three obstacles were diagnosed regarding these techniques. First, these procedures need oriented core samples; secondly, due to the developments of anelastic strains within 10–50 hours, the core sample test must be executed in less than the specified period; finally, the interpretation of the test is intractable if the rocks are anisotropic or fractured (Nauroy 2011).

The most reliable value of minimum horizontal stress can be obtained from a leak-off test (LOT), extended leak-off tests (Lin et al. 2008), and hydraulic fracturing (Fallahzadeh et al. 2017). The least principal stress is the minimum horizontal stress in both the normal and strike-slip faults regime according to Anderson's classification. Moreover, fracture occurs when the maximum tensile stress surrounding the wellbore surpasses the tensile strength of the rock. Whereas the propagation of fracture is perpendicular on the most tensile principal stress. Therefore, fracture initiation is perpendicular on the least principal stress, Figure 2.3, because in this direction the energy which is required to open a fracture is the minimal. This concept was demonstrated by means of laboratory testing (Hubbert and G. Willis 1957).

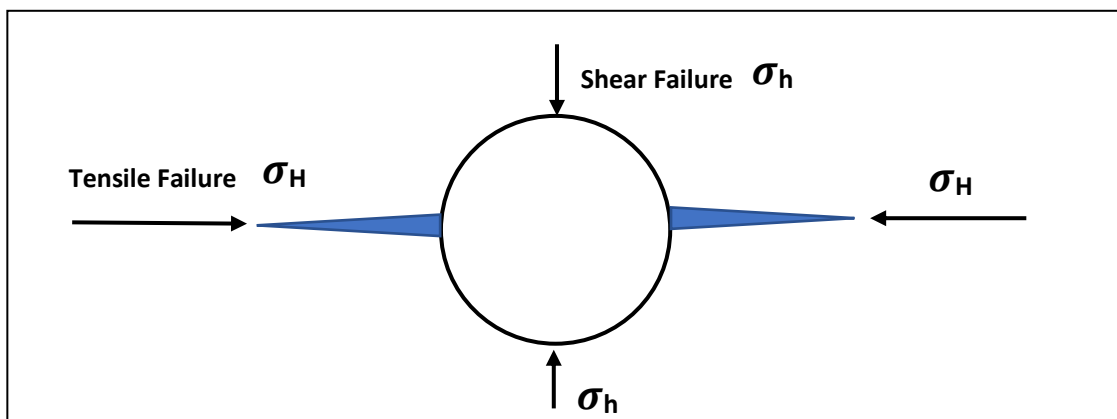


**Figure 2. 3 Fracture orientation in the direction of maximum Horizontal stress, Image was adapted.**

The International Society for Rock Mechanics (ISRM) recommends hydraulic fracturing as the most precise technique to measure the minimum horizontal stress. Hydraulic fracturing is preferred to be implemented in vertical wells assuming a wellbore parallel to the principal stress. However, fractures develop when the combination of mud pressure (Hydrostatic + pump pressure) and rock tensile strength becomes higher than the least principal stress (Nauroy 2011). Formation of planar or opening-mode fractures occurs when pore pressure increases due to tectonic activities or diagenetic processes, or due to the minimum stress decrement. Moreover, in normal and strike slip faults the plane of the fracture is vertical, while in reverse fault the plane is horizontal at 90 deg. with respect to vertical least stress (Zhang and Zhang 2017).

In LOT, XLOT and hydro-fracturing, the point at which the pressure-time curve diverges from the linearity is called leak-off pressure. It is considered as a starting point of fracture initiation around the wellbore as clarified in Figure 2.4 (John Lander Ichenwo 2017).

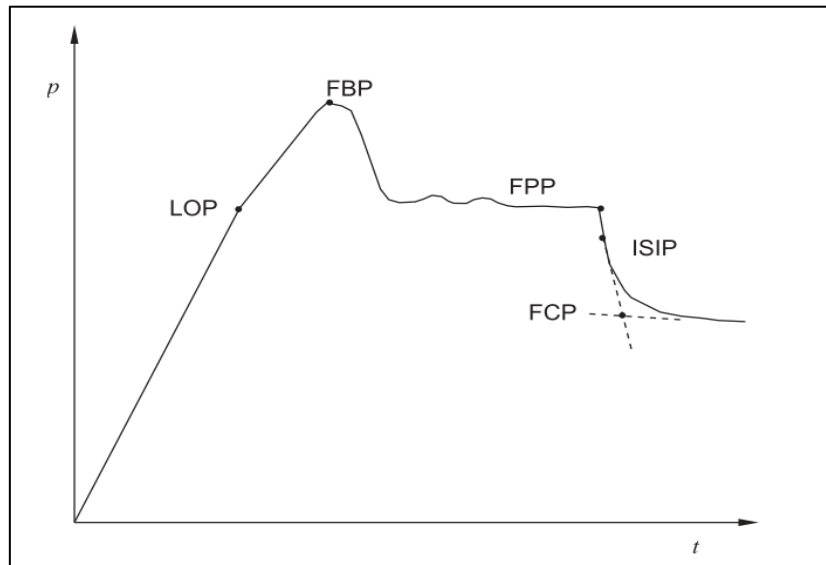


**Figure 2. 4 Leak of Test Scheme (Raaen et al. 2006).**

Where, FBP stands for formation breakdown pressure. FBP is the pressure when fluid starts to flow into formation. It is controlled by the in-situ stresses conditions and rock strength. In vertical wellbore and Normal Faulting ( $\sigma_v > \sigma_H > \sigma_h$ ), FBP can be evaluated from equation (2.8):

$$P_f = T_o + 3\sigma_h - \sigma_H - P_p \quad (2.8)$$

$P_f$  is formation breakdown pressure,  $T_o$  is the rock tensile strength and  $\sigma_h, \sigma_H$  are the minimum and maximum horizontal stresses, respectively.  $P_p$  is the pore pressure (Ibrahim and Nasr-El-Din 2018).

Fracture propagation pressure (FPP) is the upper limit of pressure accompanying fracture spreading within the rock formation. FPP is highly impacted by the rate of fluid injection, fluid viscosity and casing that effect the distribution of stresses around the casing string. The propagation pressure is quite close to the minimum principal stress, but the above three parameters must be considered (Fallahzadeh et al. 2017). Furthermore, instantaneous shut-in pressure (ISIP) is the identified pressure immediately after pumping stops, as demonstrated in Figure 2.4. The ISIP is the closest and most accurate point for defining the least principal stress. This is considered because when pumping stops the effect of friction generated as a result of flow rate and the fluid viscosity is eliminated (Haimson and Fairhurst 1967).

The magnitude of maximum horizontal stress can be estimated based on the hydraulic fracturing data. There is no direct method available at the present time to measure  $\sigma_H$ . It is one of the most difficult parameters to determine, which is why the error rate in the valuation of  $\sigma_H$  is quite large. There are many techniques that can be employed for the purpose of computing the maximum horizontal stress. For instance, Djurhuus and Aadnoy, in 2003, used multiple fracturing data, and image logs such as FMI and UBI of deviated wells, Figure 2.5. In addition to exploiting an induced fracture from leak-off tests of many wells, they constructed their theory and defined the magnitude and directions of horizontal stresses with inversion method. This technique depends on the Kirsch's solution.

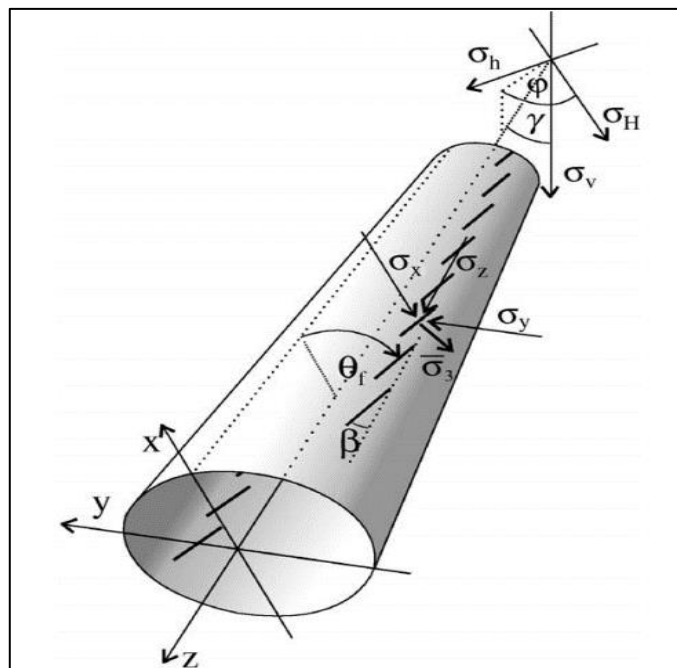


**Figure 2. 5 Various directions of wellbore and stress states (Aadnøy and Looyeh 2011).**

Induced fracture occurs at  $\theta = 0$  or  $\theta = 90$  dega as defined in equation (2.9)

$$\tan(2\theta) = \frac{2\tau_{xy}}{\sigma_x - \sigma_y} \quad (2.9)$$

Stress transformation is applied on equation (2.8) to obtain:

$$\frac{P_{wf} + P_o - \sigma_T}{\sigma_v} + \sin^2\gamma = (3 \sin^2\varphi - \cos^2\varphi \cos^2\gamma) \frac{\sigma_H}{\sigma_v} + (3 \cos^2\varphi - \sin^2\varphi \cos^2\gamma) \frac{\sigma_h}{\sigma_v} \quad (2.10)$$

$$\frac{P_{wf} + P_o - \sigma_T}{\sigma_v} - 3\sin^2\gamma = (3 \cos^2\varphi \cos^2\gamma - \sin^2\varphi) \frac{\sigma_H}{\sigma_v} + (3 \sin^2\varphi \cos^2\gamma - \cos^2\varphi) \frac{\sigma_h}{\sigma_v} \quad (2.11)$$

Equation (2.10) and (2.11) can be redefined to gain:

$$P' = a \frac{\sigma_H}{\sigma_v} + b \frac{\sigma_h}{\sigma_v} \quad (2.12)$$

$P'$ ,  $a$  and  $b$  can be determined from the following equations:

$$P' = \frac{P_o + P_{wf}}{\sigma_v} + \sin^2\gamma \quad (2.13)$$

$$a = 3 \sin^2\varphi - \cos^2\varphi \cos^2\gamma \quad (2.14)$$

$$b = 3 \cos^2\varphi - \sin^2\varphi \cos^2\gamma \quad (2.15)$$

The linear *poroelastic* strain model is another common technique to specify the horizontal stresses. This method provides continuous profiles of  $\sigma_H$  and  $\sigma_h$  based on a plain strain model. The minimum horizontal stress is derived from the *poroelastic* equation:

$$\sigma_h = \frac{v_s}{1-v_s} (\sigma_v - \alpha P_o) + \alpha P_o \quad (2.16)$$

Past and current tectonic stresses may cause deformation and horizontal strain which must be considered in the conventional stress equation (Song 2012). In order to demonstrate the mathematical relationship of horizontal stress and strain, Hooke's law can be applied (Hayavi and Abdideh 2016). The final equations of the poroelastic strain model are (2.17) and (2.18). These two formulas are used in some MEM softwares such as Schlumberger's Techlog.

$$\sigma_h = \frac{v}{1-v} \sigma_v - \frac{v}{1-v} \alpha P_o + \alpha P_o + \frac{E}{1-v^2} \varepsilon_h + \frac{vE}{1-v^2} \varepsilon_H \quad (2.17)$$

$$\sigma_H = \frac{v}{1-v} \sigma_v - \frac{v}{1-v} \alpha P_o + \alpha P_o + \frac{E}{1-v^2} \varepsilon_H + \frac{vE}{1-v^2} \varepsilon_h \quad (2.18)$$

The other major task in reservoir geomechanics is to determine the orientation of horizontal stresses. Consequently, realization of stresses direction helps in appointing an optimized wellbore trajectory in drilling. While in production, it assists locating the preferred orientation of perforation and avoiding sand production. Hence, logging tools can be utilized for this purpose. Many tools are available including formation micro imager (FMI), Caliper logs, Ultrasonic borehole televiewer (BHTV), Resistivity and cross-dipole logs (Tiwari 2013). If the stresses are anisotropic, according to Anderson’s classification, there will be possibility of failure in the formation. The failure can be Shear failure (break out) in the direction of minimum horizontal stress or tensile failure (Breakdown) in the azimuth of maximum horizontal stress.

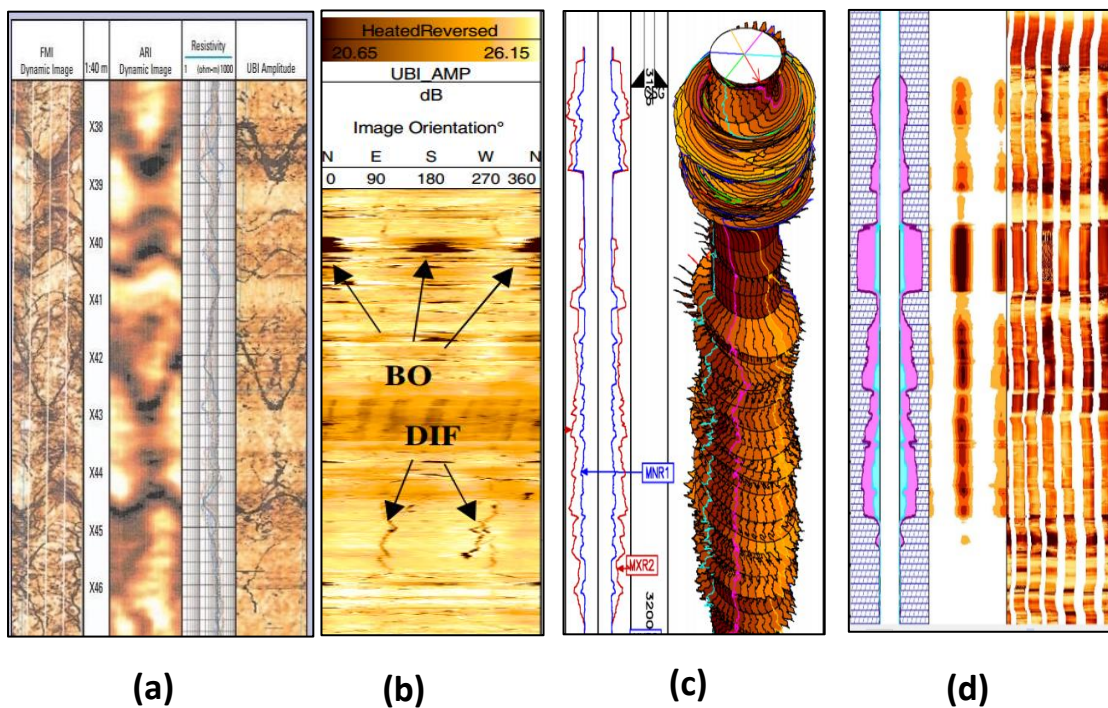


**Figure 2. 6 Natural Fracture on FMI, Resistivity and UBI. (b) 3D oriented caliper log. (c) Break out on FMI (Bailey et al., 2015, Field data).**

It is extremely essential to recognize the natural fracture from drilling induced tensile fractures. In Figure 2.6 (a) FMI, Resistivity and UBI show a sinusoidal fracture; this profile emphasizes that the type of fracture is natural. On the other hand, a drilling induced tensile fracture (DIF) can be realized as a straight vertical line if the well is vertical and parallel lines on the same orientation if the well is deviated as illustrated in Figure 2.6 (b). In this case, FMI tools and Oriented caliper logs can help in detecting the direction of stresses and type of fractures. Figure 2.6 (c) shows 3D Wellbore geometry derived from 6 arms caliper logs. The direction of minimum horizontal stress can also be inferred by the presence of breakout as demonstrated in Figure 2.6 (d) (Kundan and Sen 2015).

The polarization of shear waves is the other way to define the horizontal stresses direction. The propagation of sound waves takes place at equal speed within the formation if the medium is isotropic, and this is not perfectly true. In addition, shear waves have two sections, fast shear and slow shear waves. Thus, the particle motions of these two components are perpendicular on each other Figure 2.7. For that reason, the polarization of the fastest shear wave spreads into the stiffest direction (maximum Horizontal stress). This is valid if the wellbore is vertical, and the medium is anisotropic. Therefore, the polarization phenomenon was exploited to determine the orientation of horizontal stresses (Donald et al. 2015).

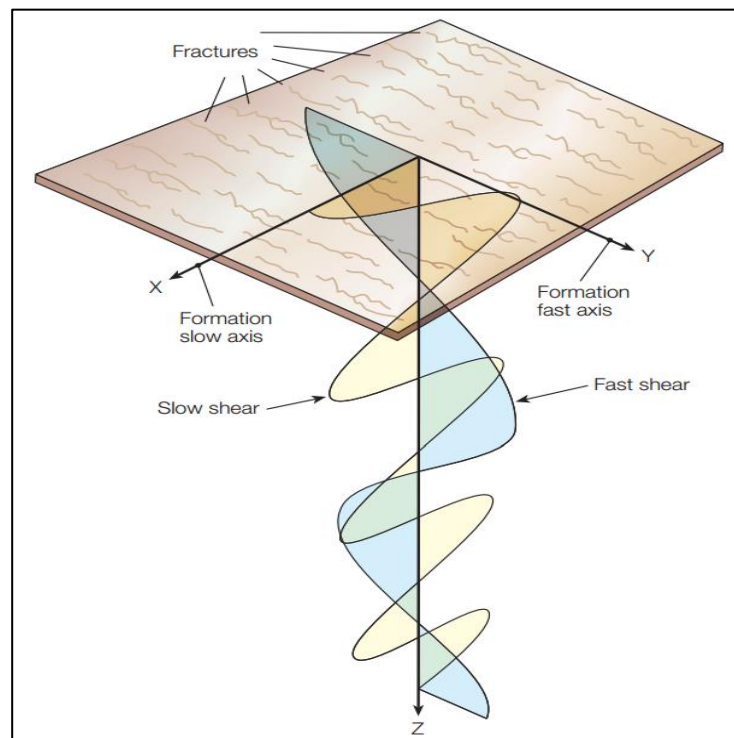


**Figure 2. 7 Formation of fast and slow axes of shear wave (Ezati and Soleimani 2014).**

Using the same preceding principle, directional acoustic tools like Cross-Dipole log can be used to determine the orientation of the bedding plane in laminated rocks (Tang, Land, and Patterson 2008). The impact of bedding plane on wellbore stability and rock mechanical strength is discussed in detail in the section on rock failure criteria.

## 2.2 Pore Pressure

Rock failure is controlled by effective stress which is a function of pore pressure as per Terzaghi's principle. For that reason, pore pressure is a decisive parameter in geomechanics, especially in shale rocks. It is immensely important to determine the

pore pressure in shale formations for many reasons. Shale is characterized as high pressure lithology due to the compaction disequilibrium process, along with laboriousness of precise tensile and shear failure prediction. Furthermore, the chemical reaction between drilling fluid and formation water makes calculations more confusing (Zhang et al. 2006).

Unfortunately, there is no direct method for pore pressure measurement in shale intervals due to the permeability being insufficient for fluids mobility. Therefore, the only way to detect the pore pressure is by means of indirect methods. On the other hand, direct evaluation through logging tools such as Repeated Formation Tester (RFT) can be utilized in permeable formations like carbonate and sandstone rocks.

### 2.2.1 Normal Compaction Trend (NCT)

According to the NCT, interval travel times ( $\Delta t$ ) versus depth can be plotted on two cycles of semi log paper. When the condition is normal compaction, trend line is drawn as a reference line. Any increment in  $\Delta t$  refers to abnormal compaction and consequently abnormal pore pressure, Figure 2.8. The anomaly in trend is due to high transit time or porosity of formation with respect to depth (Das and Mukherjee 2020).

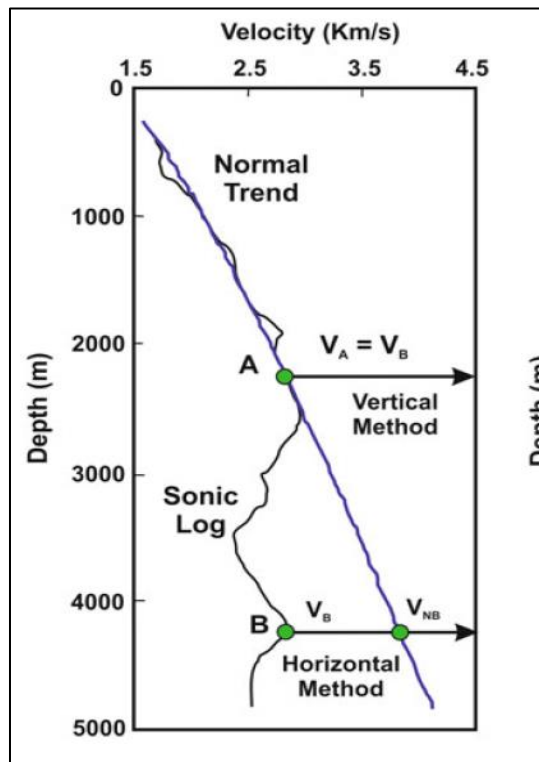


**Figure 2. 8 Normal compaction trend in Interval Transit Times versus Depth (Das and Mukherjee 2020).**

Gardner et al. (1974) developed a formula to estimate pore pressure based on Hottmann and Johnson's prediction equation (2.19)

$$P_p = \sigma_v - \frac{(\alpha_v - \beta)(A1 - B \ln(\Delta t))^3}{z^2} \quad (2.19)$$

A1 = 82776 and B1 = 15695,  $\alpha_v$  stands for gradients of normal overburden stress,  $\beta$  is gradient of normal pore pressure.

### 2.2.2 Eaton Method

Eaton's technique employs log derived methods to predict pore pressure. It is totally based on disequilibrium compaction principles. Eaton (1972) used resistivity log to develop an empirical equation to estimate the pore pressure in shale formations. The main drawback in this method is that it is more accurate in young sedimentary basins when the resistivity log is recorded satisfactorily (Zhang 2011).

$$P_{pg} = OBG - (OBG - P_{pn})\left(\frac{R_0}{R_n}\right)^x \quad (2.20)$$

Where  $P_{pg}$  is pore pressure gradient,  $OBG$  is overburden gradient,  $P_{pn}$  is gradient of normal hydrostatic pore pressure,  $R_0$  is shale resistivity recorded on log,  $R_n$  is the normal resistivity of shale.

In 1975 Eaton proposed another mathematical formula using compressional slowness to predict the formation pressure. He supposed that both vertical effective stress and pore pressure impact the overburden stress according to Terzaghi's principle.

$$P_{pg} = OBG - (OBG - P_{pn})\left(\frac{\Delta t_n}{\Delta t_0}\right)^x \quad (2.21)$$

Where  $\Delta t_n$  is the Shale slowness at normal trend line,  $\Delta t_0$  is Shale slowness derived from sonic log (Zhang 2011). The exponent "x" relies on the way that is utilized to assess the normal compaction trend line. It is usually equal to 3 if the Sonic Log (or seismic data) has been evaluated or to 1.5 if a resistivity log was considered. The exponent values in the main equations relate to the Gulf of Mexico, but globally the exponent needs to be updated for the area of study (Azadpour and Manaman 2015).

### 2.2.3 Holbrook Method

Holbrook is one of the indirect techniques exercised in pore pressure calculations. It was applied to obliquely appreciate the pore pressure in carbonate, sandstone and shaly limestone rocks in the North Sea. Holbrook is one of the methods currently

adopted in the oil industry. The process is based on the interrelation between effective stress, porosity and mineralogy as described in the following demonstration:

$$\sigma'_v = \sigma_{max}(1 - \emptyset)^\beta \quad (2.22)$$

$$P_p = \sigma_v - \alpha\sigma'_v \text{ (Terzaghi)} \quad (2.23)$$

$$P_p = \sigma_v - \sigma_{max}(1 - \emptyset)^\beta \quad (2.24)$$

Where  $\sigma'_v$  stands for the effective vertical stress,  $\sigma_{max}$  is the maximum hypothetical value of effective vertical stress and it is lithology dependent.  $\emptyset$  stands for the formation porosity,  $\beta$  is the coefficient of compaction strain-hardening (Adham 2016).

**Table 2. 1 Parameters used to determine pore pressure in Holbrook technique (Holbrook 1999).**

Rock	$\beta$	$\sigma_{max}$	Grains density	Solubility	Hardness
Quartz sand	13.219	130000	2.65	6	7
Average shale	8.728	18461	2.54-3.15	20	3
Calcite sand	13	12000	2.71	140	3
Anhydrite	20	1585	2.87	300	2.5
Halite sand	31.909	85	2.16	350000	2

### 2.3 Rock mechanical strength and deformation.

Rocks are categorized into isotropic and anisotropic. They are isotropic if the applied stresses at any direction present the same mechanical properties, otherwise the rocks are anisotropic. Furthermore, the anisotropy is classified into Intrinsic and Structural anisotropy. Intrinsic anisotropy occurs when the strength properties of homogeneous substances are different with respect to the directions of the exerted forces. On the other hand, structural anisotropy comes from the existence of bedding planes or foliations such as the shale formation texture. Most sedimentary rocks act as anisotropic, the reason being the existence of weakness plane or fabric. This characterization is based on the tendency of sediment clasts or grains to follow the water direction during sedimentation, Figure 2.9 (Schlunegger and Garefalakis 2018).

Whether rocks are transversely isotropic can be detected in triaxial tests or tensile tests. The tests results will be dependent on the applied stresses' orientation. This explains the major role played by selection of a proper failure criterion in the success of the geomechanical study (Deangeli and Omwanghe 2018).

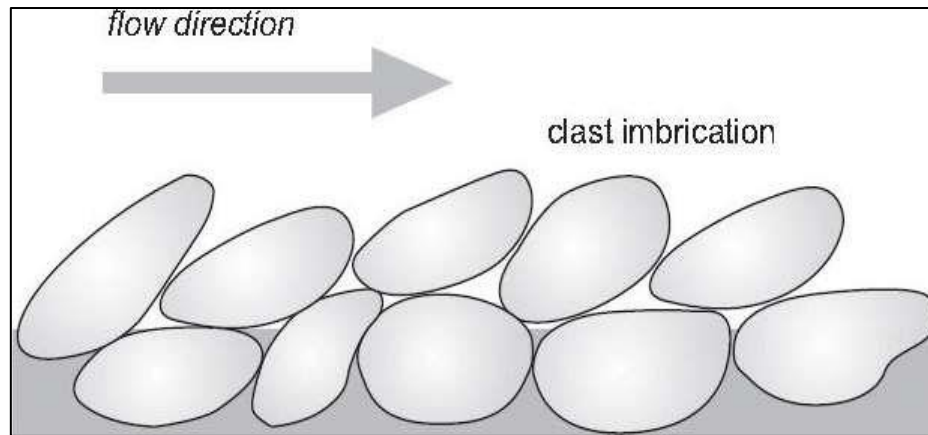


**Figure 2. 9 The effect of flow direction on the fabric of rocks (MACAULAY et al. 2016).**

The severity of the rock deformation depends exclusively on strength of the rock and the magnitude of the applied stresses. Thus, the stress-strain relationship, which is also called constitutive law, is extremely dependent on the sort of material and geometry; therefore, the relationship is often not linear. Consequently, many constitutive laws were derived to characterize the material's response to applied stresses. If the put-on stress is low, the response will be linear, while the rock behavior is non-linear when the applied stress is quite high. This dictates classification of the response into elastic, plastic, viscous and *viscoelastoplastic*. Generally, the rocks are assumed to be homogeneous – isotropic and linear elastic in modeling, but in reality rocks are anisotropic and non-linear elastic (Aadnøy and Looyeh 2011).

### **2.3.1 Theory of Elasticity & Biot Coefficient**

Many rocks are subjected to the theory of elasticity that is the traditional constitutive law. The material is said to be elastic if the stress strain correspondence is one to one. In addition, distortion or strain of elastic materials is within the framework of infinitesimal deformation away from any damage or significant change in the rock's shape. Consequently, just removing the stress is enough to restore the stressed rock into normal status. Thus, the stress strain relation in rock mechanics is complex and linear elasticity is therefore applied in order to simplify the analyses of stresses around the wellbore or faults and fractures (Jaeger et al. 2007). The elastic constants are given by:

$$\sigma_{ij} = C_{ijhk}\varepsilon_{hk} \quad (2.25)$$

$$\varepsilon_{ij} = D_{ijhk}\sigma_{hk} \quad (2.26)$$

Where  $C_{ijhk}$  is the stiffness tensor and  $D_{ijhk}$  the compliance tensor. Both tensors are fourth order and they have 81 elastic constants, 36 of which are independent.

The material is elastically homogeneous when every single point of the medium has the same elastic constant. According to Voigt notation, the *iperelastic* materials present physical symmetry. Moreover, based on the function of strain energy, the number of independent elastic constants becomes 21. Finally, in Isotropic Linear Elastic material the number of constants can be reduced to just two. These two constants can be “Young’s modulus and Poisson’s ratio” or “Shear and Bulk modulus” (Nauroy 2011).

**Young’s modulus (modulus of elasticity):** is stress strain relationship in terms of linear elasticity theory Figure 2.10 (a). It is applied to determine the stiffness of material in uniaxial compression status, Figure 2.10 (b) (Nauroy 2011).

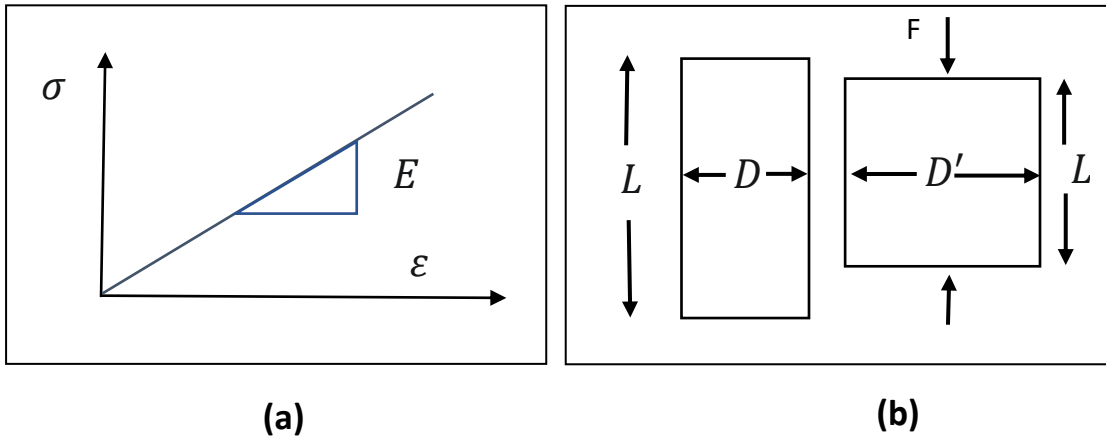


**Figure 2. 10 (a) Young’s modulus in stress strain relationship. (b) Axial & Radial strain - uniaxial stress, Images adapted from reference (Fjaer et al. 2008).**

$$\sigma_z = \frac{F}{A} \quad (2.27)$$

$$\varepsilon_z = \frac{L-L'}{L} \quad (2.28)$$

$$\varepsilon_x = \varepsilon_y = \frac{D-D'}{D} \quad (2.29)$$

$$E = \frac{\sigma_z}{\varepsilon_z} \quad (2.30)$$

**Poisson's ratio ( $\nu$ ):** is a measure of lateral deformability in rocks. The value of the ratio depends on the orientation of the applied stresses and the direction of the longitudinal strain through which the ratio was measured. This applies in the case of anisotropic rocks, while in isotropic rocks the ratio is direction independent (Aadnøy and Looyeh 2011). From Figure 2.10 (b), Poisson's ratio formula can be derived:

$$\nu = - \frac{\varepsilon_x}{\varepsilon_z} \quad (2.31)$$

**Shear modulus:** is indicated by  $G$  or sometimes  $\mu$ . It refers to the measurement of shear or tangential strain in rocks that are subjected to shear stress, Figure 2.11 (a). In fluids the shear modulus disappears because the shear strength of fluid is negligible (Jaeger et al., 2007).

$$G = \frac{E}{2(1+\nu)} \quad (2.32)$$

**Bulk modulus ( $K$ ):** is a measure of a material's stiffness when exposed to hydrostatic compression, as illustrated in Figure 2.11 (b) (Russell, Smith, and Hampson-Russell 2007).

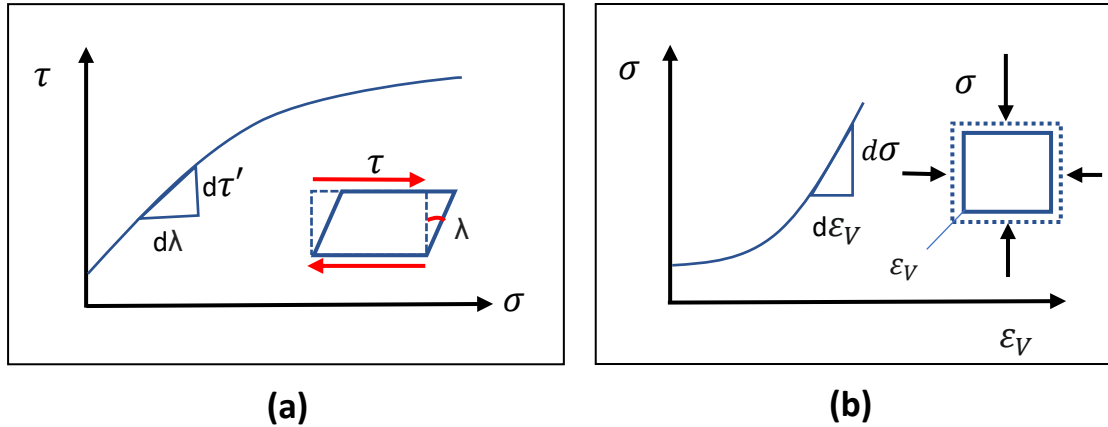


**Figure 2. 11 Shear Modulus. (b) Bulk Modulus, images adapted from reference ([environment.uwe.ac.uk/geocal/SoilMech/basic/stiffness.htm](http://environment.uwe.ac.uk/geocal/SoilMech/basic/stiffness.htm)).**

$$K = \frac{P}{\varepsilon_V} = \frac{E}{3(1-2\nu)} \quad (2.33)$$

The elastic moduli can be determined directly from laboratory tests such as Uniaxial (Unconfined) compression test and Triaxial compression test (TXT). On the other side, indirect techniques have been widely used recently to obtain a continuous profile of dynamic elastic moduli. The dynamic model is based on compressional wave velocity ( $V_p$ ) and shear wave velocity ( $V_s$ ) using the following dynamic equations.

$$E_{dyn} = \frac{\rho v_s^2 (3v_p^2 - 4v_s^2)}{(v_p^2 - v_s^2)} \quad (2.34)$$

$$v_{dyn} = \frac{\left[ \frac{1}{2} \left( \frac{v_p}{v_s} \right)^2 - 1 \right]}{\left[ \left( \frac{v_p}{v_s} \right)^2 - 1 \right]} \quad (2.35)$$

$$G_{dyn} = \rho v_s^2 \quad (2.36)$$

$$K_{dyn} = \rho \left[ v_p^2 - \frac{3}{4} v_s^2 \right] \quad (2.37)$$

Considerable studies based on practical experiences have demonstrated that the difference between static and dynamic models can be obvious. The dominant model is a dynamic model with a difference of 4-8 times in the Young's Modulus, for instance. There are many reasons governing that discrepancy, including frequency variations. The rock is tested in the laboratory with 100 kHz–1 MHz, while the dynamic moduli are derived from logs which are performed with 10–20 kHz. Thus, the amplitude of strain in dynamic is extremely slight, while in static it is relatively large (Mashinsky 2003). Furthermore, that divergence is significantly maximized in porous and weak rocks.

Another reason derives from drained and undrained conditions. Rock deformation in log-derived moduli is undrained, so the elastic parameters are higher compared with those obtained from lab test in drained conditions. Finally, the unloading-reloading round in static lab tests may aggravate the distinction. Whereas the stiffness of rocks in the first loading is higher than that in unloading-reloading cycles, Figure 2.18, and this is not the case in dynamic measurements (Fjaer et al. 2008).

**Biot Coefficient ( $\alpha$ ):** is a function of the rock skeleton and solid grains' compressibility. In other words, it is the variation of pore volume to bulk volume (Selvadurai, Selvadurai, and Nejati 2019).

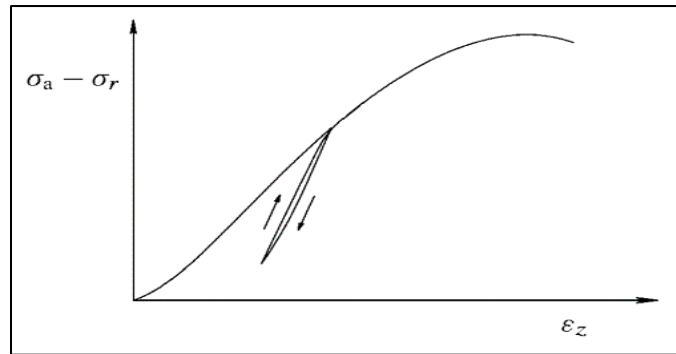


**Figure 2. 12 Unloading-reloading round in static lab test (Fjaer et al., 2008).**

$$\alpha = 1 - \frac{K'}{K_s} \quad (2.38)$$

Where  $K'$  stands for the drained bulk modulus of rock skeleton and  $K_s$  is the solid phase bulk modulus. The Biot Coefficient greatly affects the behavior of rocks and the local

stresses, which in turn change as a result of alteration in the reservoir pressure. Many techniques have been developed to measure  $\alpha$ . The first method was presented by Biot and Willis (1957) (Civan 2020). The Biot coefficient can be determined empirically using indirect methods.

$$\alpha = 1 - (1 - \phi)^{\left(\frac{3}{1-\phi}\right)} \quad (2.39)$$

$$\alpha = 1 - (1 - \phi)^{3.8} \quad (2.40)$$

Formula (2.39) was developed by Krief in 1990 for dry rocks, while equation (2.40) by Wu in 2001 for consolidated rocks.

### 2.3.2 Tensile strength ( $T_o$ )

Tensile strength is included in the formula of minimum and maximum horizontal stresses calculations. It is neglected in unconsolidated formation and considered in compacted consolidated rocks. Tensile strength can be measured directly with the direct tensile test or indirectly by means of Brazilian and Index tests. However, there are some obstacles that hinder the accurate measurement of  $T_o$ , either directly or indirectly. These obstacles are: the tensile strength is direction dependent, sample size dependent and flaw dependent. (Claesson and Bohloli 2002).

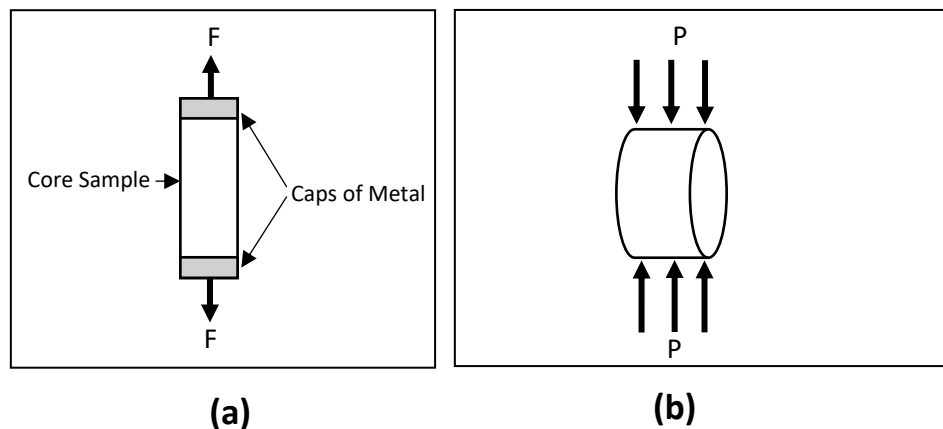


**Figure 2. 13 Direct tensile test, (b) Brazilian test, images were adapted**

The direct tensile test of rocks requires a uniaxial and uniform stress state on the rock specimen, otherwise the results will be imprecise. Furthermore, bending moments may develop due to the incorrect position of specimen in relation to loading frame. In addition, early failure may occur at the hold points of specimen ends because of stress concentration at the ends, Figure 2.13 (a). Practically fulfilling optimized uniaxial test

conditions is extraordinarily intractable, which is why indirect methods are commonly used (Briševac, Kujundžić, and Čajić 2015).

The most appropriate indirect technique is the Brazilian test. It gives an approximate value of tensile strength. In this approach, the rock sample is exposed to a specific load by using two platens that frame the specimen in circular mode, Figure 2.13 (b). The diameter of the rock cylinder must be equal to or greater than its length. Accordingly, normal tensile stresses on the vertical diameter of specimen are motivated by compressional load, while remaining constant in the area surrounding the center. Hence, the spot where the stress is at its maximum value will be subjected to failure. The stresses close to the sample center can be calculated from equation (2.41) (Li and Wong 2013).

$$T_0 = \frac{2P}{\pi D_t} \quad (2.41)$$

Where P is the failure load and D is the specimen diameter.

On the other hand, log dynamic compressive strength (UCS) can be used to determine a continuous profile of tensile strength using equation (2.42).

$$T_0 = UCS \cdot K \quad (2.42)$$

Where K is a factor that depends on the zone's facies, it is assumed that the tensile strength is equal to 10 – 12 times the UCS in all facies. This range may not be correct for some reason, such as the existence of microcracks according to the Griffith crack theory, the orientation of lamination which is based on the plane of weakness model, type of lithology, and finally the rock compaction (Li and Wong 2013).

### **2.3.3 Uniaxial (Unconfined) Compressive Strength**

Uniaxial compressive strength is of vital importance in determining the mud window. This is done through constraining the value of maximum horizontal stress and finding the proper envelopments of rock failure (Adham 2016). Jaramillo R.A (2004) found that the UCS value has a large impact on the wellbore stability. That influence is higher than the effect of well deviation, azimuth, mud weight and fluid exposure time. In turn, this significance dictates on the researchers to find the correct calculations of UCS. Uniaxial compressive strength value can be measured by using static or dynamic models. Statics model from laboratory and dynamic one derived from well logs (interval transient time and density logs).

The static technique is based on the results of various laboratory tests such as Unconfined Compression Test (UCT), Triaxial Test (TXT) and Thick Wall Cylinder Tests (TWC). Although there are some technical challenges in the measurement of UCS by TXT and UCT, especially in shale and clay, these are the most reliable tests to define the UCS (García et al. 2008).

Because of the high costs involved in taking core samples and conducting laboratory tests, the UCS is known only at limited intervals. Therefore, it is necessary to use available geophysical logs to derive UCS along the layers of interest. The rock's elastic and physical properties have an influence on rock strength. That is why geophysical logs such as density and slowness are employed to derive the rock UCS. These log data are exploited to construct a continual UCS peak and then correlation must be established with the UCS obtained from laboratory tests. Many correlations have been developed for different kinds of rocks and regions around the world. Zoback (2007, 2010) introduced some empirical relations to figure out the UCS in Carbonates, Shale and Sandstone formations.

For sandstone, equation (2.43) is recommended everywhere around the globe, while equation (2.44) is proposed for sedimentary formation, equation (2.45) for shale, and formula 2.46 for compacted strong shale.

$$UCS = 2.28 + 4.1089 E \quad (2.43)$$

$$UCS = 245 (1 - 2.7 \phi)^2 \quad (2.44)$$

$$UCS = 7.22 E^{0.712} \quad (2.45)$$

$$UCS = 1.35 \left( \frac{304.8}{\Delta t} \right)^2 \quad (2.46)$$

Sometimes, these mathematical equations may give results that are identical to laboratory tests in specific regions around the world or in a certain rock. Other than that, the outcomes are far from laboratory test results (Chang, Zoback, and Khaksar 2006).

### **2.3.4 Shear strength parameters (cohesion, friction angle)**

Shear strength is defined as the maximum value of shear stress that rocks or soil can withstand. In other words, it represents the rock particles' or grains' impedance to deformation. Shear strength plays a critical function in the analysis of rock mechanics, and the parameters include rock cohesion and friction angle. Thereby, the failure takes place at maximum shear stress ( $\tau_{max}$ ) which exceeds the cohesion and friction angle.

Furthermore, rock shear strength is vastly dependent on water content and presence of weakness plane. Thus, the strength parameters can be measured directly in the laboratory by means of TXT and UCT or indirectly using geophysical logs data (Gong et al. 2020).

**Cohesion ( $C'$  inherent shear strength):** in soil mechanics, Cohesion is the force that bonds particles or grains together by means of cementation between sand grains or electrostatic forces in the case of clay (Komurlu and Demir 2018).

**Friction angle ( $\varphi'$ ):** When the normal stress increases on the failure plane, Figure 2.14, then the variation of rock resistance is described by friction angle.  $\varphi'$  can be defined as the measurement of rock shear strength because of friction. The friction angle can possibly be obtained from Gamma Ray and porosity logs. Many mathematical correlations were outlined by Zoback in 2010 to determine  $\varphi'$  from logs:

$$\varphi' = 70 - 0.417 GR \quad (2.47)$$

$$\varphi' = \tan^{-1} \left( \frac{78 - 0.4 GR}{60} \right) \quad (2.48)$$

$$\varphi' = 57.8 - 105 GR \quad (2.49)$$

Where equation (2.47) is used for shaly sedimentary rock, equation (2.48) in shale and equation (2.49) for sandstone. However, the angle value that measured in laboratory tests is the most rigorous (D. Zoback 2007).

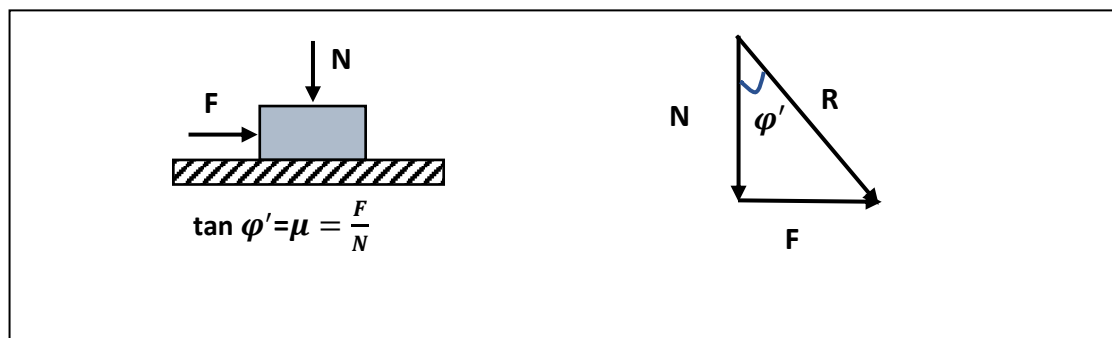


**Figure 2. 14 The concept of Friction angle, Images were adapted**

## Rock Failure Criteria

Over the years, researchers developed many criteria for rocks failure that are of great importance in geomechanical analyses. The selection of appropriate failure criterion is certainly significant in wellbore stability, specifically in the definition of shear, tensile and compressive rock failure. Some of these criteria take into account only the effect of maximum and minimum principal stresses and they are the most common. On the other hand, there are couples of criteria that include the impact of the intermediate principal stress. This kind of envelope is more sophisticated but based on poly-axial tests (Jaeger et al. 2007). Some investigators have underappreciated the results obtained from criteria which do not consider the influence of  $\sigma_2$  such as the Mohr-Coulomb criterion. They demonstrated that the outcomes of two-dimensional criteria are not reasonable. Applying  $\sigma_2$  in some envelopes like Mogi criterion may cause the rocks to be strengthened (Song and Haimson 1997).

The typical barrier of applying any criterion which takes intermediate principal stress into account is the requirement of the True Triaxial test. Any inventing of the  $\sigma_2$  value from the standard Triaxial Test using some empirical relations may alter the final approach. However, in real situations, stresses around the wellbore are three dimensional. That is why including  $\sigma_2$  in the failure criterion may display the most precise outcomes (Rahimi 2014).

### 3.1 Mohr-Coulomb

The maximum shear stress or the larger diameter of Mohr circle that the material can afford represents the connection among compressive, tensile and shear strength. According to Mohr-Coulomb, the rock failure is examined in two dimensional circles of Mohr.

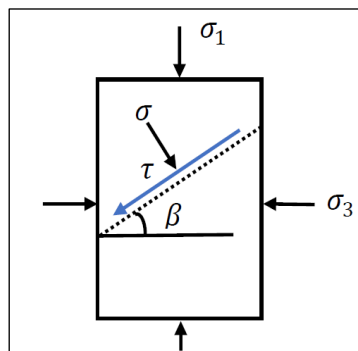


Figure 3. 1 Shear stress and failure plane, figure was adapted.

When compressive stress is applied on a rock sample, shear stress will develop on a plane. Consequently it will cause failure if the stress exceeds rock inherent shear strength ( $C'$ ) and friction angle ( $\varphi'$ ) Figure 3.1 (Aslannezhad, Khaksar Manshad, and Jalalifar 2016). The Mohr-Coulomb criterion is given by an equation that represents a linear relationship characterized by cohesion and friction angle.

$$\tau = \frac{1}{2} (\sigma_1 - \sigma_3) \sin 2\beta \quad (3.1)$$

$$\sigma = \frac{1}{2} (\sigma_1 + \sigma_3) + \frac{1}{2} (\sigma_1 - \sigma_3) \cos 2\beta \quad (3.2)$$

Where  $\beta$  stands for the angle of the failure plane, Figure 3.1, and it is given by:

$$\beta = 45^\circ + \frac{\varphi'}{2} \quad (3.3)$$

By including the Terzaghi principle, Figure 3.2 (a,b)

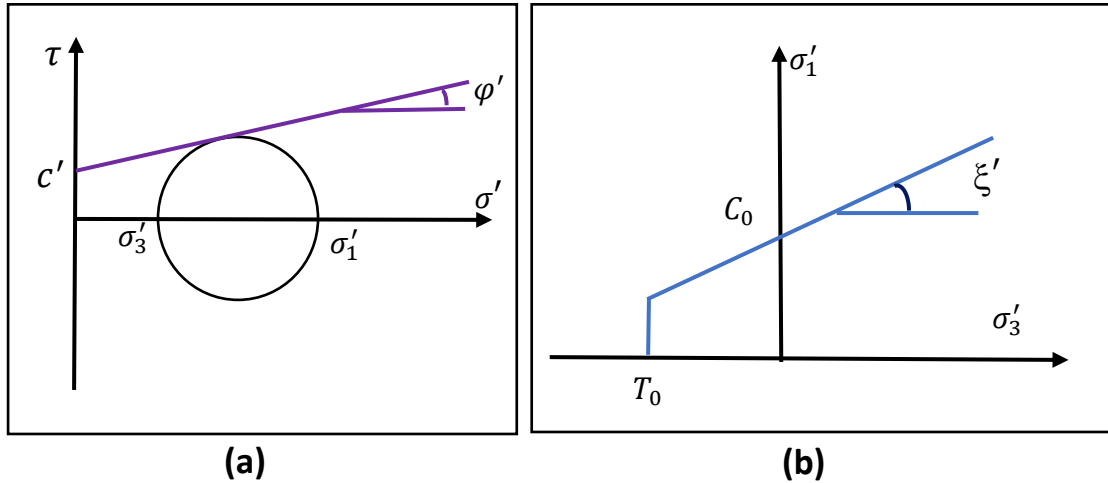


**Figure 3. 2 Mohr-Coulomb, (a) Shear stress and effective normal stress relationship, (b) Principal stress and UCS & UTS in the Mohr-Coulomb criterion envelope, figures were adapted**

$$\sigma'_1 = \frac{2c' + \sigma'_3 [\sin 2\beta + \tan \varphi' (1 - \cos 2\beta)]}{\sin 2\beta - \tan \varphi' (1 + \cos 2\beta)} \quad (3.4)$$

$$\tau_s = c' + \sigma' \tan \varphi' \quad (3.5)$$

$$\sigma'_{1s} = \frac{2c' \cos \varphi' + \sigma_3 (1 + \sin \varphi')}{1 - \sin \varphi'} \quad (3.6)$$

$$N_\theta = \tan \xi' = \frac{1 + \sin \varphi'}{1 - \sin \varphi'} \quad (3.7)$$

Where  $\tau_s$  is the peak of shear strength and  $\sigma'$  is the normal stress.  $N_\theta$  is line slope in  $\sigma'_1$  &  $\sigma'_2$  and  $\xi'$  is the angle of line in  $\sigma'_1$  &  $\sigma'_2$  graph, Figure 3.2 (b).

In practical situation uniaxial tensile stress  $T_0$  is assumed to be zero, but sometimes tensile cut-off is applied to be more realistic.

$$UCS = C_0 = \frac{2 C' \cos \varphi'}{1 - \sin \varphi'} \quad (3.8)$$

$$T_0 = \frac{2 C' \cos \varphi'}{1 + \sin \varphi'} \quad (3.9)$$

### 3.2 Hoek-Brown

Some failure criteria were presented to describe the failure in transversely isotropic rocks. Hoek-Brown, in the 1980s, analysed failure in rocks that exhibit anisotropy due to the presence of discontinuities. The empirical criterion was developed according to TXT that was conducted on a large number of fractured rocks. The discontinuities and rock matrix properties are included in the equation of nonlinear form:

$$\sigma'_1 - \sigma'_3 = \sqrt{m C_0 \sigma'_3 + s C_0^2} \quad (3.10)$$

Where  $m$  and  $s$  are strength parameters of rocks, they depend on the properties of the rock matrix and fissures. The value of  $s$  can be determined visually for intact rocks ( $s = 1$ ), while  $m$  is defined from Triaxial tests. The criterion was amended in 2001 by Tien and by Kuo and Unlu in 2004. They indicated that in every deviation of the weakness plane the rock is intact ( $s = 1$ ) and it is instantaneously isotropic. Equation 3.10 was modified to be:

$$(\sigma'_1 - \sigma'_3)_{\beta_w} = \sqrt{m_{\beta_w} C_{0\beta_w} \sigma'_3 + C_{0\beta_w}^2} \quad (3.11)$$

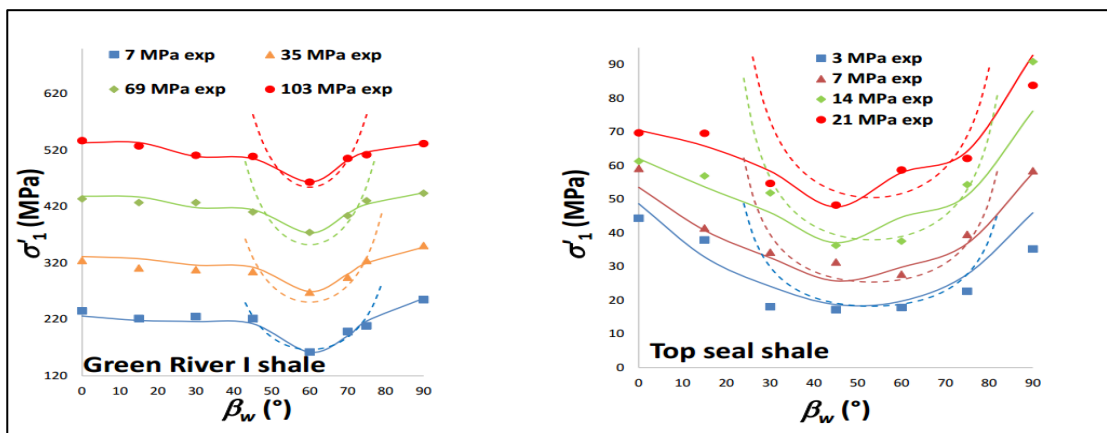


**Figure 3. 3 TXT at different bedding plane inclination: Experimental data (symbols), H&B (Solid lines) and dotted lines are weakness plane (Deangeli and Omwanghe 2018).**

Where  $m_{\beta_w}$  is an instantaneous dimensionless constant of every deviation in the weakness plane ( $\beta_w$ ).  $C_{0\beta_w}$  stands for instantaneous uniaxial compressive strength at each  $\beta_w$ , Figure 3.3 (Konietzky and Ismael 2018).

The weak points of this model are the nonlinearity and inability to derive the dimensionless constant  $m$  from logging or experimental data. Furthermore, the intermediate principal stress is not included in the criterion. These major downsides make this model uncommon in the oil industry (Rahimi 2014).

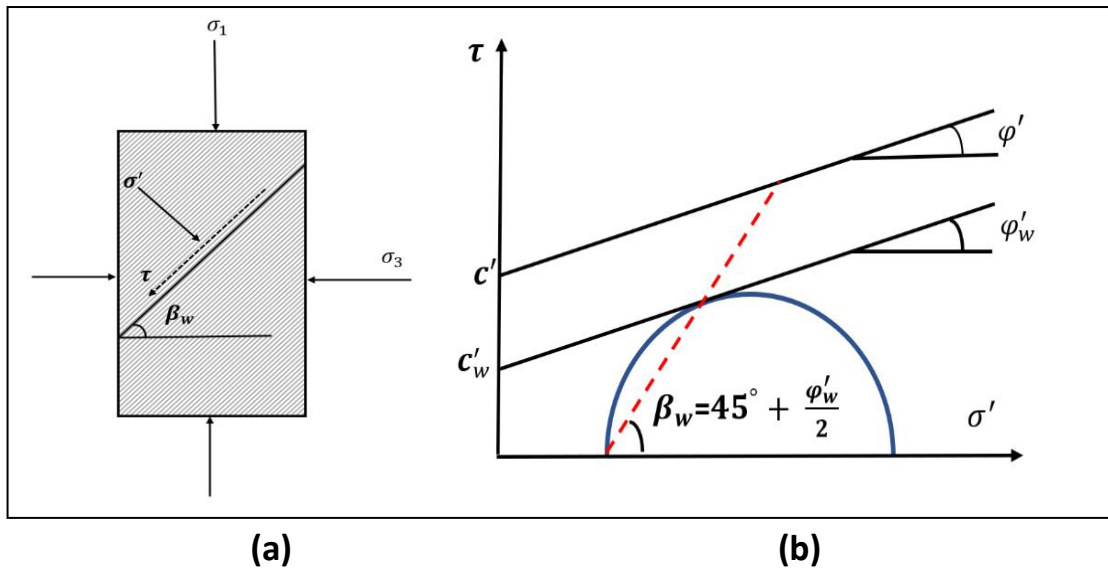


Figure 3. 4 (a), Weakness plane in TXT specimen, (b) Weakness plane model envelope, Shapes adapted from reference (Zhang et al. 2015).

### 3.3 Weakness Plane Model (Jaeger, 1960)

One of the features that expresses the distinctive nature of rocks is the presence of inherited anisotropy. This anisotropy is the result of *schistosity* and *foliation* in the cases of metamorphic rocks, lamination and bedding plane in sedimentary rocks, Figure 3.4 (a). Jaeger assumed that the rocks have the same inherent strength in all directions, with the exception of the smallest strength in one set of parallel planes. The Weakness Plane Model is one of the cardinal criteria to define failure in anisotropic rocks. The model is derived from Mohr-Coulomb, Figure 3.4 (b). Essentially, the Jaeger Model evaluates the failure in rock matrix and along the lamination in sandstone or bedding plane in shale (Deangeli and Omwanghe 2018).

Jaeger and Cook (1979) developed mathematical equations to determine the influence of discontinuity on rock mechanical strength:

$$\tau = \frac{1}{2} (\sigma_1 - \sigma_3) \sin 2\beta_w \quad (3.12)$$

$$\sigma = \frac{1}{2} (\sigma_1 + \sigma_3) + \frac{1}{2} (\sigma_1 - \sigma_3) \cos 2\beta_w \quad (3.13)$$

$$\tau_s = c'_w + \sigma' \tan \varphi'_w \quad (3.14)$$

$$(\sigma_1 - \sigma_3)_{slip} = \frac{2 (c'_w + \sigma'_3 \tan \varphi'_w)}{(1 - \tan \varphi'_w \cot \beta_w) \sin 2\beta_w} \quad (3.15)$$

Equation 3.15 is the formula to define the slip along bedding plane. Furthermore, the model predicts the maximum strength when applied stress is perpendicular to the bedding plane and minimum strength when the stress is parallel to the weakness planes (FEMI-OYEWOLE 2018).

### 3.4 Mogi-Coulomb

The previously mentioned failure criteria do not include the effect of intermediate principal stress on the ultimate rock strength. On the other hand, there are several criteria that consider the influence of  $\sigma_2$  on the failure envelope. Some of them were adopted for comparison reasons in the calculations section, in particular the Mogi-Coulomb criterion and Stassi d'Alia. Hence, True triaxial test was executed by Mogi (1971) on rock samples in order to define the footprint of  $\sigma_2$  on rock strength. Mogi implied that the fracture plane is extended to be parallel to the intermediate stress. Accordingly, the fracture is prevented from happening because of mean normal stress  $\sigma_{m2}$  not octahedral normal stress  $\sigma_{oct}$ . He proposed that the energy of distortional strain is proportionate to the  $\sigma_{oct}$ . Correspondingly, any addition in mean normal stress will lead to increasing of  $\sigma_{oct}$ , then reach the critical point which is followed by failure. Depending on these observations, Al-Ajmi and Zimmerman (2005) introduced the linearized Mogi-Coulomb criterion in the Mogi domain ( $\sigma_{oct}$  &  $\sigma_{m2}$ ). Based on the experimental results, they found that the rock strength is overestimated by Drucker-Prager and underestimated by Mohr-Coulomb (Al-Ajmi and Zimmerman 2006). Mogi-Coulomb was applied in many fields around the world and the results were identical to the field observations. Nevertheless, one of the main downsides of this criterion is the determination of  $a$  and  $b$  constants. In consequence, any increase in the number of unknowns in any mathematical relation will be reflected on the application of that relation in practice.

$$\tau_{oct} = a + b \sigma_{m2} \quad (3.16)$$

Where  $a$  and  $b$  are the constants,  $a$  is the line intersection with  $\tau_{oct}$  axis and  $b$  is the line slope, Figure 3.5. Poly axial test is rarely applied, particularly in shale rocks, but the model fitting parameters are defined from TXT. The parameters of Mohr-Coulomb

criterion have been used to define the Mogi fitting parameters. Thus, constant  $a$  is associated with internal friction and cohesion while  $b$  is related to internal friction.

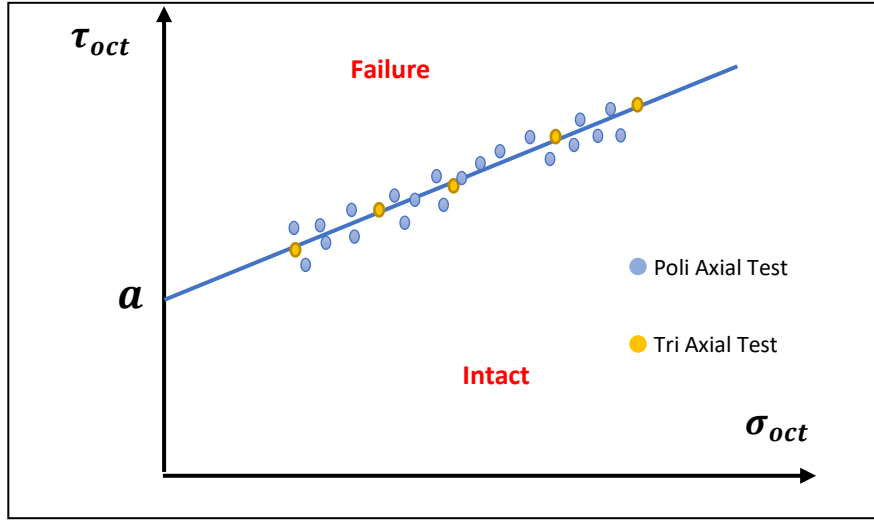


**Figure 3. 5 TTX and Poly axial test data in  $\tau_{oct}$   $\sigma_{oct}$  space to determine  $a$  and  $b$ , Image adapted from reference (Al-Ajmi and Zimmerman 2006).**

$$a = \frac{2\sqrt{2}}{3} C' \cos \varphi' \quad (3.17)$$

$$b = \frac{2\sqrt{2}}{3} \sin \varphi' \quad (3.18)$$

$$\tau_{oct} = \frac{1}{3} \sqrt{[(\sigma_1 - \sigma_3)^2 + (\sigma_2 - \sigma_3)^2 + (\sigma_3 - \sigma_1)^2]} \quad (3.19)$$

Uniaxial compressive strength  $C_0$  and uniaxial tensile strength  $T_0$  are obtained from equations (3.20) and (3.21), respectively.

$$C_0 = \frac{a}{(\sqrt{2/3}) - (b/2)} \quad (3.20)$$

$$T_0 = \frac{a}{(\sqrt{2/3}) + (b/2)} \quad (3.21)$$

Mogi-Coulomb is an extension of Mohr-Coulomb; therefore, it is turned into Mohr-Coulomb when  $\sigma_1 = \sigma_3$  or  $\sigma_2 = \sigma_3$ . The criterion has been used for the wellbore stability analysis, especially in the case of collapse failure in vertical and horizontal wells. The collapse pressure can be analyzed for various faults regimes (NF, SSF, RF). However, according to the experimental results, Al-Ajmi and Zimmerman (2006) postulated that the selection of failure criteria has no considerable impact on the borehole trajectory. It is mostly affected by the magnitude of the principal stresses. In essence, one of the most precise criteria is Mogi-Coulomb, particularly in hard rocks (Aadnøy and Looyeh 2011).

### 3.5 Stresses around a wellbore

The overburden stress, tectonic activities and local perturbations control the distribution of in-situ stresses in the underground circumstances. During drilling operations, drilling fluid is utilized to support the stressed rocks. This may cause instability in the wellbore when the fluid hydrostatic or dynamic pressure ( $P_w$ ) does not harmonize the state of stresses. Therefore, deviatoric stresses might rise to be higher than the rock mechanical strength when stresses are redistributed. This may lead to some physical problems such as wellbore collapse. For that reason, mathematical models are essential to understand the stresses behavior around the borehole after drilling and during production (Aadnøy and Looyeh 2011).

After drilling, there will be in-situ or far field stresses and stresses that surround the borehole. Any possible failure in wellbore depends on the rock strength and magnitude of these stresses (Aadnøy and Looyeh 2011). Cylindrical coordinates have been utilized to demonstrate the stresses and strains around the wellbore due to the cylindrical shape which characterizes the borehole pattern, Figure 3.6.

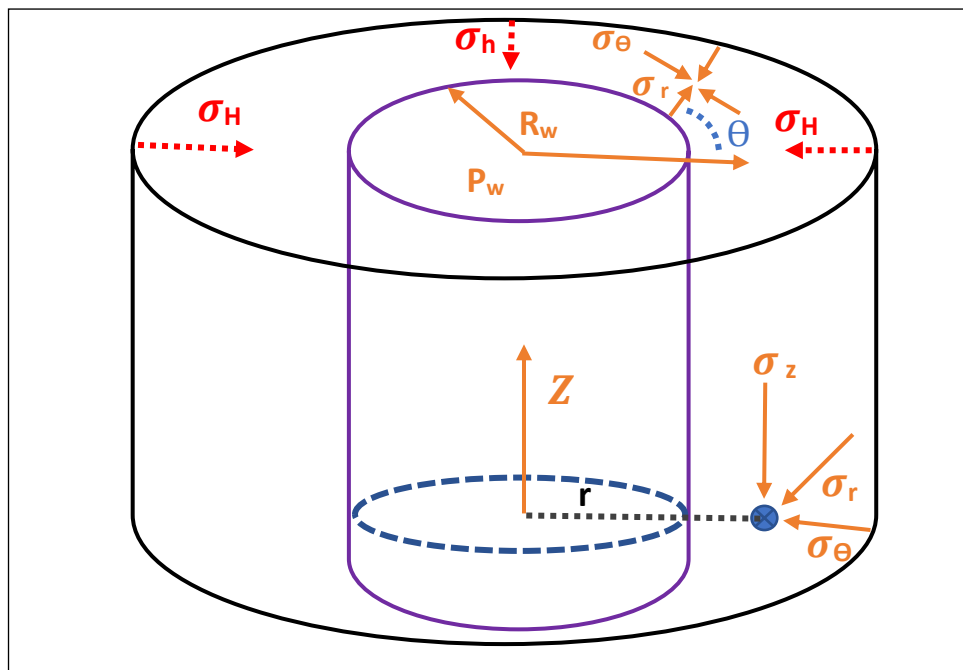


**Figure 3. 6 Stresses distribution around wellbore and far field stresses in cylindrical coordinates, figure adapted from reference (Eide, H.S. 2012).**

The formation neighbouring the wellbore is proposed to be homogeneous, so the failure may occur due to the stress concentration around the borehole. The failure may extend to 1-3 times the wellbore radii (Aadnøy and Looyeh 2011).

### 3.5.1 Lamé Solution

The Lamé Solution is a set of straightforward equations that are employed to characterize the behavior of isotropic linear elastic rocks. The general equations are:

$$\sigma_r = \sigma_h \left(1 - \frac{R_w^2}{r^2}\right) + \frac{P_w R_w^2}{r^2} \quad (3.22)$$

$$\sigma_\theta = \sigma_h \left(1 + \frac{R_w^2}{r^2}\right) - \frac{P_w R_w^2}{r^2} \quad (3.23)$$

$$\sigma_z = \sigma_v + \nu (\Delta\sigma_r + \Delta\sigma_\theta) = \sigma_v \quad (3.24)$$

Where ( $\tau_{r\theta} = \tau_{z\theta} = \tau_{zr} = 0$ ), equations (3.22) to (3.24) are used for dry materials. In saturated formations the instantaneous *poroelastic* undrained solution is considered. Thus, before any exchange between pore and wellbore fluids just after drilling, the undrained condition is dominant and pore pressure is constant, Figure 3.7. Therefore, the Lamé solution is applied, using the total stress and Skempton equation to identify the pore pressure in terms of undrained conditions (Himmelberg 2014).

$$P_{final} = \frac{1}{3} \left[ \sigma_h \left(1 - \frac{R_w^2}{r^2}\right) + \frac{P_w R_w^2}{r^2} + \sigma_h \left(1 + \frac{R_w^2}{r^2}\right) - \frac{P_w R_w^2}{r^2} + \sigma_v \right] \quad (3.25)$$

$$P_{final} = \frac{1}{3} (2\sigma_h + \sigma_v) \quad (3.26)$$

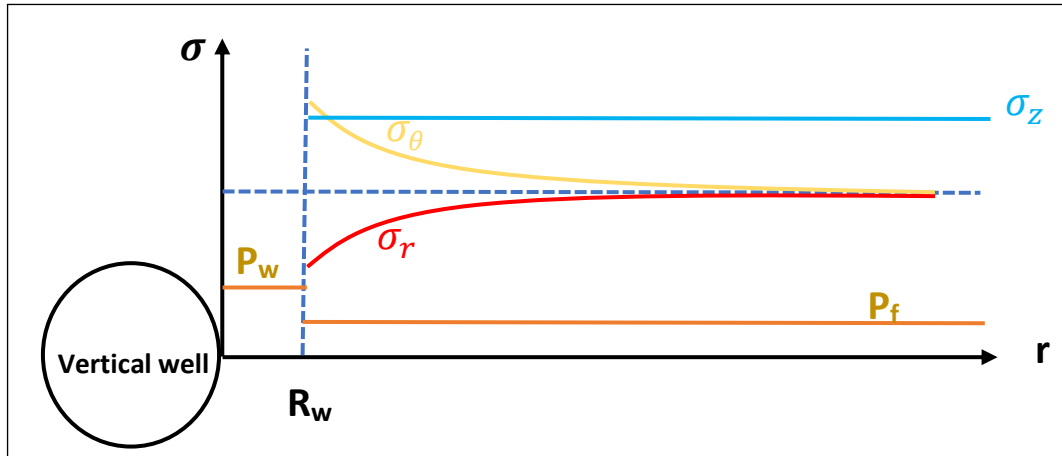


**Figure 3. 7 Stresses distribution around wellbore for constant pore pressure in linear elastic rock, Shapes adapted from reference (Fjær et al., 2008).**

On the other hand, after a specific period of time, drained condition will govern the system. Therefore, pore pressure will vary and consequently stresses adjacent to the borehole will redistribute. Thus, if the wellbore pressure is higher than the formation pressure, there will be fluid loss from drilling fluid into formation. This may lead to stress increment due to formation expansion, while exactly the opposite occurs during production. Thereafter, axial and tangential stresses will drop, and formation

contraction may happen (Fjaer et al. 2008). The distribution of stresses at wellbore can be investigated by:

$$\sigma_r = P_w \quad (3.27)$$

$$\sigma_\theta = 2\sigma_h - P_w - 2\eta(P_f - P_{Rw}) \quad (3.28)$$

$$\sigma_z = \sigma_v - 2\eta(P_f - P_{Rw}) \quad (3.29)$$

Where  $P_{Rw}$  is the formation pressure at borehole wall,  $\eta$  stands for coefficient of poroelastic stress and it is given by:

$$\eta = \frac{1-2\nu}{2(1-\nu)} \alpha \quad (3.30)$$

### 3.5.2 Kirsch Solution

In 1898 Ernst Gustav Kirsch presented his solution to define wellbore stability in anisotropic far field stresses. He assumed isotropic linear elastic rocks in his approach. The effective stresses have been computed at a point located in a circular hole

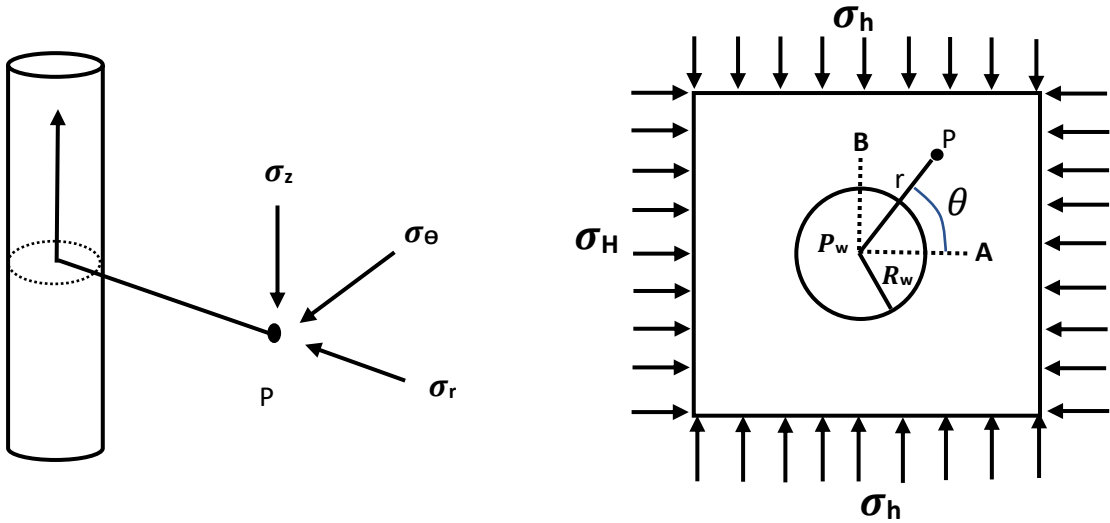


**Figure 3. 8 Stresses distribution around wellbore and far field stresses according to Kirsch Solution, Images were adapted.**

coordinate  $(r, \theta)$  drilled in an infinite plate under plane strain condition Figure 3.8. Correspondingly, effective stresses around the vertical wellbore can be resolved from the following equations:

$$\sigma_r = \left( \frac{\sigma_H + \sigma_h}{2} \right) \left( 1 - \frac{R_w^2}{r^2} \right) + \left( \frac{\sigma_H - \sigma_h}{2} \right) \left( 1 + \frac{3R_w^4}{r^4} - \frac{4R_w^2}{r^2} \right) \cos 2\theta + P_w \frac{R_w^2}{r^2} \quad (3.31)$$

$$\sigma_\theta = \left( \frac{\sigma_H + \sigma_h}{2} \right) \left( 1 + \frac{R_w^2}{r^2} \right) - \left( \frac{\sigma_H - \sigma_h}{2} \right) \left( 1 + \frac{3R_w^4}{r^4} \right) \cos 2\theta - P_w \frac{R_w^2}{r^2} \quad (3.32)$$

$$\sigma_z = \sigma_v - 2\nu (\sigma_H - \sigma_h) \frac{R_w^2}{r^2} \cos 2\theta \quad (3.33)$$

$$\tau_{r\theta} = -\left(\frac{\sigma_H - \sigma_h}{2}\right) \left(1 - \frac{3R_w^4}{r^4} + \frac{2R_w^2}{r^2}\right) \sin 2\theta + \tau_{xy} \left(1 - \frac{3R_w^4}{r^4} - \frac{2R_w^2}{r^2}\right) \cos 2\theta \quad (3.34)$$

The condition is plane strain so,  $\tau_{rz} = \tau_{\theta z} = 0$

Where  $R_w$  is the borehole radius,  $r$  is the distance from the wellbore to point P Figure 3.8.  $P_w$  stands for the wellbore pressure,  $\theta$  is the angle measured from x-axis in clockwise direction.  $\nu$  Poisson's ratio.  $\sigma_r, \sigma_\theta, \sigma_z$  are radial, tangential and axial stresses, respectively.  $\tau_{r\theta}, \tau_{rz}, \tau_{\theta z}$  are shear stresses (Aadnøy and Looyeh 2011).

The values of stresses in the borehole wall change clearly from point A ( $\theta = 0^\circ$ ) to B ( $\theta = 90^\circ$ ), Figure 3.8. The radial stress ( $\sigma_r$ ) is assumed to be equal to wellbore pressure in every borehole direction, while axial and hoop stresses are direction dependent.

$$\text{At A direction:} \quad \sigma_\theta = 3\sigma_h - \sigma_H - P_w \quad (3.35)$$

$$\sigma_z = \sigma_v - 2\nu (\sigma_H - \sigma_h) \quad (3.36)$$

$$\text{At B direction:} \quad \sigma_\theta = 3\sigma_H - \sigma_h - P_w \quad (3.37)$$

$$\sigma_z = \sigma_v + 2\nu (\sigma_H - \sigma_h) \quad (3.38)$$

If the anisotropy of the far field stresses is large, thereafter the tangential stress may become negative in equation (3.35), and tensile failure may occur in A direction. On the other hand, the axial and tangential stresses are at their maximum values in B direction. Therefore, shear failure is often happening in this direction (Zhang et al. 2006)

## **Results and Discussions of Wellbore Stability Analysis**

### **4.1 Model Parameters**

All parameters were carefully computed to establish the mechanical earth model (MEM) as close to the reality as possible. Therefore, appropriate empirical equations were employed to create a ceaseless peak of rock mechanical strength parameters, pore pressure and in-situ stresses, then specify the ultimate mud window. The log derived results were calibrated with the parameters obtained from the laboratory tests. This calibration helped to see the convergence and divergence between predicted and measured data.

The model and methodologies have been built based on logic sequences as depicted in flowchart Figure 1.4. Parameters of lab test and geophysical logs have been collected from four different wells distributed around the northern domes of Zubair field. The Pre-Drill Wells are ZB-199, drilled vertically to almost 2500 m in carbonate reservoir, and ZB-201, ZB-202 and ZB-233 which were drilled vertically to over 3500 m in sandstone reservoir, exposing them to quite long shale intervals. The most accurate, reliable and comprehensive data were gathered from well ZB-233 when most of the operations were done by Schlumberger. Finally, the results were compared with the real situations of wellbore stability in eleven wells to assess the validity of the model. The subsequent parts define the input data of the MEM.

#### **4.1.1 Overburden stress calculations**

Overburden stress is the stress caused by the cumulative rock weight combined with the fluids which saturate the rocks. As mentioned in chapter two, the overburden stress can be calculated based on equation (4.1). This formula is the integrating of the bulk density log and it is mostly used in onshore applications. Figure 4.1 represents the bulk density and calculations of vertical stress in Zubair field from 569 m to 3500 m TVD. The logs were recorded in two wells: from 569 to 1870 m TVD at a 17-1/2" hole section in exploratory well ZB-202, while from 1870 to 3190 m TVD in a 12-1/4" hole section and from 3190 to 3500 m TVD in an 8-1/2" hole section in the evaluation well ZB-233. From 569 m to surface, the bulk density was calculated by means of extrapolation.

$$\sigma_V = \int_0^Z \rho(Z)gdz \quad (4.1)$$

It is not recommended to use log data from different separated wells even if the wells are located on the same field. But, in the case of vertical stress, the only way is to originate the density of the surface layers. Thus, density origination may not give reasonable values, especially in uplifted areas or if there is an ice loading such as in the case of the North Sea field. The density in shallow depths of the North Sea is higher than the boundary of sedimentary basins due to the deglaciation (D. Zoback 2007). Therefore, all these restrictions dictate the use of log data even from different unattached wells to minimize the uncertainty.

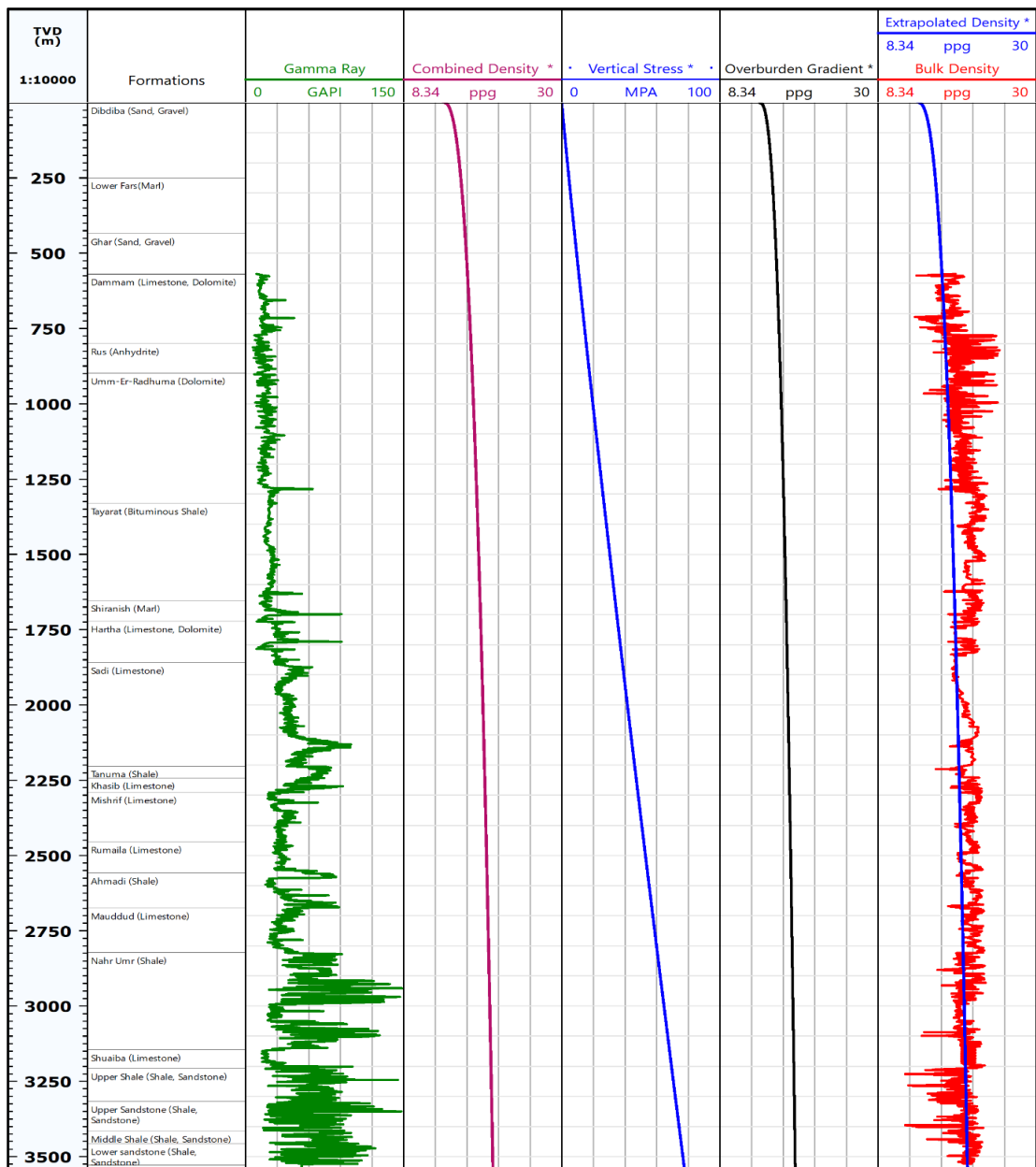


Figure 4. 1 Integrated Overburden stress, calculated based on bulk density log of Zubair field, Published with Techlog 2020.1.1.

### 4.1.2 Pore Pressure Estimation

Pore pressure assessment along the field section is a heavy task, especially in impermeable rocks. It highly affects the reservoir characterizations and consequently the geomechanics parameters. It is fundamental to measure pore pressure in production zones for well control purposes while drilling or for behalf of the reservoir engineering requirements. In wellbore stability, it is mandatory to determine the pore pressure along the proposed borehole trajectory, including non-producers. Many models are accessible to evaluate the pore pressure, some of which are normal trends and the others are explicit. Therefore, choosing the appropriate method to calculate the pore pressure is crucial in determining the reliability of the results. Detailed discussion of some techniques in chapter two identified that one of the most trustworthy methods of indirect pressure calculation is Eaton's method.

Eaton's method, in equation (4.2), was applied to define the pore pressure relying on the deep resistivity log. But, as aforementioned in chapter two, this way is accurate only in young sedimentary basins. Subsequently, pore pressure was overestimated as illustrated in Figure 4.2. The black tracks, weather in pore pressure gradient (PPG Resistivity) or pore pressure (PP Resistivity) are identical to the vertical stress line and this is not rational (Lang, Li, and Zhang 2011).

$$P_{pg} = OBG - (OBG - P_{pn})\left(\frac{R_0}{R_n}\right)^x \quad (4.2)$$

On the other hand, the second Eaton's equation is (4.3). The formula is based on the compressional wave velocity ( $\Delta t$ ). This equation was utilized to establish a continuous profile of pore pressure along permeable and nonpermeable formations. In order to validate the calculations, 37 pressure points that were previously measured with direct measurement tools were used for calibration purposes. This comparison is the principal determinant that emphasizes the calculations. However, on Figure 4.2, the green circles refer to the measured pore pressure. Although there is convergence between measured and estimated values, there are some scatters, especially in the pay zones. For instance, at the interval of 2250 to 2500 m TVD, the divergence between the two values is very clear, and the reason is depletion in the production zone. The same disagreement can be diagnosed from 3325-3375 m which is the other depleted reservoir (Zhang 2011).

$$P_{pg} = OBG - (OBG - P_{pn})\left(\frac{\Delta t_n}{\Delta t_0}\right)^x \quad (4.3)$$

In summary, Eaton's slowness equation is the pioneer indirect method of pore pressure prediction. It gives highly close values of pore pressure in all lithologies except

depleted reservoirs. Finally, probabilistic analysis has been implemented with MonCarlo process to shrink the uncertainty. The run comprised 1000 trials, the process took 46 seconds, and the outcomes were finalized as depicted in Figure 4.2.

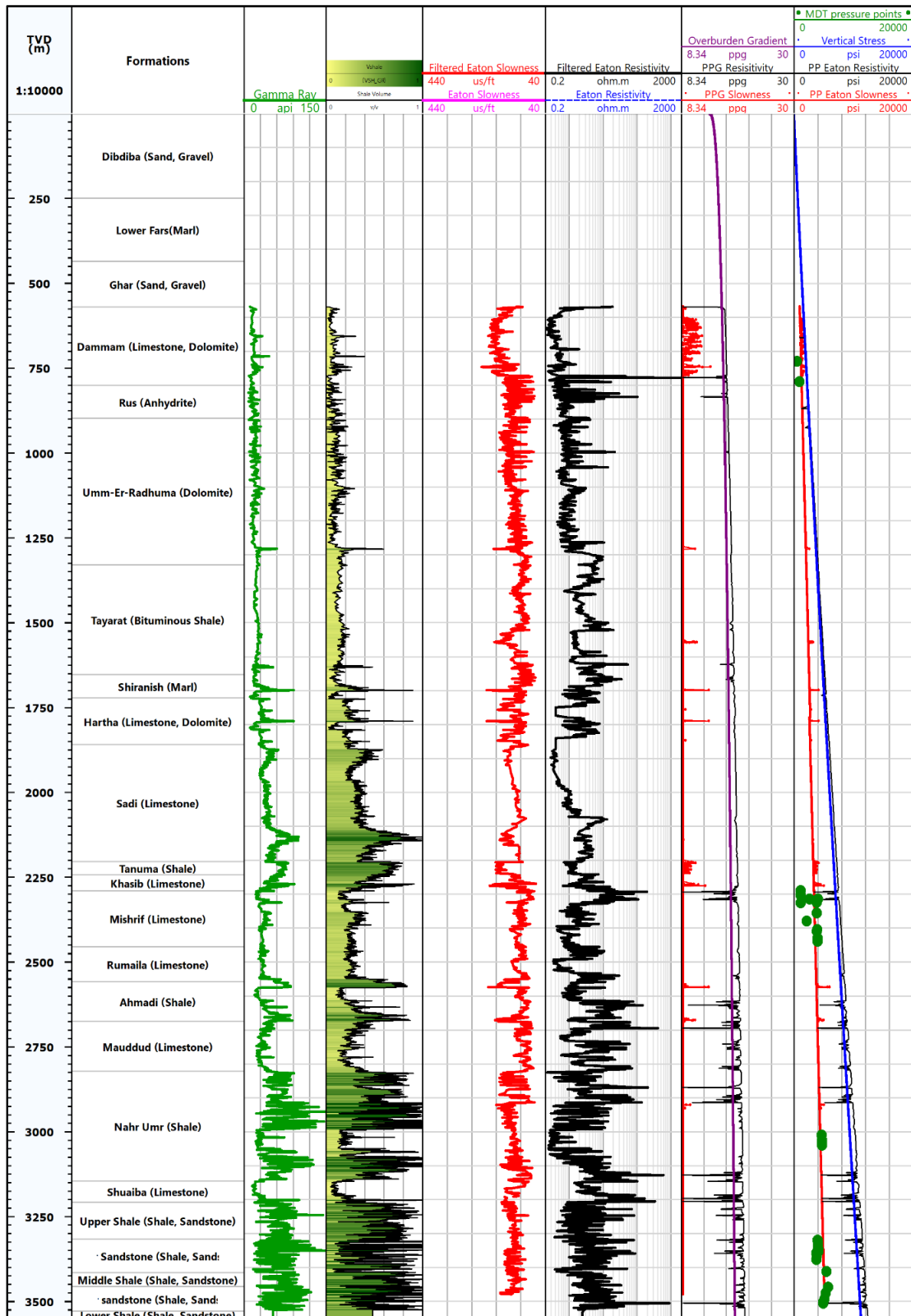


Figure 4. 2 Pore Pressure calculation according to Eaton's Resistivity and Slowness logs, Published with Techlog 2020.1.1.

### 4.1.3 Young's modulus prediction

The elastic moduli parameters are the basic building blocks of the geomechanical model. In this study, these parameters were extracted from the depth of 569 m to 3500 m TVD based on the available geophysical logs. The values were then verified by comparing them with the laboratory test data. Despite the hypothesis of the variations between static and dynamic models, the results of the calculations were acceptable and somewhat similar to the lab tests outputs.

First of all, the dynamic Young's modulus was calculated assuming that the rocks are elastic and isotropic (Ameen et al. 2009). The computations were implemented with compressional and shear wave velocities in addition to the density logs in order to define the shear and bulk moduli with equations (4.4) and (4.5).

$$G_{dyn} = 13474.45 \frac{\rho_b}{(\Delta t_{shear})^2} \quad (4.4)$$

$$K_{dyn} = 13474.45 \rho_b \left[ \frac{1}{(\Delta t_{comp})^2} \right] - \frac{3}{4} G_{dyn} \quad (4.5)$$

These two equations were applied to derive the final equation (4.6), which in turn was exploited to calculate the ultimate value of the dynamic Young's modulus.

$$E_{dyn} = \frac{9G_{dyn} \times K_{dyn}}{G_{dyn} + 3K_{dyn}} \quad (4.6)$$

Correlation techniques that are available to extract the static Young's modulus from dynamic Young's modulus include the Morales, Modified Morales, Plumb Bradford and John Fuller correlations. The reason for extraction is that the rock's mechanical strength is sonic velocity independent, particularly in high porous medium circumstances. Therefore, the conventional sonic logs may not produce convenient results in comparison with laboratory test (Ameen et al., 2009). Nevertheless, one of the most acceptable approaches to make this correlation is John Fuller. The correlation is based on a sandstone investigation which was conducted in the North Sea. Equation 4.7 (Bradford et al. 1998) was executed to obtain the  $E_{stat}$  in this thesis:

$$E_{stat} = 0.0018 E_{dyn}^{2.7} \quad (4.7)$$

All previous steps were applied to obtain the Young's modulus as exhibited in Figure 4.3. There is tolerable rapprochement between what was built based on sonic logs and Triaxial test data. The first interval of comparison is 2290 m to 2454 m TVD. The comparison shows consistent results except for two points which may be scatters or laboratory interpretation faults. On the other hand, the number of unmatched points is higher at 3316 m to 3500 m TVD. Various reasons can govern that divergence. The

lithology is shale interbedded with sandstone as corroborated by Gamma Ray and Shale Volume indicator; thus, the interval is enlarged due to the wellbore instability as clarified in the three-dimensional borehole shape, Figure 4.11. This enlargement may adjust the sonic log readings and consequently the log derived Young's modulus. The other reason is the reliability of the Triaxial test and its interpretation.

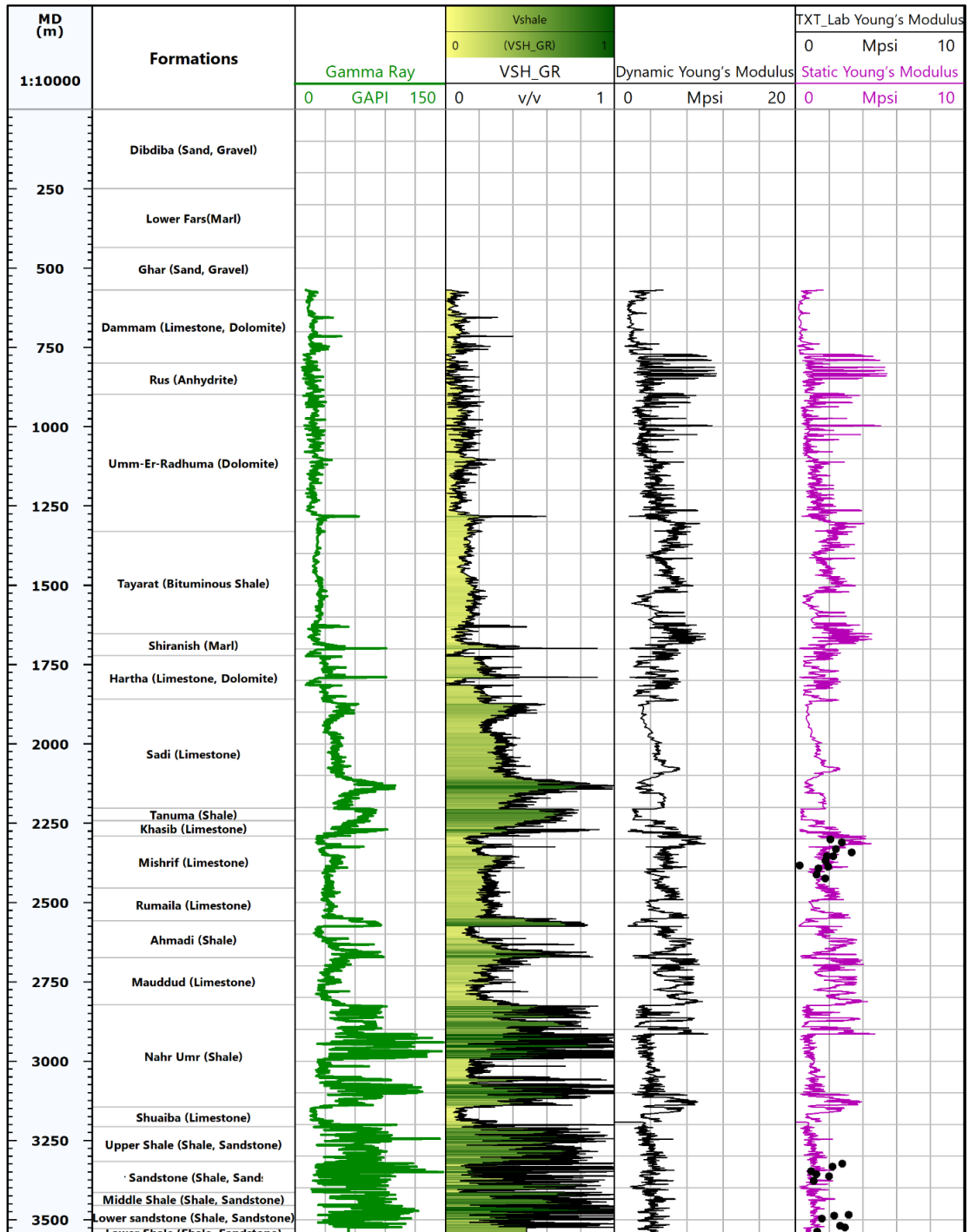


Figure 4. 3 Young's modulus prediction, Published with Techlog 2020.1.1.

#### 4.1.4 Poisson's ratio estimation

A continuous profile of dynamic Poisson's ratio was expressed based on equation (4.8), and then static values were assessed from the dynamic one (Al-Ameri and Al-Kattan 2012).

$$v_{dyn} = \frac{3K_{dyn} - 2G_{dyn}}{6K_{dyn} + 2G_{dyn}} \quad (4.8)$$

There are some incomparable points but in general the congruence between measurable points and estimated  $v_{dyn}$  is plausible, Figure 4.4.

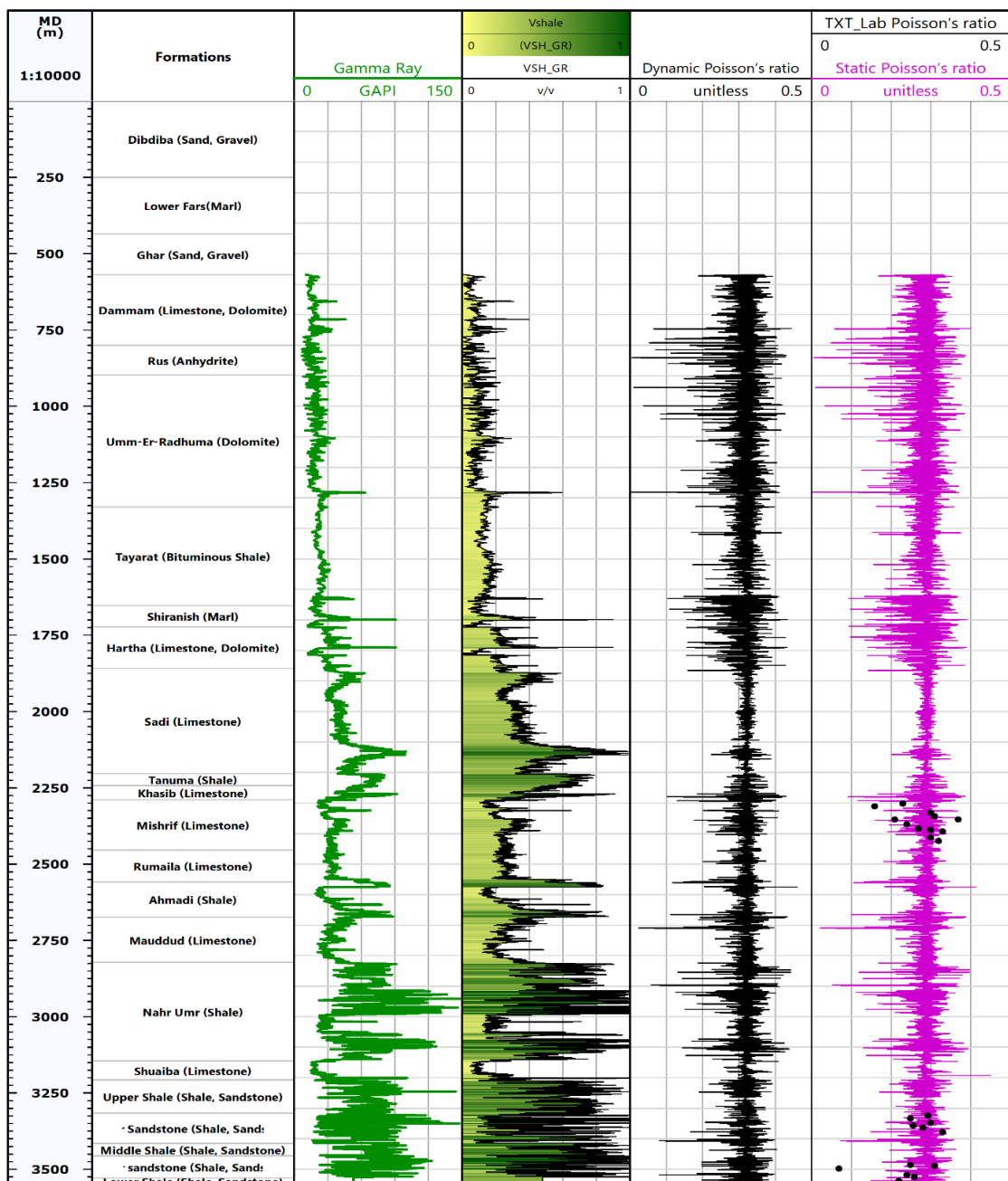


Figure 4. 4 Poisson's ratio estimation, Published with Techlog 2020.1.1.

#### 4.1.5 Evaluation of Uniaxial Compressive Strength

UCS is the vigorous player in determining the type of failure criterion as previously discussed in the third chapter. Therefore, the accuracy of the compressive strength estimation is the final word on the reliability of eventual calculations (Xu et al. 2016). In this study, the laboratory tests data were employed from tests. TXT was conducted on several core samples of different lithologies along the drilled section. Thereafter, an uninterrupted track of UCS was created from 569 m to 3500 m TVD using empirical correlations. The selection of the right empirical correlation is extremely essential, since the correlation used in one territory is not appropriate to another.

In order to avoid all these obstacles, great effort was made in this study to select the proper correlation. Several models have been fulfilled, including Coates Denoo, Brie Shear Modulus Clay, Plumb Shear Modulus, plumb porosity correlations Clay, plumb porosity correlations grain, plumb porosity upper bound, Horsrud Shale correlation and static Young's modulus correlations. After comparing the results with the TXT data, it became clear that the closest one to the lab results is the static Young's modulus correlations. Therefore, it was adopted in the final calculations.

$$UCS = 330.7 + 0.0041 E_{stat} \quad (4.9)$$

Where  $E_{stat}$  stands for static Young's modulus (Khaksar et al. 2009).

The blue track in Figure 4.5 accounts for the dynamic UCS, while black dots are the TXT UCS. There is contradiction between laboratory and log derived UCS at the carbonate reservoir in Mishrif Limestone from 2255 to 2260 m. The same discrepancy can be seen in the interval of 2275-2285m, while there is obvious match in all remaining spots. This identified incomparable in the aforementioned points is probably due to the inconvenience of applying this model to carbonate rocks. On the other hand, there is tolerable rapprochement in most of the stations recorded in the second sandstone reservoir from 3250 – 3500 m.

#### 4.1.6 Friction angle & Cohesion prediction

The other two parameters of rock compressive strength that are depicted in Figure 4.5 are Friction angle and Cohesion. Dynamic friction angle was calculated based on equations (2.47) and (2.48) for shaly sedimentary rock and shale respectively (D. Zoback 2007). While equation (2.49) was applied for sandstone (Peng and Zhang 2007).

The first section shows an acceptable closeness, except for some points that recorded values smaller than the model. However, the biggest inconsistency appeared in the second interval where most of the recorded spots are higher than the log derived track. Duncan C.Wyllie, in 1933, restricted the friction angle of sedimentary rocks in the range of 20-40 deg. Accordingly, the predicted profile is more convincing than the exaggerated TXT values in this study.

The other parameter is Cohesion, which in the carbonate reservoir is smaller than estimated, while in the sandstone reservoir it exhibits very good agreement.

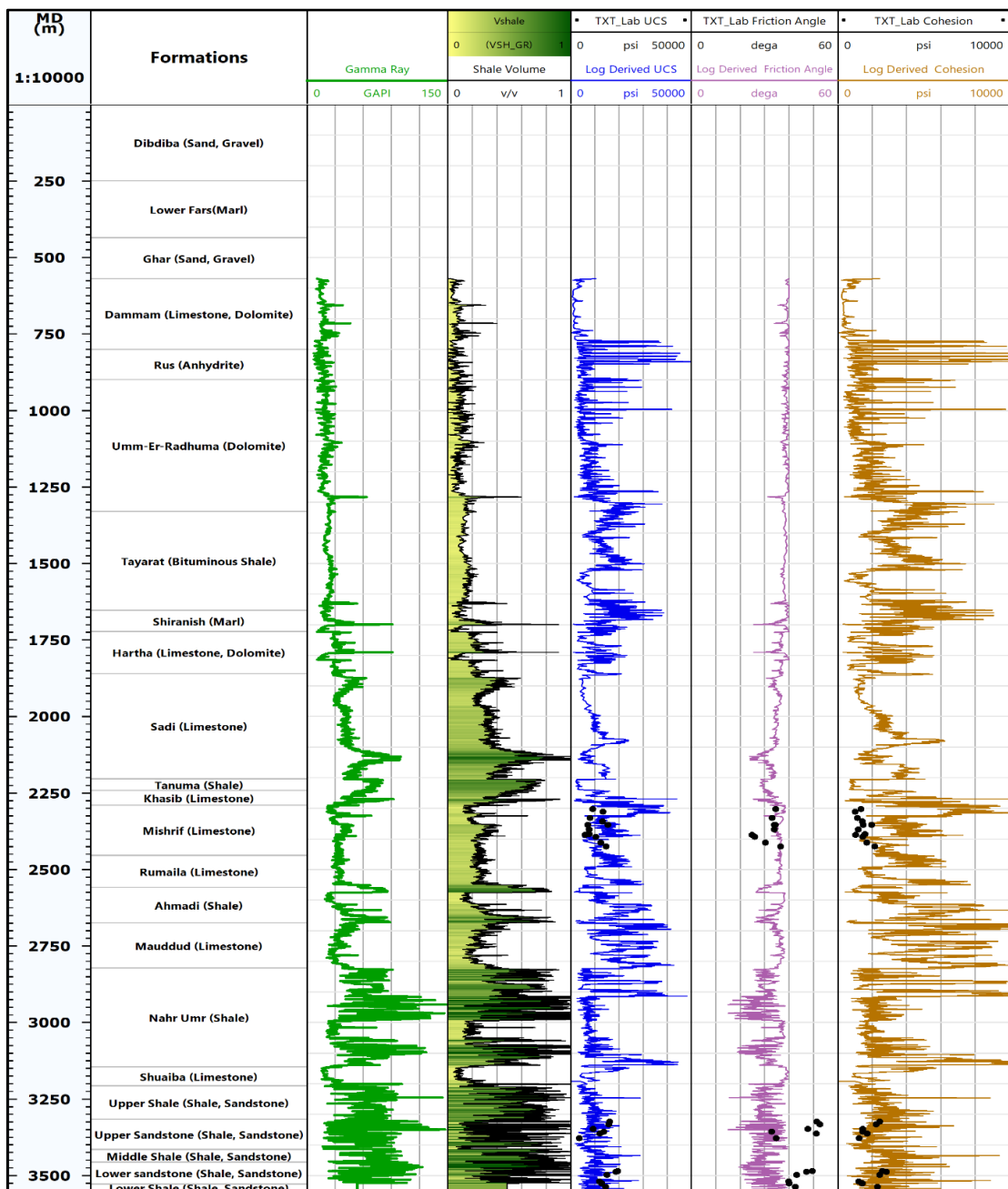


Figure 4. 5 UCS, Friction angle and cohesion prediction, Published with Techlog 2020.1.1.

### 4.1.7 Tensile Strength assessment

This variable is one of the most intractable parameters to be specified as explained and simplified in the second chapter. Equation (2.42) was utilized to construct a continuous track of tensile strength as illustrated in Figure 4.6. Thereafter, the track was calibrated with the Brazilian tensile strength.

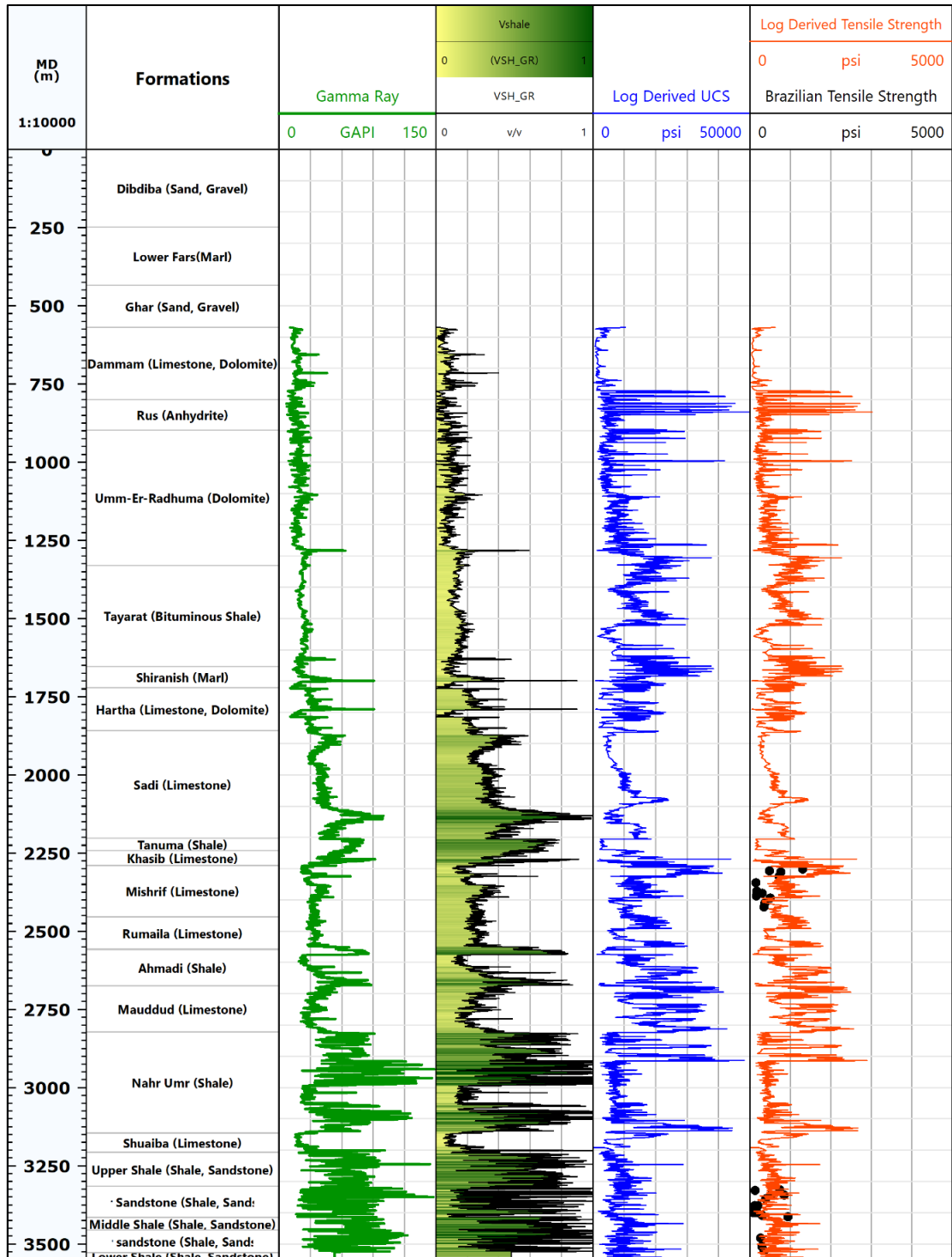


Figure 4. 6 Tensile strength, Published with Techlog 2020.1.1.

#### 4.1.8 Horizontal stresses calculation by Poro-Elastic Horizontal strain model

Incessant tracks of horizontal stresses are excessively substantial for hydraulic fracturing and wellbore trajectory design in deviated wells (Song 2012). Many models are dedicated for that purpose. Poro-Elastic Horizontal strain is one of the most dependable techniques utilized nowadays to define the maximum and minimum horizontal stresses. In this model, distortion impact and horizontal strain are considered. Therefore, Hooke's Law, Poisson ratio, overburden stress, Young's modulus and Biot's constant are employed to express the terminal relations. Finally, strain relationships and horizontal stresses can be derived as typified in equations (4.10) and (4.11) (Hayavi and Abdideh 2016).

$$\sigma_h = \frac{v_{stat}}{1-v_{stat}} \sigma_v - \frac{v_{stat}}{1-v_{stat}} \alpha P_o + \alpha P_o + \frac{E_{stat}}{1-v_{stat}^2} \varepsilon_h + \frac{v_{stat} E_{stat}}{1-v_{stat}^2} \varepsilon_H \quad (4.10)$$

$$\sigma_H = \frac{v_{stat}}{1-v_{stat}} \sigma_v - \frac{v_{stat}}{1-v_{stat}} \alpha P_o + \alpha P_o + \frac{E_{stat}}{1-v_{stat}^2} \varepsilon_H + \frac{v_{stat} E_{stat}}{1-v_{stat}^2} \varepsilon_h \quad (4.11)$$

Where  $v_{stat}$  stands for static Poisson ratio,  $E_{stat}$  is static Young's modulus,  $\alpha$  is Biot's constant,  $P_o$  is pore pressure. Tectonic strains are abbreviated as  $\varepsilon_h$ ,  $\varepsilon_H$ , these two variables can be defined by equations (4.12) and (4.13) (Kidambi and Kumar 2016).

$$\varepsilon_H = \frac{\sigma_v v_{stat}}{E_{stat}} \left( \frac{1}{1-v_{stat}} - 1 \right) \quad (4.12)$$

$$\varepsilon_h = \frac{\sigma_v v_{stat}}{E_{stat}} \left( 1 - \frac{v_{stat}^2}{1-v_{stat}} \right) \quad (4.13)$$

The preceding formulae were applied to draw  $\sigma_H$  and  $\sigma_h$  across the Dammam to the Lower shale formations at 569- 3500 m. Minimum horizontal stress as exhibited in the blue track was advocated with hydro-Frac points at four depths, Figure 4.7. All of the calibration stations revealed adequate resemblance. Whereas, there is no specific process to validate the profile in maximum horizontal stress.

As stated by Anderson's classification of fault regimes, strike slip fault was diagnosed from the Dammam formation at 569 m to the top of the Nahr Umr at 2822 m, except for Sadi limestone section. At Sadi formation (1850 – 2150 m TVD) the regime is normal fault. On the other hand, from 2822 to 3500 m the regime is normal fault unless Shuaiba formation (3145 – 3200 m TVD) where the fault is strike slip. There are short intervals with reverse and strike slip faults in between, but they were not mentioned in order to avoid verbiage. The faults distribution according to the horizontal stresses calculations might be compatible with the field seismic interpretation. Seismic data emphasize significant differences in the shape, dimension,

displacement and density of faults' structure between the Jurassic and Cretaceous sequences of the field (Geophysical Support 2013 and 2014 Seismic Horizons Interpretation, Field Data). Basically, faults categorization has considerable impact on the deviation and well direction whether the trajectory is parallel to  $\sigma_v$ ,  $\sigma_H$  or  $\sigma_h$  (D. Zoback 2007).

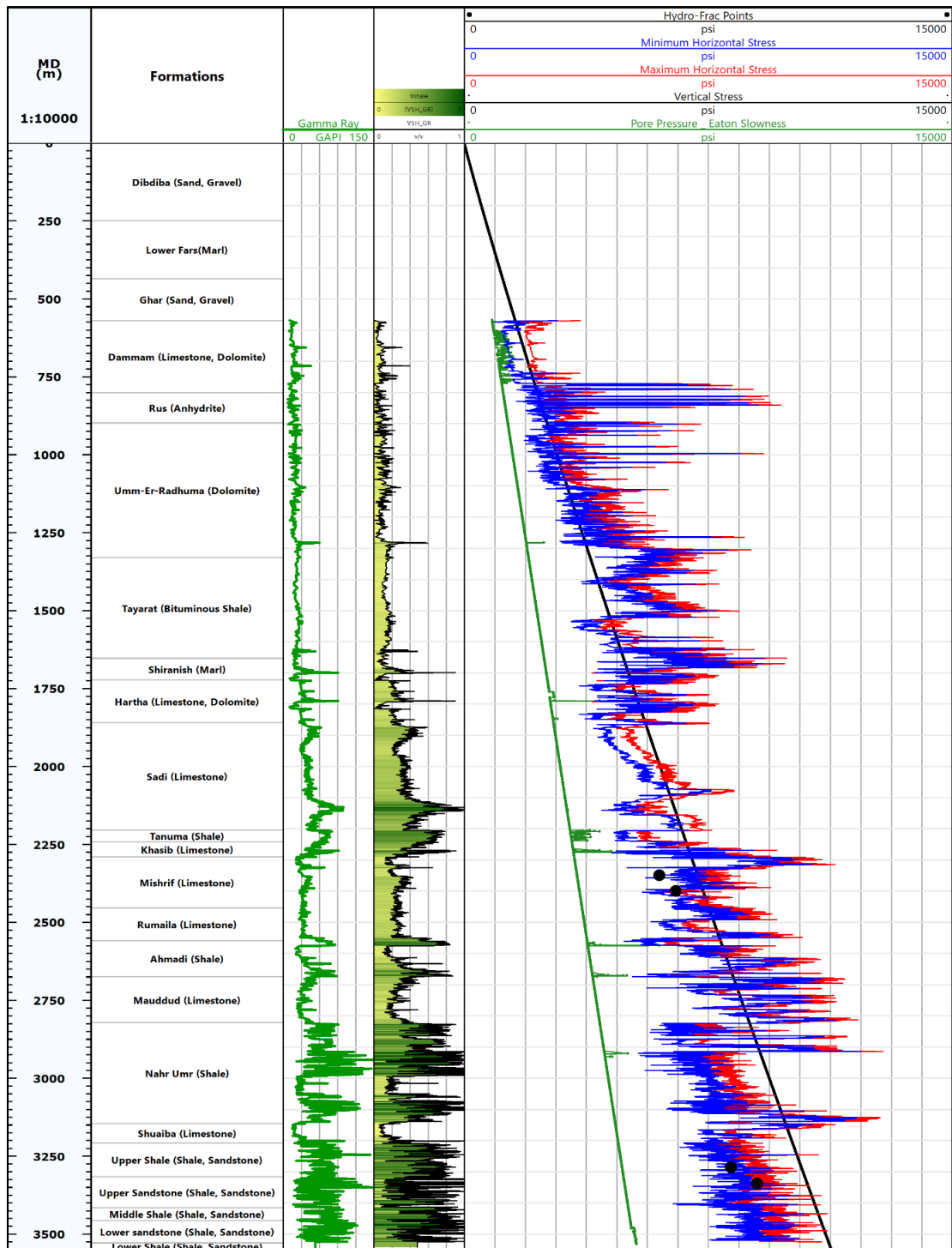


**Figure 4. 7 Horizontal stresses in Poro-Elastic Horizontal strain model, Published with Techlog 2020.1.1.**

#### 4.1.9 Horizontal stresses prediction by Mohr-Coulomb stress

The association between two principal stresses in rocks that are in a mechanical failure can be given by the Mohr-Coulomb stress model. The concept postulates that the maximum principal stress is ruled by the rock shear strength which is described by the Mohr-Coulomb criterion. The model is not restricted to any failure mechanism. It can be fulfilled at any territory whether under extensional or compressional activities.  $\sigma_H$  and  $\sigma_h$  in Figure 4.8 were calculated based on equations (4.14) and (4.15):

$$\sigma_H = \tan^2\left(\frac{\pi}{4} + \frac{\theta}{2}\right) \times (\sigma_v - \alpha P_o) + \alpha P_o \quad (4.14)$$

$$\sigma_h = \frac{(\sigma_v - \alpha P_o)}{\tan^2\left(\frac{\pi}{4} + \frac{\theta}{2}\right)} + \alpha P_o \quad (4.15)$$

Where  $\theta$  is friction angle,  $\alpha$  is Biot's constant and  $\sigma_v$  is vertical stress (Schlumberger's Techlog 2020.1).

The results are completely different from those defined with the Poro-Elastic Horizontal strain. The fault is strike slip fault from top to bottom and this contradicts the seismic data of the field. Moreover, the minimum horizontal stress is not compatible with the hydro-frac points, Figure 4.8. Therefore, the Poro-Elastic Horizontal strain model was considered for the construction of the MEM in the next steps.

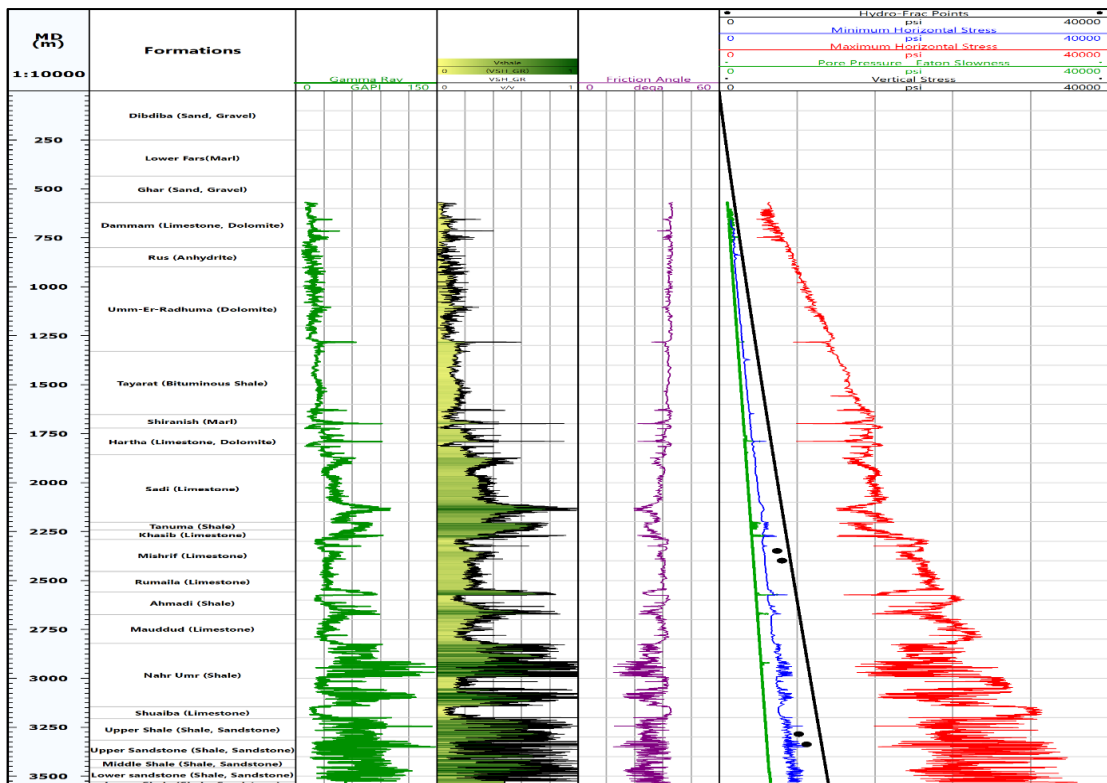


Figure 4. 8 Horizontal stresses prediction by Mohr-Coulomb stress model, Published with Techlog 2020.1.1.

#### 4.1.10 Maximum Horizontal stress from frictional faulting theory

Maximum horizontal stress can be constrained between upper and lower limit. That depends on the relation of the frictional faulting theory and borehole stresses incorporated with the wellbore failure. Thus, stress polygons have been drawn in two intervals in order to calibrate the results of Poro-Elastic Horizontal strain Model. However, the following formulae were applied on MATLAB to build the stress polygons, see appendix A and B.

$$\mu = \tan \varphi' \quad 4.16$$

$$\frac{\sigma_v - P_p}{\sigma_h - P_p} = \left[ \sqrt{\mu^2 + 1} + \mu \right]^2 \quad 4.17$$

$$\frac{\sigma_H - P_p}{\sigma_v - P_p} = \left[ \sqrt{\mu^2 + 1} + \mu \right]^2 \quad 4.18$$

$$\sigma_H = 3\sigma_h - 2P_p - \Delta P - T_0 - \sigma^{\Delta T} \quad 4.19$$

$$\sigma_H = \frac{[UCS + 2P_p + \Delta P + \sigma^{\Delta T}] - \sigma_h [1 + 2 \cos(\pi - W_{bo})]}{1 - 2 \cos(\pi - W_{bo})} \quad 4.20$$

Where  $\mu$  is coefficient of friction,  $\Delta P$  is an extra pore pressure due to the mud weight,  $\sigma^{\Delta T}$  is thermal stress and it was neglected.  $W_{bo}$  is the breakout width (D. Zoback 2007)

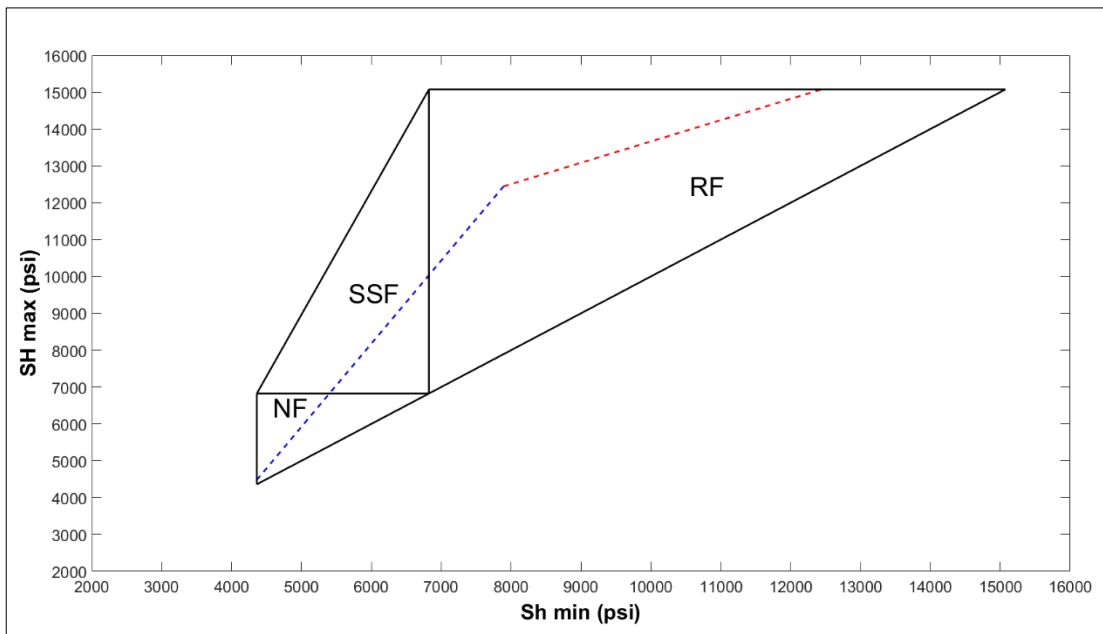


**Figure 4. 9 Stress Polygon of Tanuma formation at 2224 m, Published with MATLAB® R2019b**

The stress polygon in Figure 4.9 was implemented in Tanuma formation at 2224 m. The segmented red and blue lines are the maximum horizontal stress constraints that

calculated based on the wellbore breakout. The breakout width has been exploited from the formation imager processing as depicted in Figures 4.12 and 4.13. Thus, the minimum horizontal stress is 4650 psi at 2224 m and by using the upper limit of maximum horizontal stress,  $\sigma_H$  is 5500 psi. Whereas  $\sigma_H$  is 5332 psi in Poro-Elastic Horizontal strain Model Figure 4.9. Generally, the two numbers are reasonably close.

Another polygon was established to emphasize the magnitude of  $\sigma_H$  of the middle shale formation at 3376 m Figure 4.10.  $\sigma_H$  Lower limit is 9300 psi while upper limit is 10600 psi in normal faulting domain, and this is convenient with the Anderson's fault classification of Zubair field see the previous sections. On the other hand, the predicted maximum horizontal stress is 10019 psi according to the Poro-Elastic Horizontal strain Model, and this value is contained within the polygon upper/lower limits.

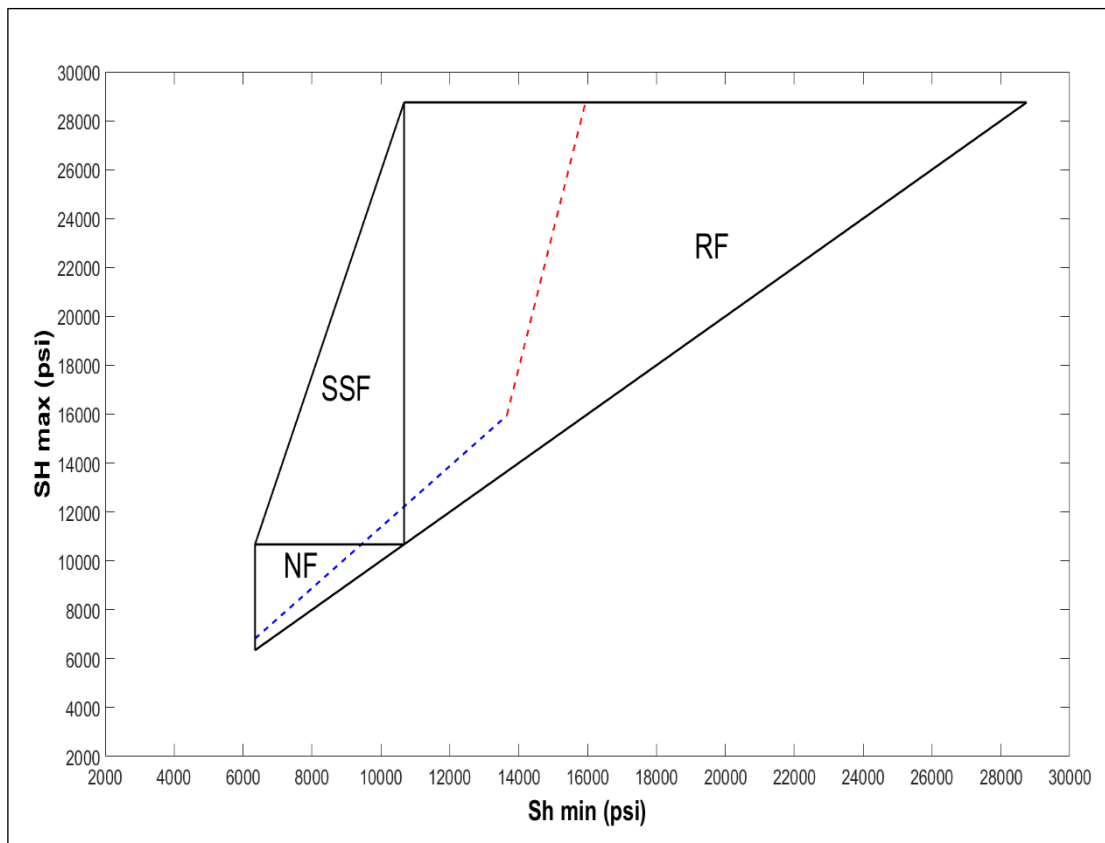


**Figure 4. 10 Stress Polygon of middle shale formation at 3376 m, Published with MATLAB® R2019b**

The last two depths were chosen to ensure the validity of the values that obtained from the other model. Because the other model was formed depending on the compressional and shear wave velocities, which in turn are greatly affected by the borehole enlargement due to the geomechanical circumstances.

## 4.2 Direction of Horizontal stresses

The orientation of horizontal stresses performs a substantial function in appreciating the risk of borehole collapse while drilling and in hydraulic fracturing design (Ezati and Soleimani 2014). The directions can be detected by the world stress map field, Figure 4.11, or by using geophysical logs such as 4 arms caliper log and Formation Micro Imager (FMI). Moreover, a new methodology has been adopted for that purpose that is called the micro seismic focal mechanism (Agharazi 2016). However, caliper and imager logs remain the most accurate and commonly used in the oil industry.

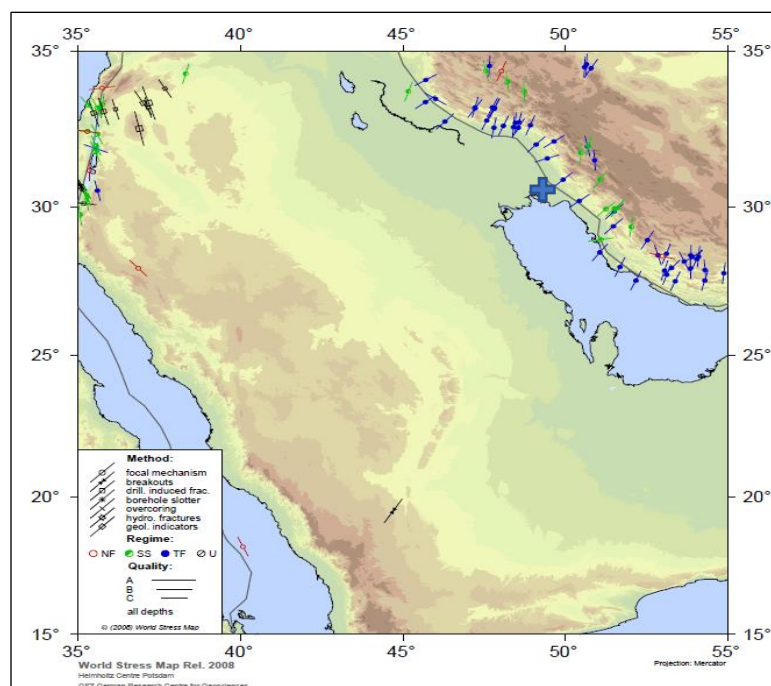


**Figure 4. 11 Stress map of Zubair field and surrounding area (World Stress Map Rel.2008).**

Caliper and Formation Micro Imager were utilized to investigate the stresses orientation. Straightforwardly, FMI can detect the azimuth of breakout and drilling induced tensile fractures as well as the natural fractures. Therefore, Schlumberger's raw FMI-HD data of ZB-227 and ZB-233 were processed with Maxwell acquisition system, Figures 4.12 and 4.13. Thus, breakouts and induced fractures were picked out manually for most intervals of FMI 4 pads. Thereafter, stereonet plots were generated in order to statistically classify the directions of collapse and tensile fractures, Figures 4.12, 4.13. The red arrows refer to the direction of breakout, while blue ones are the induced tensile fractures azimuth. The direction of maximum horizontal stress is along the tensile fractures orientation with approximately 60 deg. NE. Importantly, the results of FMI processing are fairly compatible with the World Stress Map Field in both wells. On the

other hand, the breakout direction is 150 deg. SE. Hence, any disagreement, whether slightly greater or smaller than the previously determined values, can be a consequence of log reliability or the well conditions while recording FMI data.

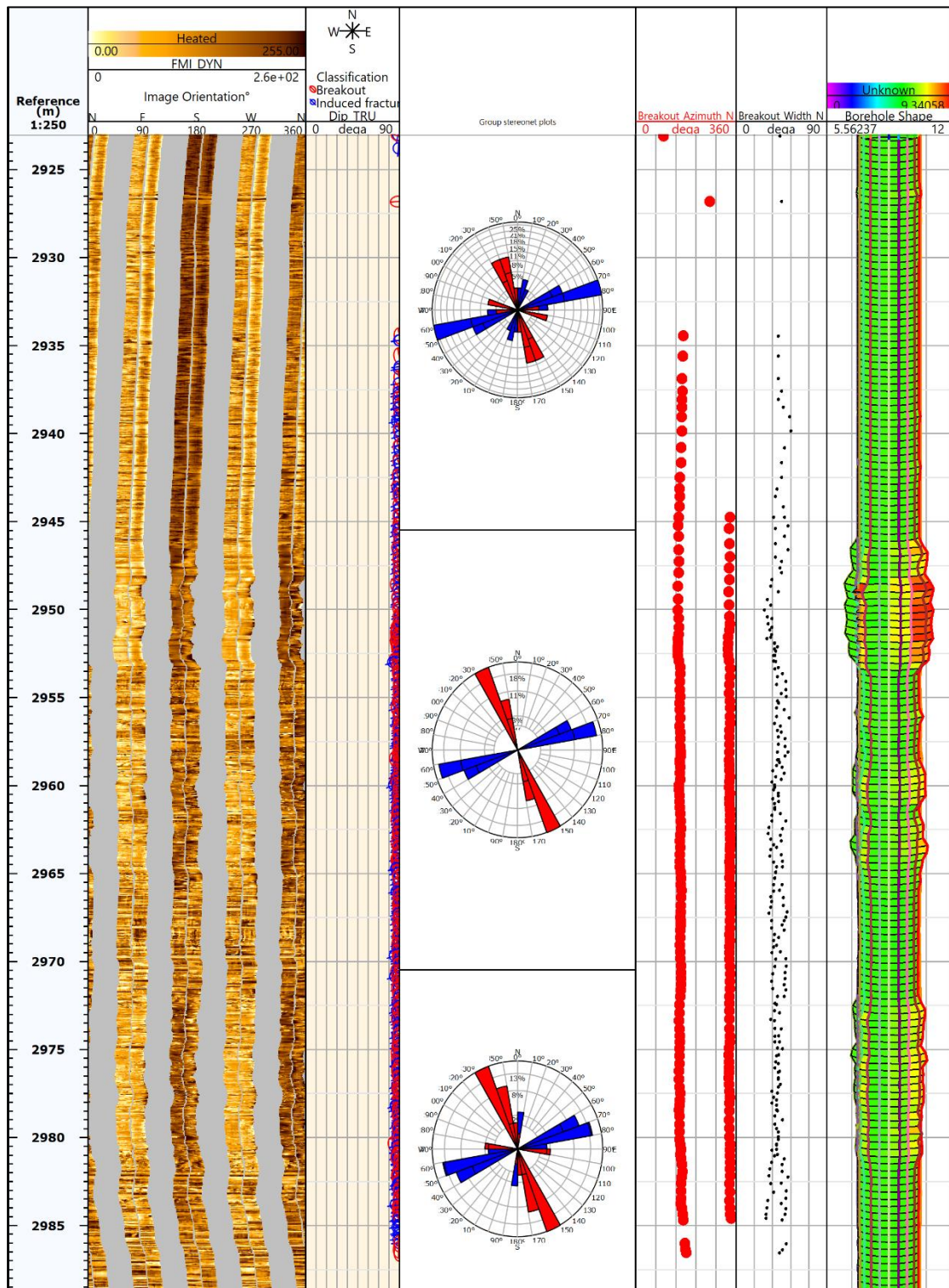


**Figure 4. 12 FMI processing and horizontal stresses directions, processing at 12.25" hole section ZB-227, Published with Techlog 2020.1.1.**

Borehole imaging of another interval under the influence of shear failure was processed. The objective of this step is to confirm the predetermined direction of the horizontal stresses. Fundamentally, the existence of deformations in the borehole adversely affects the accuracy of the well log readings. However, in the analysis of the FMI data, both wells gave similar values of stresses orientation whether in intact or over-gauged intervals.

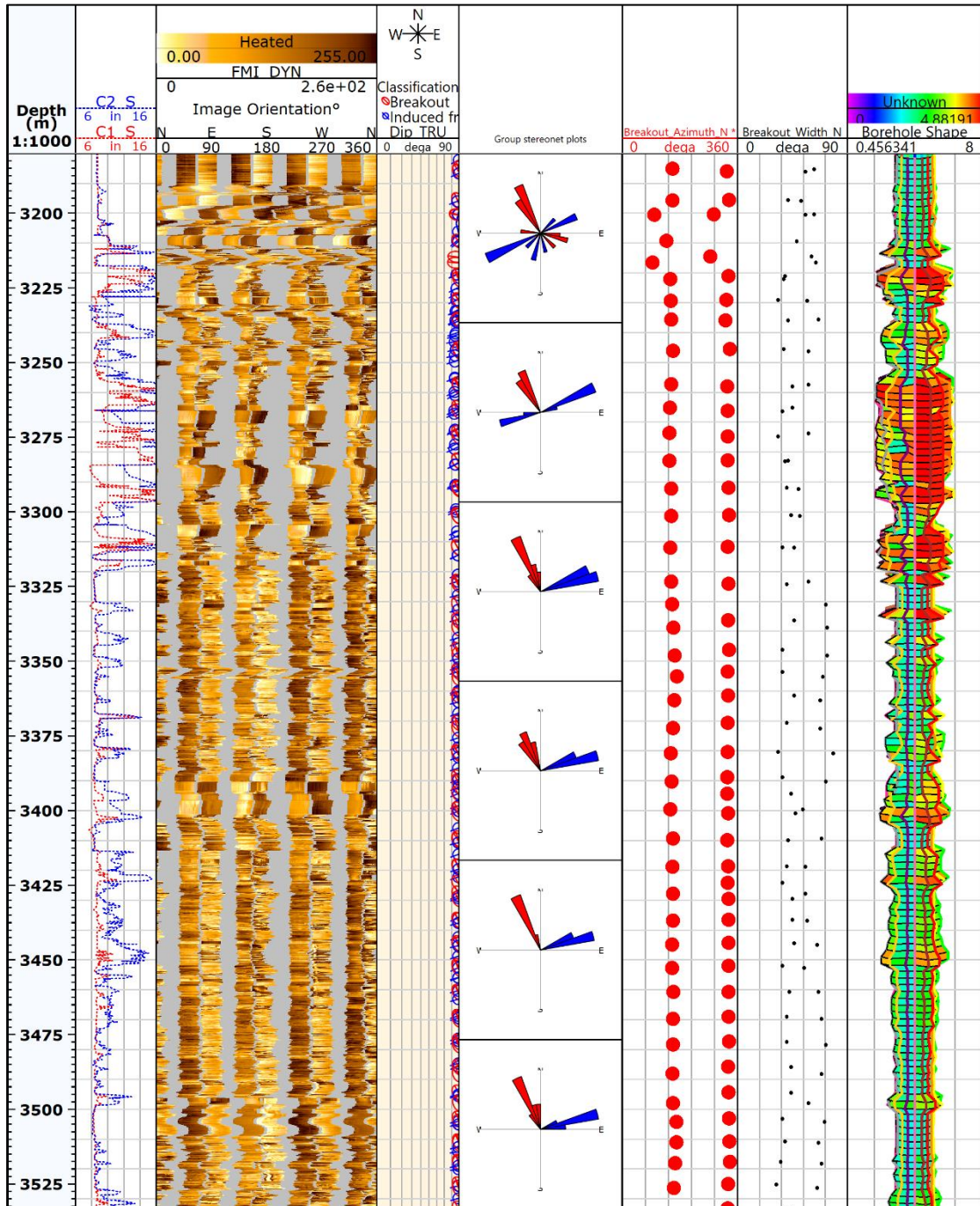


Figure 4. 13 FMI processing and horizontal stresses directions, processing at 8.5" hole section, Published with Techlog 2020.1.1.

### 4.3 Wellbore stability analysis with Mohr-Coulomb criterion

This criterion is one of the predominant methods to establish wellbore stability analysis because of its simplicity (Horsrud 2001). The criterion has been executed in this study to construct mud window (MW) and compare the results with the actual well status, Figure 4.12. Mud window is the mud weight boundary: if mud density is higher than the limit then tensile failure will take place, whereas the lower limit means collapse failure (Aslannezhad et al. 2016). Thus, Mohr–Coulomb equations with field stress characteristic and rock mechanical parameters were used to construct an optimized MW by means of the following equations. Firstly, to determine the commencement of shear failure, the stresses magnitude around the borehole must be calculated based on the subsequent equations:

$$\sigma_{\theta}^{max} = 3\sigma_H - \sigma_h - P_w \quad (4.21)$$

$$\sigma_r = P_w \quad (4.22)$$

$$\sigma_z = \sigma_v + 2\nu(\sigma_H - \sigma_h) \quad (4.23)$$

For drilling induced tensile failure initiation, the following equations are obeyed:

$$\sigma_{\theta}^{min} = 3\sigma_h - \sigma_H - P_w \quad (4.24)$$

$$\sigma_r = P_w \quad (4.25)$$

$$\sigma_z = \sigma_v - 2\nu(\sigma_{max} - \sigma_{min}) \quad (4.26)$$

The equations to create the MW are presented in the next tables.

**Table 4. 1 Shear failure equations in vertical well based on Mohr-Coulomb.**

Borehole stresses	Shear Failure Mohr-Coulomb
$\sigma'_z \geq \sigma'_\theta \geq \sigma'_r$	$P_{w(BO)} = [\sigma_v + 2\nu(\sigma_{max} - \sigma_{min}) - UCS]/[\tan^2(\pi/4 + \varphi'/2)]$
$\sigma'_\theta \geq \sigma'_z \geq \sigma'_r$	$P_{w(BO)} = [3\sigma_{max} - \sigma_{min} - UCS]/[1 + \tan^2(\pi/4 + \varphi'/2)]$
$\sigma'_\theta \geq \sigma'_r \geq \sigma'_z$	$P_{w(BO)} = 3\sigma_{max} - \sigma_{min} - UCS - [\sigma_v + 2\nu(\sigma_{max} - \sigma_{min})][\tan^2(\pi/4 + \varphi'/2)]$

**Table 4. 2 Tensile failure equations in vertical well based on Mohr-Coulomb.**

Borehole stresses	Tensile Failure Mohr-Coulomb
$\sigma'_r \geq \sigma'_\theta \geq \sigma'_z$	$P_{w(frac)} = UCS + [\tan^2(\pi/4 + \varphi'/2)][\sigma_v - 2\nu(\sigma_{max} - \sigma_{min})]$
$\sigma'_r \geq \sigma'_z \geq \sigma'_\theta$	$P_{w(frac)} = [UCS + (3\sigma_{min} - \sigma_{max})(\tan^2(\pi/4 + \varphi'/2))]/[1 + \tan^2(\pi/4 + \varphi'/2)]$
$\sigma'_z \geq \sigma'_r \geq \sigma'_\theta$	$P_{w(frac)} = ([UCS - \sigma_v + 2\nu(\sigma_{max} - \sigma_{min})]/[\tan^2(\pi/4 + \varphi'/2)]) + (3\sigma_{min} - \sigma_{max})$

The implementation of the Mohr-Coulomb criterion to build a complete analysis of wellbore stability displayed fluctuated matching between caliper log and predicted failure, Figure 4.14. More details are provided in the next pages with extended scale. Therefore, caliper and estimated deformation were compared at some intervals that experience geomechanics complications while drilling.

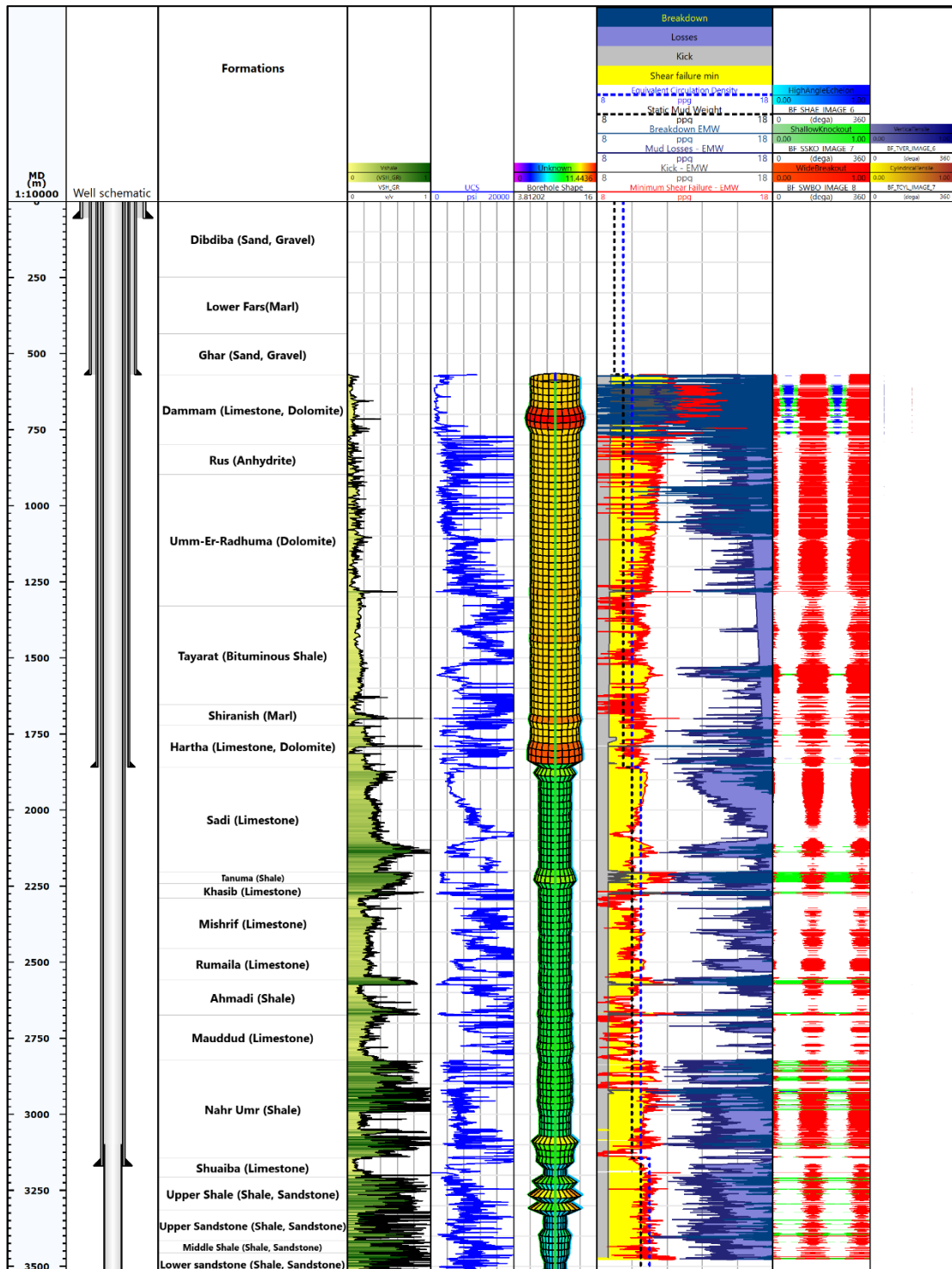


**Figure 4. 14 Wellbore stability analysis with Mohr-Coulomb criterion Published with Techlog 2020.1.1.**

### 4.3.1 Stability analysis with Mohr-Coulomb at Dammam

Dammam formation consists of porous and vuggy dolomite with limestone at the bottom (Master Log, field data). The lithology is extraordinarily weak as clarified by the unconfined compressive strength (UCS), the blue track in Figure 4.15. Mostly, the compressive strength is less than 2000 psi along the interval except the top and bottom parts. Therefore, drilling induced tensile fractures have been predicted due to the weakness of the formation. Interestingly, tensile fracture orientation is 60 deg. and 240 deg., parallel to the maximum horizontal stress orientation.

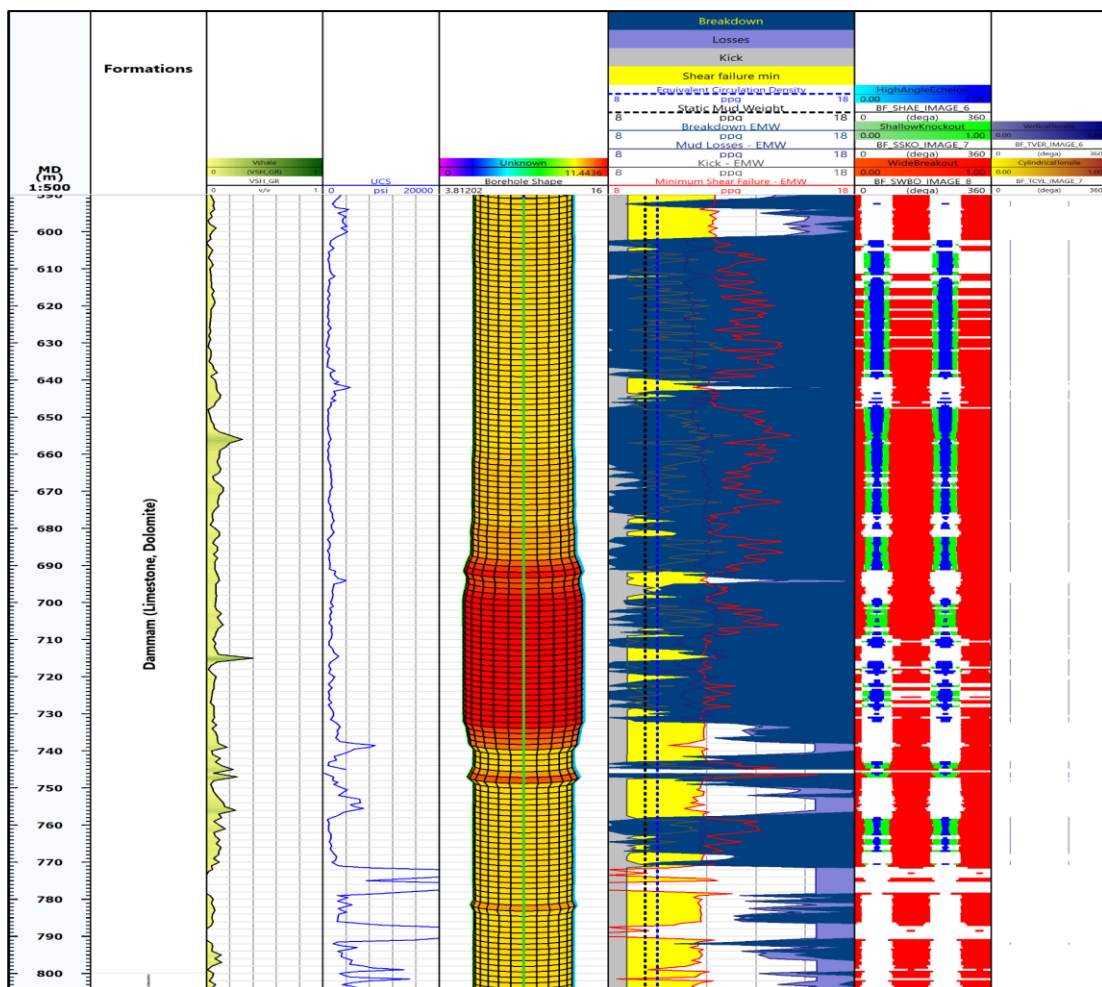


**Figure 4. 15 Wellbore stability analysis with Mohr-Coulomb criterion at Dammam formation, Published with Techlog 2020.1.1.**

By referring to the drilling reports, it was found that a severe to complete mud loss was experienced while drilling. Mud loss was recorded at depth of 785 m TVD. The loss began to subside gradually after 800 m and this is reasonably compatible with the model prediction. On the other hand, high angle echelon shear failure was diagnosed by the model. This phenomenon occurs when the minimum principal stress is the tangential stress (well pressure). Moreover, as the vertical stress is the maximum

principal stress, shear failure will make high-angle fractures covering up to a quarter of the borehole circumference (Pašić 2007). This failure was not revealed by the caliper log, the reason being that the broken rocks in this type of failure may not fall into the wellbore (Abdideh and Alisamir 2018). The only intervals that suffer from high angle echelon shear failure in Zubair field are Dammam and Hartha formations. Importantly, both are porous vuggy dolomite and endure severe to complete mud losses while drilling.

Sensitivity analysis was carried out at 625 m in Dammam formation to assess the mud window. The analysis is dedicated for vertical and deviated wells at any azimuth. Hence, outcomes displayed in Figure 4.16 confirm that the highest required mud weight to avoid break out (Shear failure) is possible in the minimum horizontal stress azimuth with inclination of 65 deg. Similarly, breakdown (Tensile failure) cannot be avoided at elevated mud weight in the direction of minimum horizontal stress with 60 deg. of deviation.

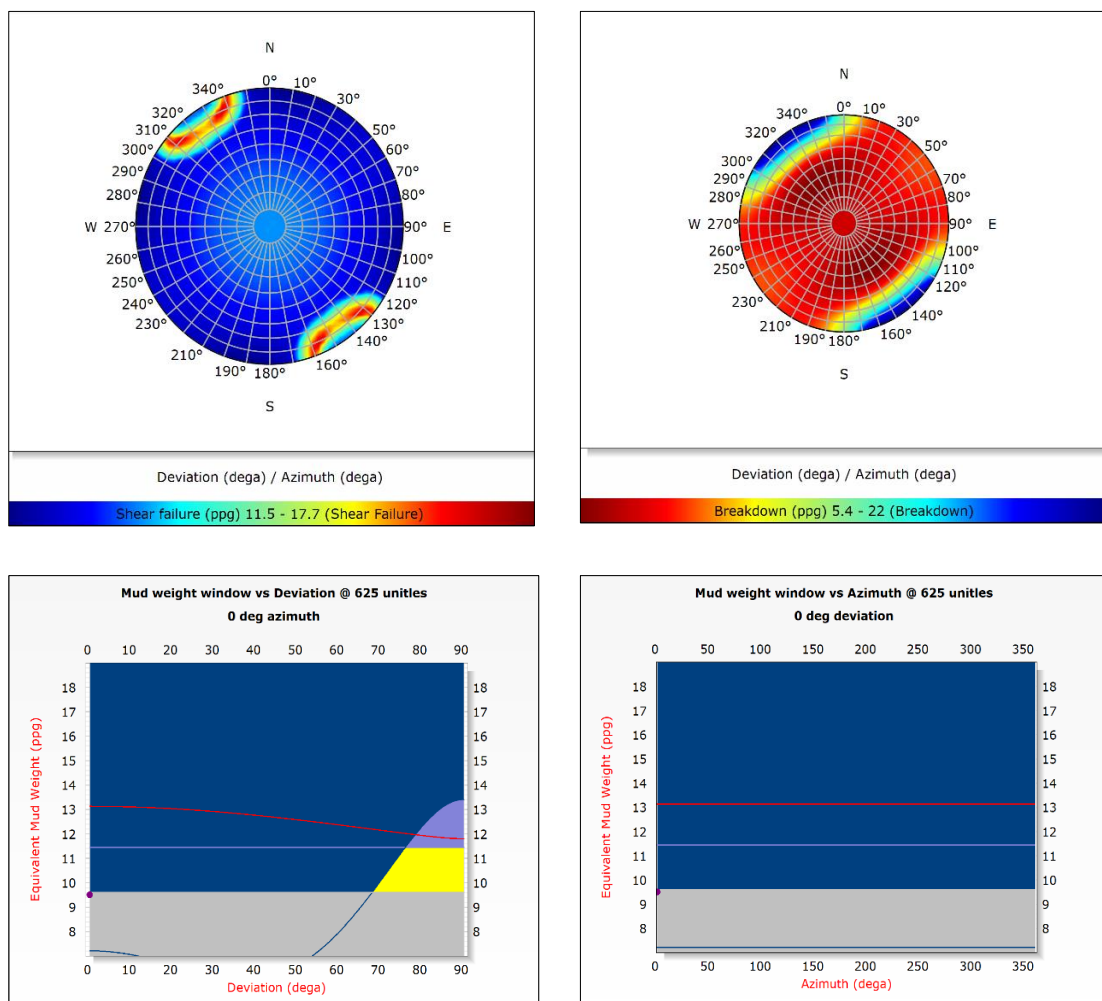


**Figure 4. 16 Sensitivity analysis with Mohr Coulomb criterion at Dammam formation, Published with Techlog 2020.1.1.**

### 4.3.2 Stability analysis with Mohr-Coulomb at Hartha formation

The lithology of Hartha formation is porous and vuggy dolomite with argillaceous limestone (Master Log, field data). The simulation demonstrated quite close results to the caliper log in three depths. The first is 1790 m where the compressive strength (UCS) is too low due to the presence of probable argillaceous limestone as indicated by Gamma ray and master log. The second depth is 1815 m and the third from 1830 to 1845 m TVD, Figure 4.17. Moreover, shallow knockout and high angle echelon shear failures have been figured out at the aforementioned three intervals. To the contrary, breakouts of the other 15 intervals are exaggerated.

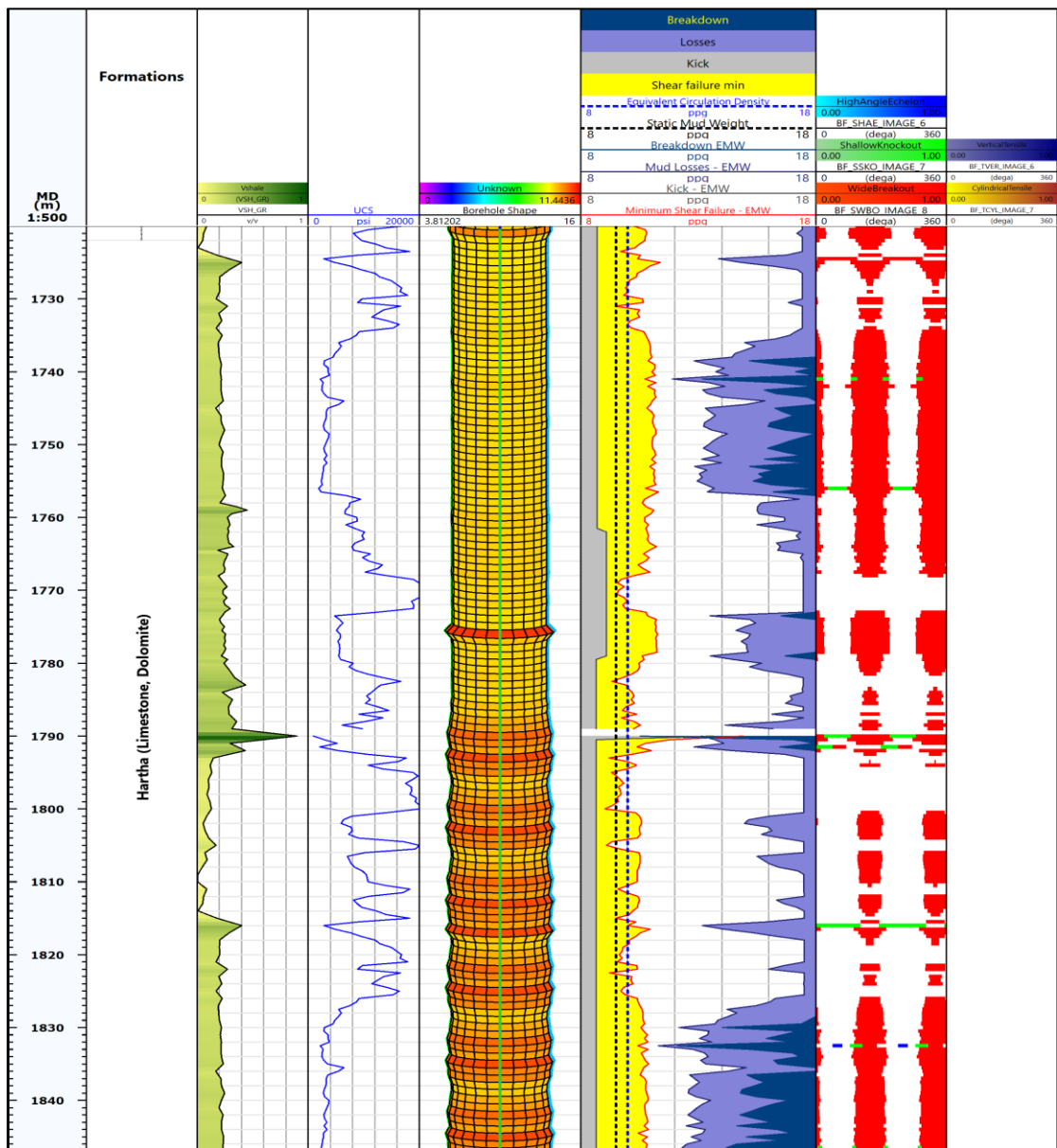
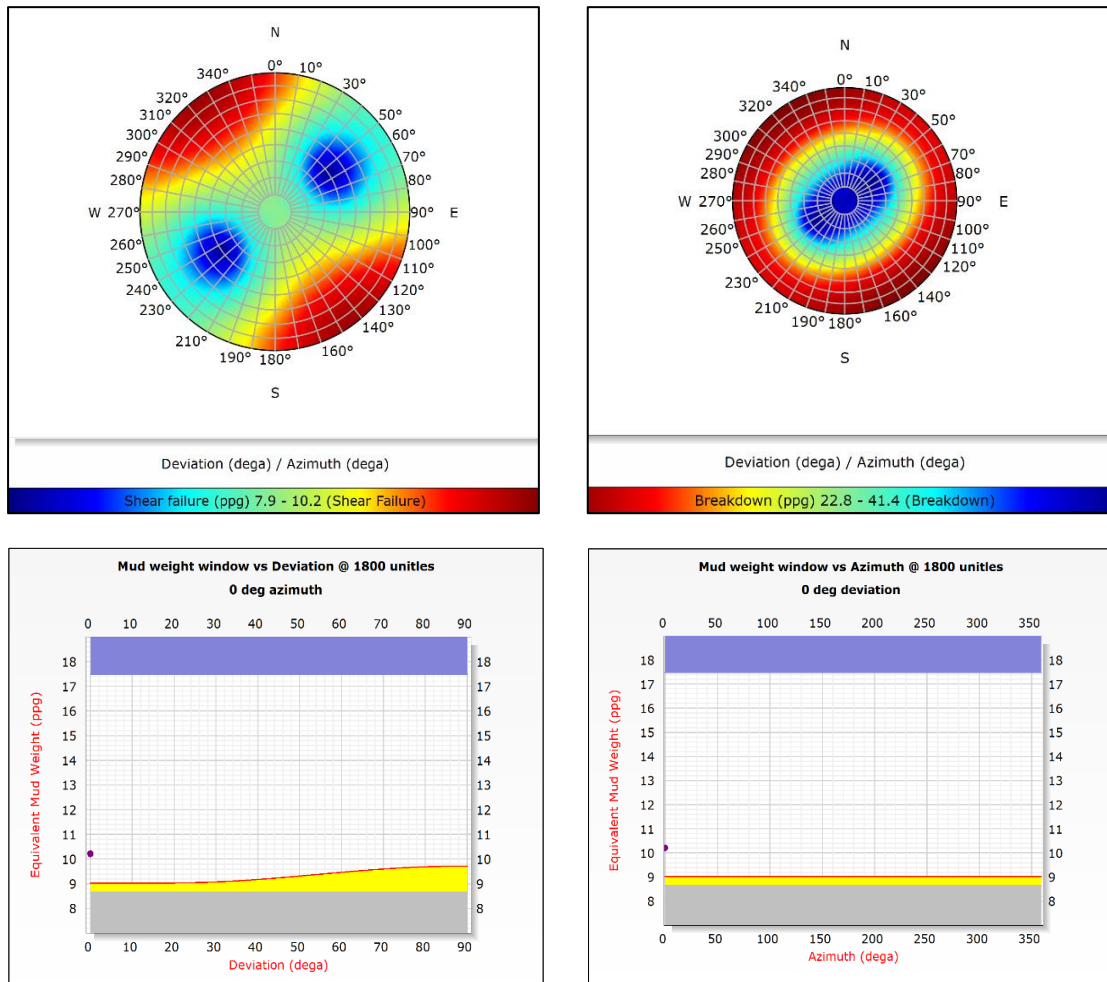


Figure 4. 17 Wellbore stability analysis with Mohr-Coulomb criterion at Hartha formation, Published with Techlog 2020.1.1.

Predominantly, loss in drilling fluids occurs while drilling in Hartha interval. Therefore, daily drilling reports have been revised; it was observed that this section was passed without any loss. It is worth noting that the criterion did not forecast the occurrence of tensile failure, and this may increase the acceptability of the criterion.



**Figure 4. 18 Sensitivity analysis with Mohr-Coulomb criterion at Hartha formation, Published with Techlog 2020.1.1.**

Figure 4.18 represents the sensitivity analysis in Hartha formation at 1800 m. The safest trajectory to be away from borehole collapse is directional drilling with 25-70 deg. in the maximum horizontal direction. Whereas tensile fracture may initiate with inclination higher than 60 deg. in any orientation with lower mud weight. Generally, to avoid both failures the azimuth of maximum horizontal stress is recommended. This proposal is not easy to implement in practice, since this formation of the field is rarely drilled without mud losses. In general, the whole mud window is quite broad and there is good tolerance.

### 4.3.3 Stability analysis with Mohr-Coulomb at Tanuma & Khasib

Tanuma contains grey reactive shale with some beds of porous limestone and pyrite. While Khasib is limestone (chalky and argillaceous) with thin beds of shale (Master Log, field data). Figure 4.19 demonstrates typical matching between predicted breakout and caliper log in most intervals of both formations. Furthermore, shallow knockout is clear in the intervals of low compressive strength (UCS) from 2206 to 2240 m and from 2270 to 2277m.

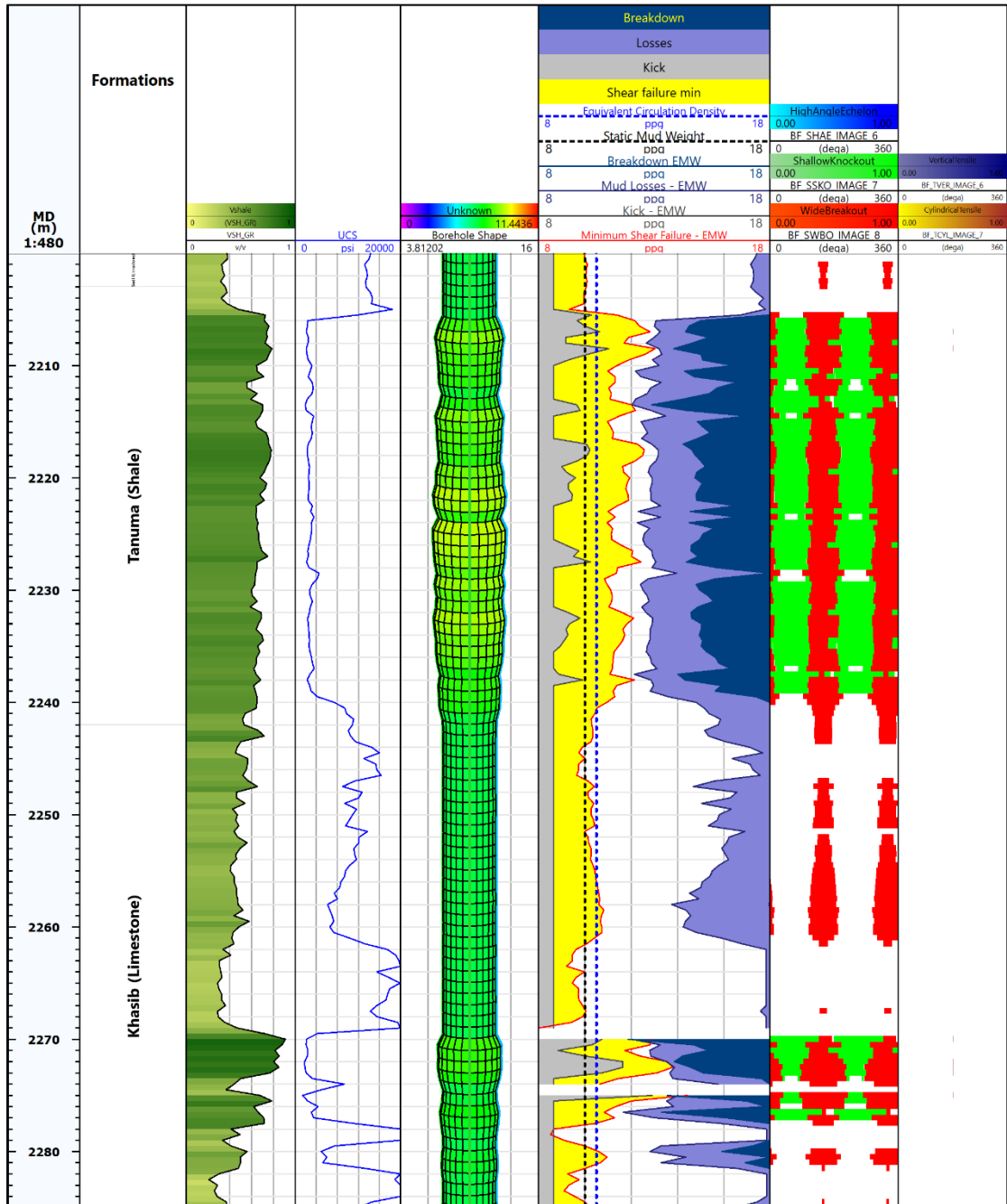
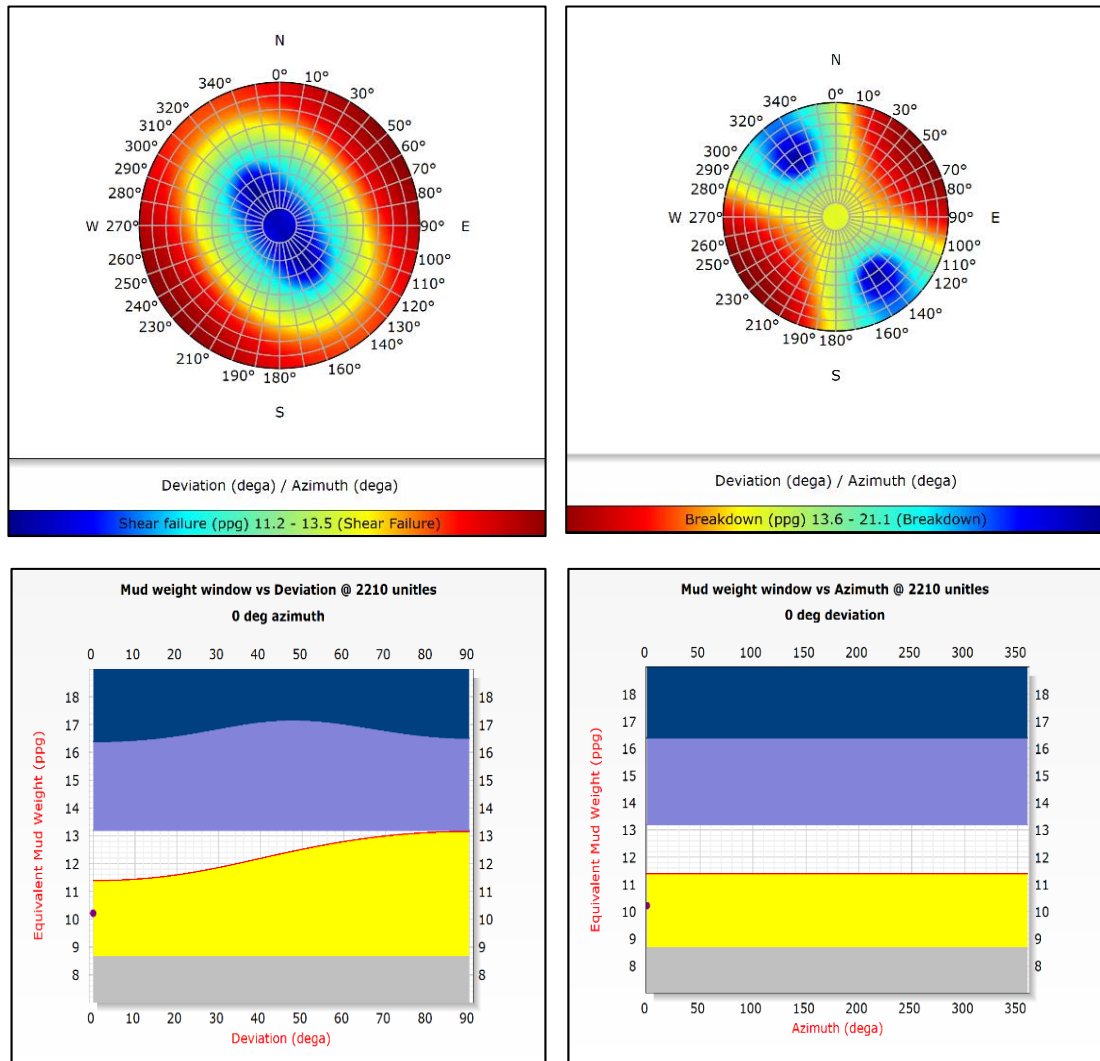


Figure 4. 19 Wellbore stability analysis with Mohr-Coulomb criterion at Tanuma and Khasib formation, Published with Techlog 2020.1.1.

Failure in shallow knockout mode takes place when the axial stress or radial stress is the maximum stress. Hence, failure occurs in the vertical plane parallel to the azimuth of minimum horizontal stress due to the impact of axial and radial stresses (Pašić 2007). As clarified in Figure 4.19, the green zone of shallow knockout is aligned with maximum horizontal stress direction and that confuses the tensile vertical fracture.



**Figure 4. 20 Sensitivity analysis with Mohr-Coulomb criterion at Tanuma and Khasib formations, Published with Techlog 2020.1.1.**

Sensitivity analysis was then fulfilled at 2210 m in Tanuma formation, Figure 4.20. The mud weight window is azimuthal independent, while its value contracts as the deviation increases. Moreover, lower mud weight can be used without hole collapse in vertical or deviated wells with maximum inclination of 40 deg. in the direction of minimum horizontal stress. The same direction requires the highest mud weight in order for tensile fracture to commence.

### 4.3.4 Stability analysis with Mohr-Coulomb at Mishrif formation

The first producer in Zubair field is the upper cretaceous Mishrif carbonate reservoir. The Anderson's fault classification refers to the existence of reverse fault at the top portion, strike slip in the middle and normal fault at the bottom zone (Horizontal stresses prediction, 4.1.8). The lithology is porous detrital limestone (Master Log, field data). In addition, the reservoir has been producing for more than 50 years, so there is desperate depletion. All these preceding aspects encourage the deepest investigation in wellbore stability.

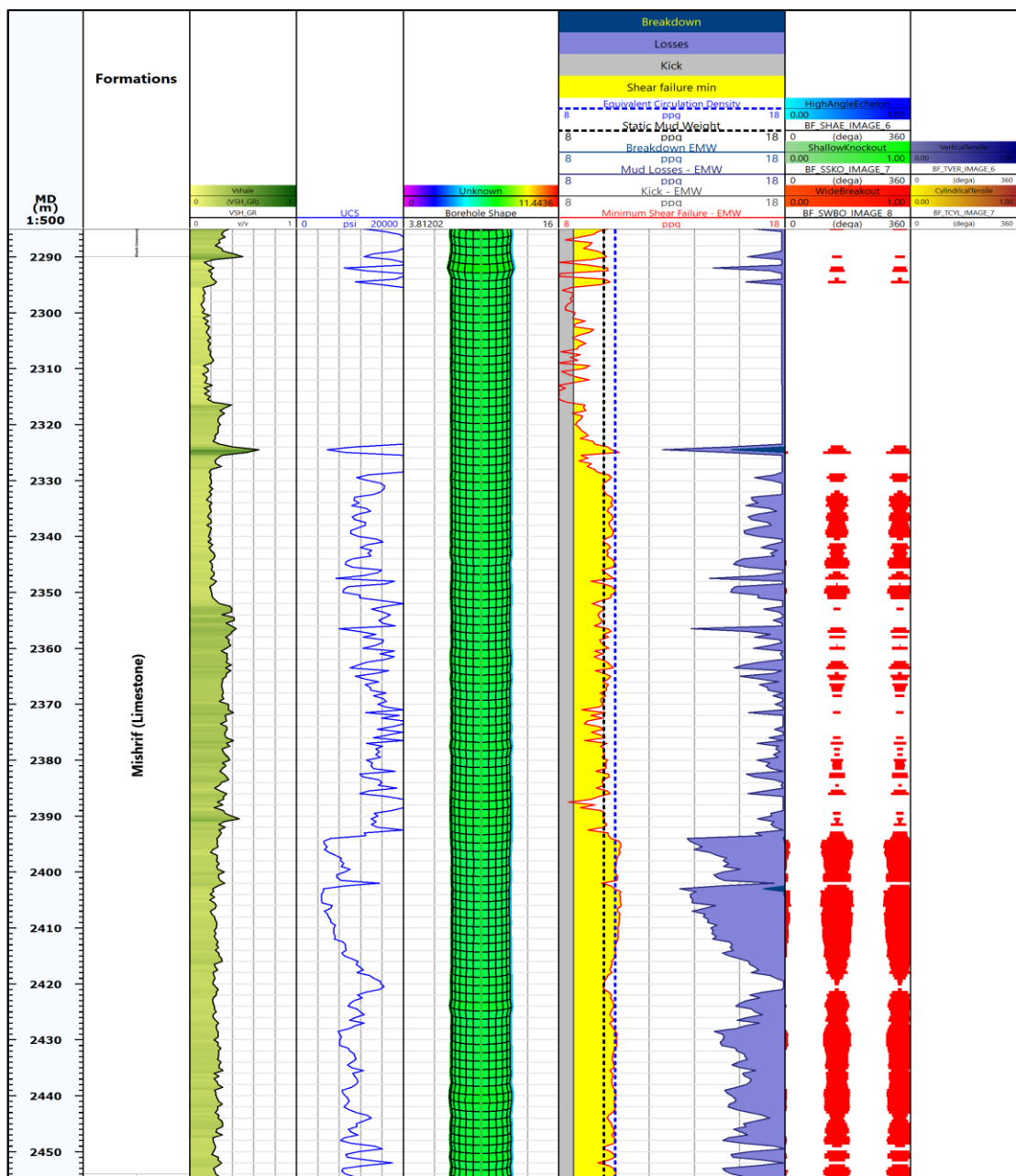
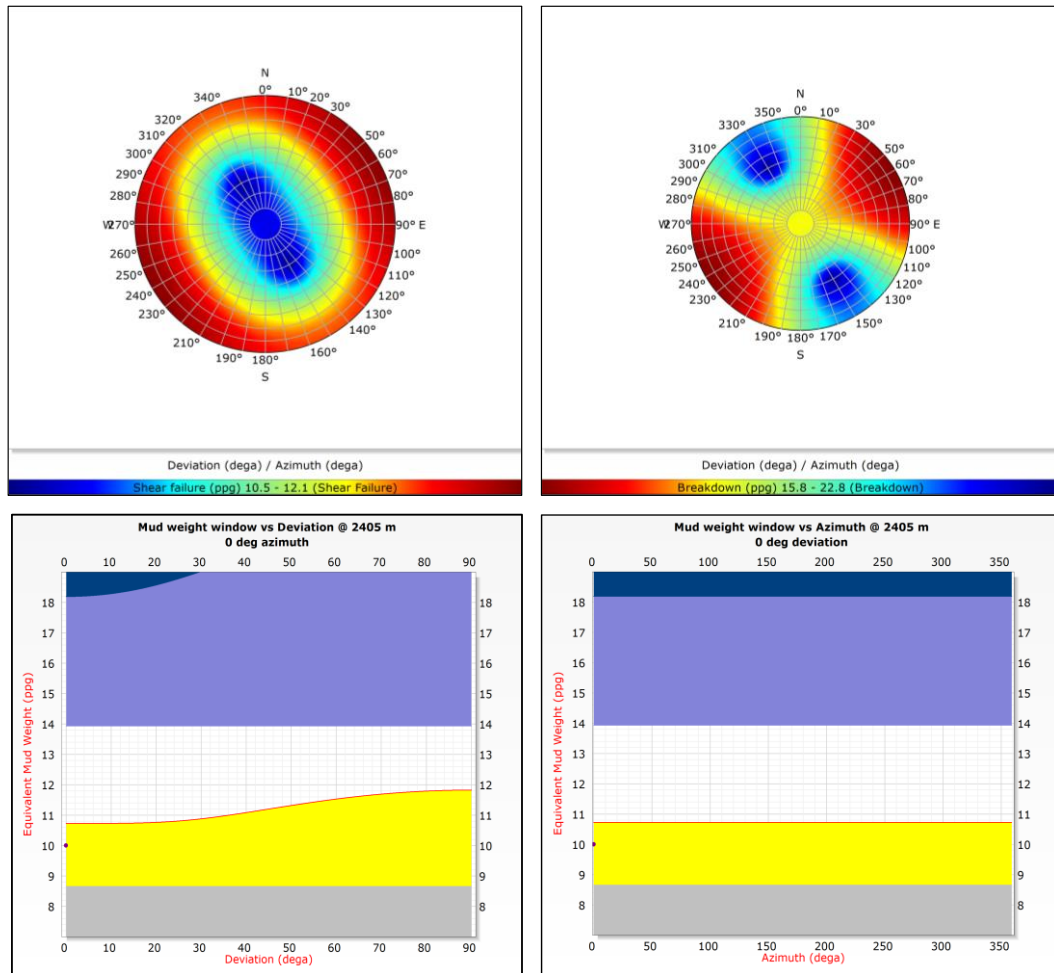


Figure 4. 21 Wellbore stability analysis with Mohr-Coulomb criterion at Mishrif formation, Published with Techlog 2020.1.1.

The foreseen breakout is overrated compared with the caliper log in some portions. Mohr-Coulomb criterion has not anticipated the drilling induced tensile fracture despite the probabilistic mud loss in the depleted reservoir. Therefore, the daily drilling reports were reviewed, no mud loss was recorded while drilling.



**Figure 4. 22 Sensitivity analysis with Mohr-Coulomb criterion at Mishrif formations, Published with Techlog 2020.1.1.**

The mud window versus deviation starts to shrink after 20 deg. of inclination whereas it remains constant with respect to the hole direction. The least desired mud weight to stay away from the shear failure is reachable at vertical to 40 deg. of inclination, parallel to the minimum horizontal stress. On the other side, the breakdown is expected in the horizontal stress azimuth with inclination of 40-90 deg. at the highest proposed mud weight, 22.8 ppg. Generally, the azimuth of  $\sigma_h$  is the optimal trajectory to minimize the risk of shear and tensile failures.

### 4.3.5 Stability analysis with Mohr-Coulomb at Nahr Umr

One of the most mechanically and chemically stressed lithologies in the field is Nahr Umr formation. It is black fissile shale with siltstone, limestone and intercalated fine sandstone. Tectonically, the formation is normally faulted.

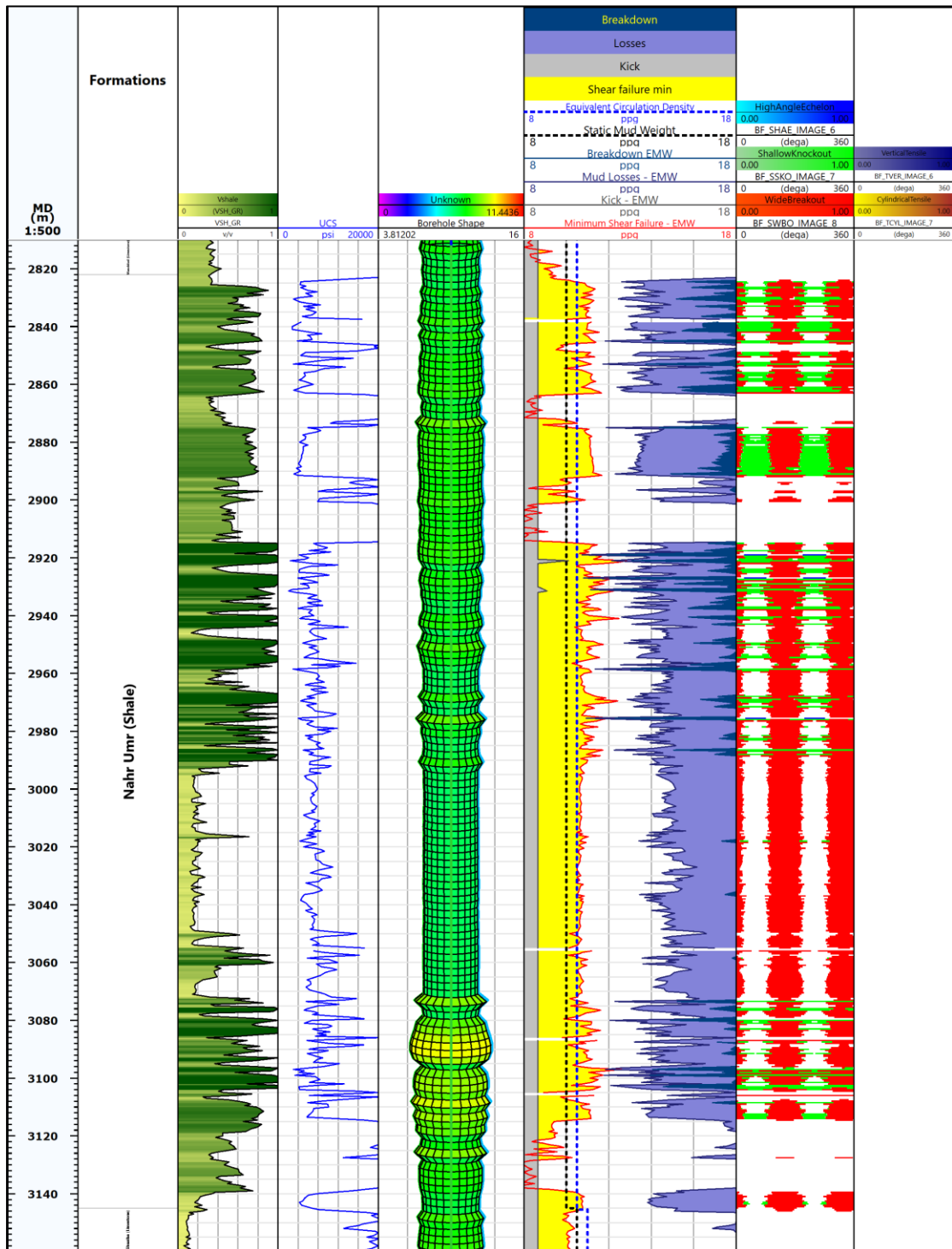
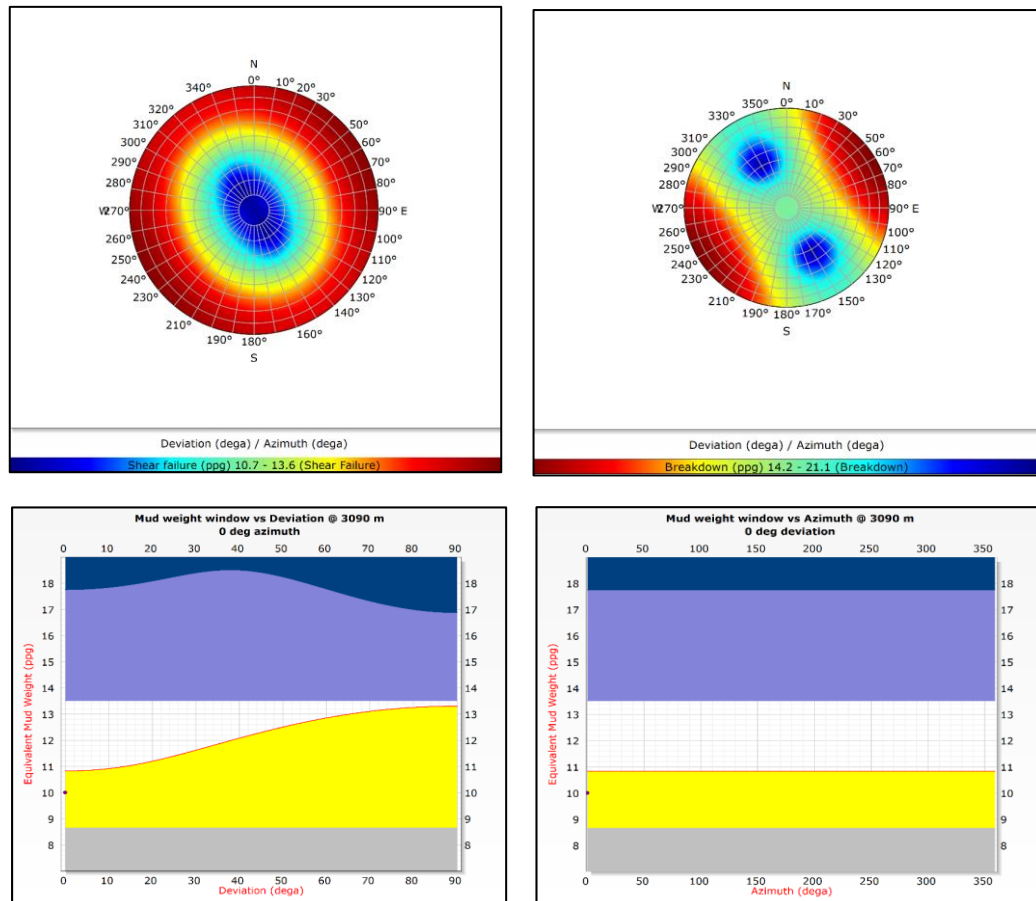


Figure 4. 23 Wellbore stability analysis with Mohr-Coulomb criterion at Nahr Umr formation , Published with Techlog 2020.1.1.

Gamma Ray in the third track, UCS in the fourth track and mud logging report of ZB-233 were investigated to ensure that the criterion was properly working. All these data were concordant that the formation from 2860 to 2870 m and from 2890 to 2910 m is compacted limestone. Therefore, no shear failure was predicted by model or indicated by calipers. Furthermore, shallow knockout and wide breakout were determined on the other intervals with good agreement between prediction and calipers. Other than that, Mohr-Coulomb overestimated shear failure in the sandstone interval from 2995-3070 m.



**Figure 4. 24 Sensitivity analysis with Mohr-Coulomb criterion at Nahr Umr formations, Published with Techlog 2020.1.1.**

Shear failure can be avoided with minimum allowable mud weight in vertical or deviated wells with maximum inclination of 35 deg. parallel to the minimum horizontal stress. While the formation can afford the highest permitted mud weight in the direction of  $\sigma_h$  with deviation of 25-70 deg., Figure 4.24. The other aspect in the mud window is that the clearance decreases gradually after 10 deg. of inclination until it approaches the lower value at 85 deg. Consequently, the azimuth of minimum horizontal stress is still the preferred wellbore trajectory.

### 4.3.6 Stability analysis with Mohr-Coulomb at Zubair formation

Zubair formation has 5 constituent members: Upper shale, Upper sandstone, Middle shale, Lower sandstone and Lower shale. Upper and middle shale are fissile black shale with layers of siltstone and sandstone. While upper and lower sandstone contain sandstone interbedded with shale and siltstone. Eventually, lower shale is entirely fissile black shale with siltstone (Master Log,). This assortment of rocks with fluctuated UCS complicates the well conditions geomechanically, Figure 4.25.

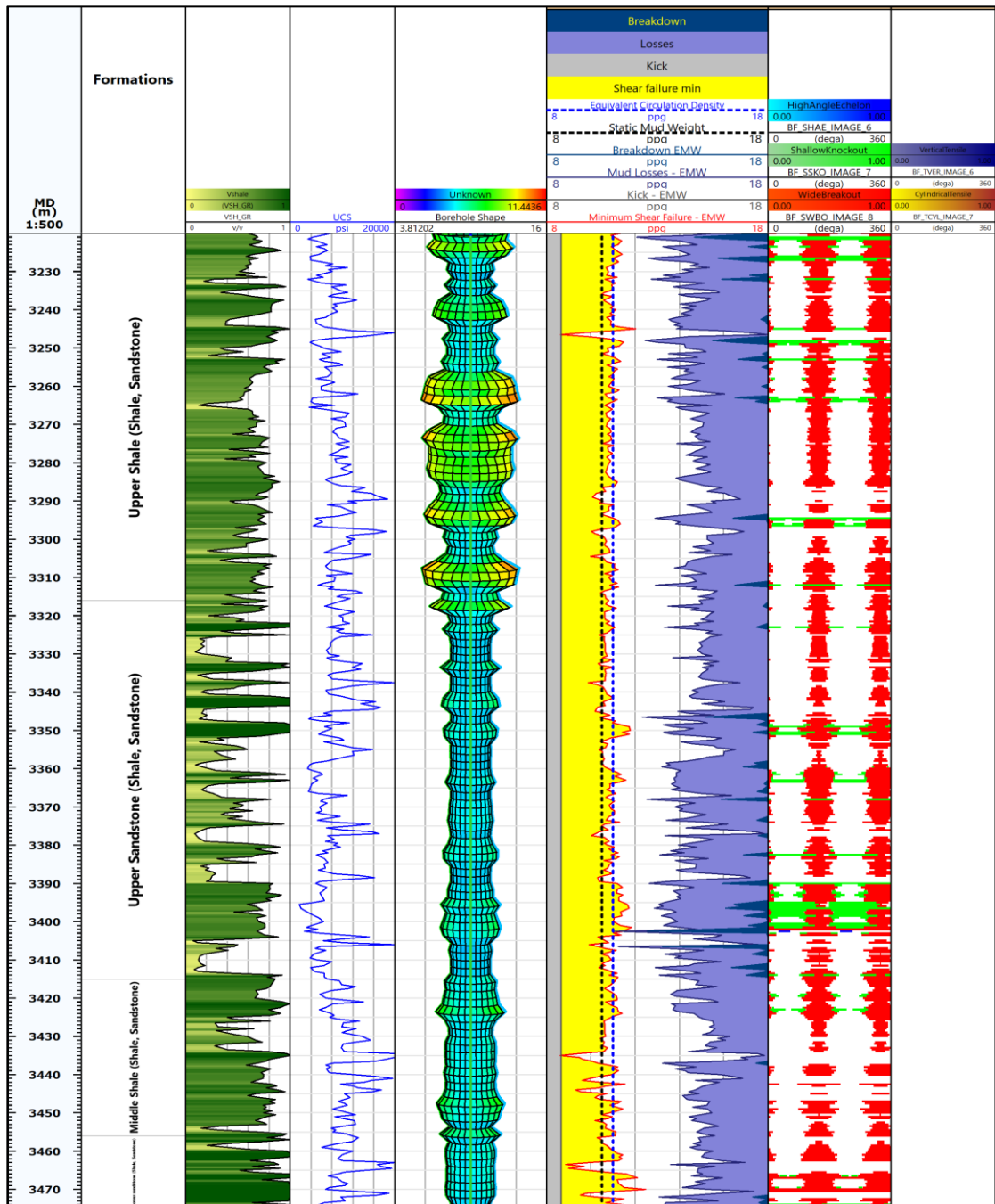
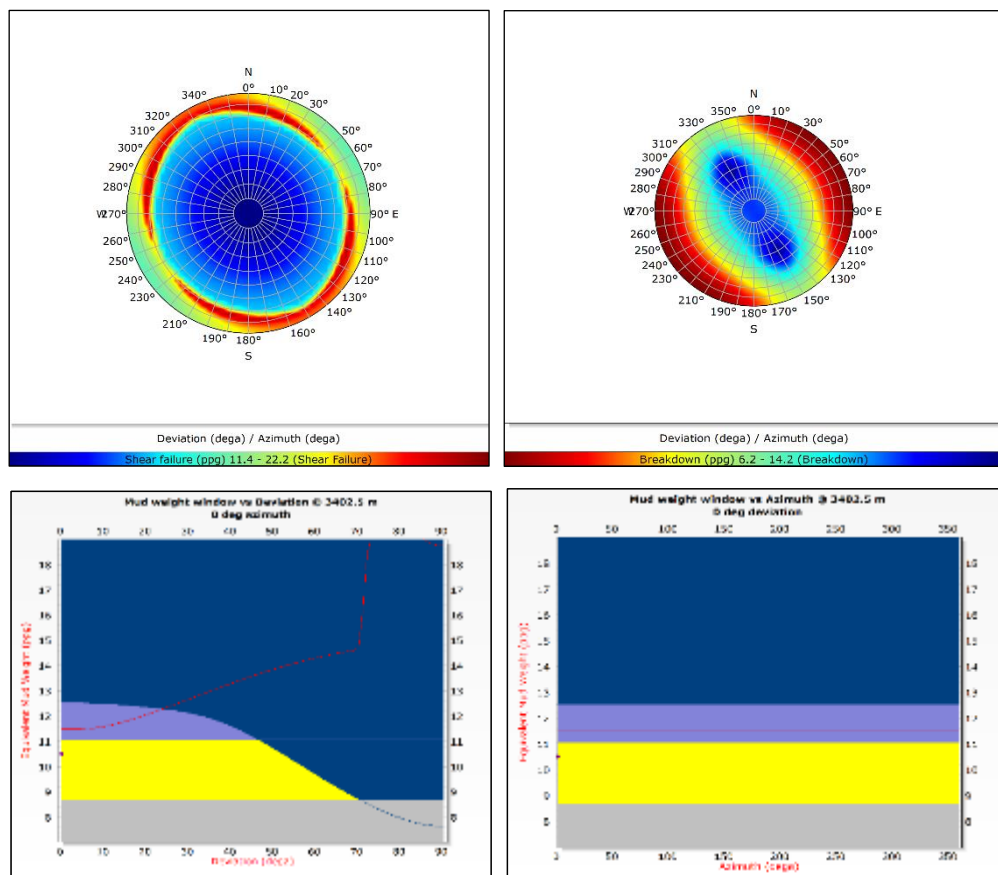


Figure 4. 25 Wellbore stability analysis with Mohr-Coulomb criterion at Zubair members formation, Published with Techlog 2020.1.1.

There is adequate consistency between predicted and real shear failures in the upper shale portion. Most of the shallow knockout on caliper log was anticipated by the criterion, Figure 4.25. Likewise, the upper sandstone is characterized by higher percentage of sandstone, so there is breakout in shale and siltstone layers according to model which is approved by the caliper. Additionally, the shallow knockout from 3390 to 3403 m was expected by the model and detected by caliper log. The same resemblances in the remaining intervals have been diagnosed and with acceptable agreement between what was prospected and recorded.

Figure 4.26 describes the sensitivity analysis of the upper sandstone member at 3402.5 m. In this depth there is high angle echelon shear failure, and no mud density is adequate to avoid all kinds of failures. Upper sandstone is the pay zone and there are some depleted intervals which worsen the situation. To avoid shear failure, vertical and deviated well with maximum 80 deg. of inclination in horizontal stress direction is recommended.



**Figure 4. 26 Sensitivity analysis with Mohr-Coulomb criterion at Zubair members formations, Published with Techlog 2020.1.1.**

## 4.4 Wellbore stability analysis with Mogi-Coulomb criterion

The Mogi-Coulomb criterion has been adopted to realize the wellbore stability analysis in Zubair field after the implementation of Mohr-Coulomb. Mogi is the most applicable failure criterion for sedimentary rocks. According to this model, the leverage of intermediate principal stress cannot be neglected, particularly in high anisotropic in-situ stresses. Moreover, the criterion is feasible at all the stress states (Al-Ajmi and Zimmerman 2006), (Islam et al. 2010). The next pages will decide the feasibility of this model in the field. The subsequent demonstration was utilized to derive the final equations to be used in this thesis to construct the MEM (Gholami et al. 2014).

$$A = 3\sigma_h - \sigma_H \quad (4.27)$$

$$B = \sigma_v - 2\nu(\sigma_H - \sigma_h) \quad (4.28)$$

$$D = 3\sigma_H - \sigma_h \quad (4.29)$$

$$E = \sigma_v + 2\nu(\sigma_H - \sigma_h) \quad (4.30)$$

$$N = \tan^2\left(\frac{\pi}{4} + \frac{\varphi'}{2}\right) \quad (4.31)$$

$$a' = 2C\cos\varphi' \quad (4.32)$$

$$b' = \sin\varphi' \quad (4.33)$$

**Table 4. 3 Shear failure equations in vertical well based on Mogi-Coulomb.**

Borehole Stresses	Shear Failure Mogi-Coulomb
$\sigma'_z \geq \sigma'_\theta \geq \sigma'_r$	$P_{w(BO)} = \frac{1}{6 - 2b'^2} \left[ (3D + 2b'K) + \sqrt{H + 12(K^2 + b'DK)} \right]$
$\sigma'_\theta \geq \sigma'_z \geq \sigma'_r$	$P_{w(BO)} = \frac{1}{2}D - \frac{1}{6}\sqrt{12(a' + b'D)^2 - 3(D - 2E)^2}$
$\sigma'_\theta \geq \sigma'_r \geq \sigma'_z$	$P_{w(BO)} = \frac{1}{6 - 2b'^2} \left[ (3D - 2b'G) + \sqrt{H + 12(G^2 - b'DG)} \right]$
$H = D^2(4b'^2 - 3) + (E^2 - DE)(4b'^2 - 12), \quad K = a' + b'E, \quad G = K + b'D$	

**Table 4. 4 Tensile failure equations in vertical well based on Mogi-Coulomb.**

Borehole Stresses	Tensile Failure Mogi-Coulomb
$\sigma'_r \geq \sigma'_\theta \geq \sigma'_z$	$P_{w(Frac)} = \frac{1}{6 - 2b'^2} \left[ (3A + 2b'N) + \sqrt{J + 12(N^2 + b'AN)} \right]$
$\sigma'_r \geq \sigma'_z \geq \sigma'_\theta$	$P_{w(Frac)} = \frac{1}{2}A + \frac{1}{6}\sqrt{12(a' + b'A)^2 - 3(2AB)^2}$
$\sigma'_z \geq \sigma'_r \geq \sigma'_\theta$	$P_{w(Frac)} = \frac{1}{6 - 2b'^2} \left[ (3A + 2b'M) + \sqrt{J + 12(M^2 - b'AM)} \right]$
$J = D^2(4b'^2 - 3) + (E^2 - DE)(4b'^2 - 12), \quad M = N + b'D, \quad N = a' + b'(E - 2Po)$	

The right side tracks in Figure 4.27 clarify the wellbore stability modeling with Mogi-Coulomb, against the Mohr-Coulomb on the left tracks. The Mohr-Coulomb criterion underestimated the rock strength parameters, therefore the failure assessment in the field was overstated due to the ignorance of  $\sigma_2$  effect. To the contrary, criteria that consider the influence of intermediate principal stress on formation strength, such as Mogi and Modified Lade, may indicate the best similarity with reference to the borehole shape.

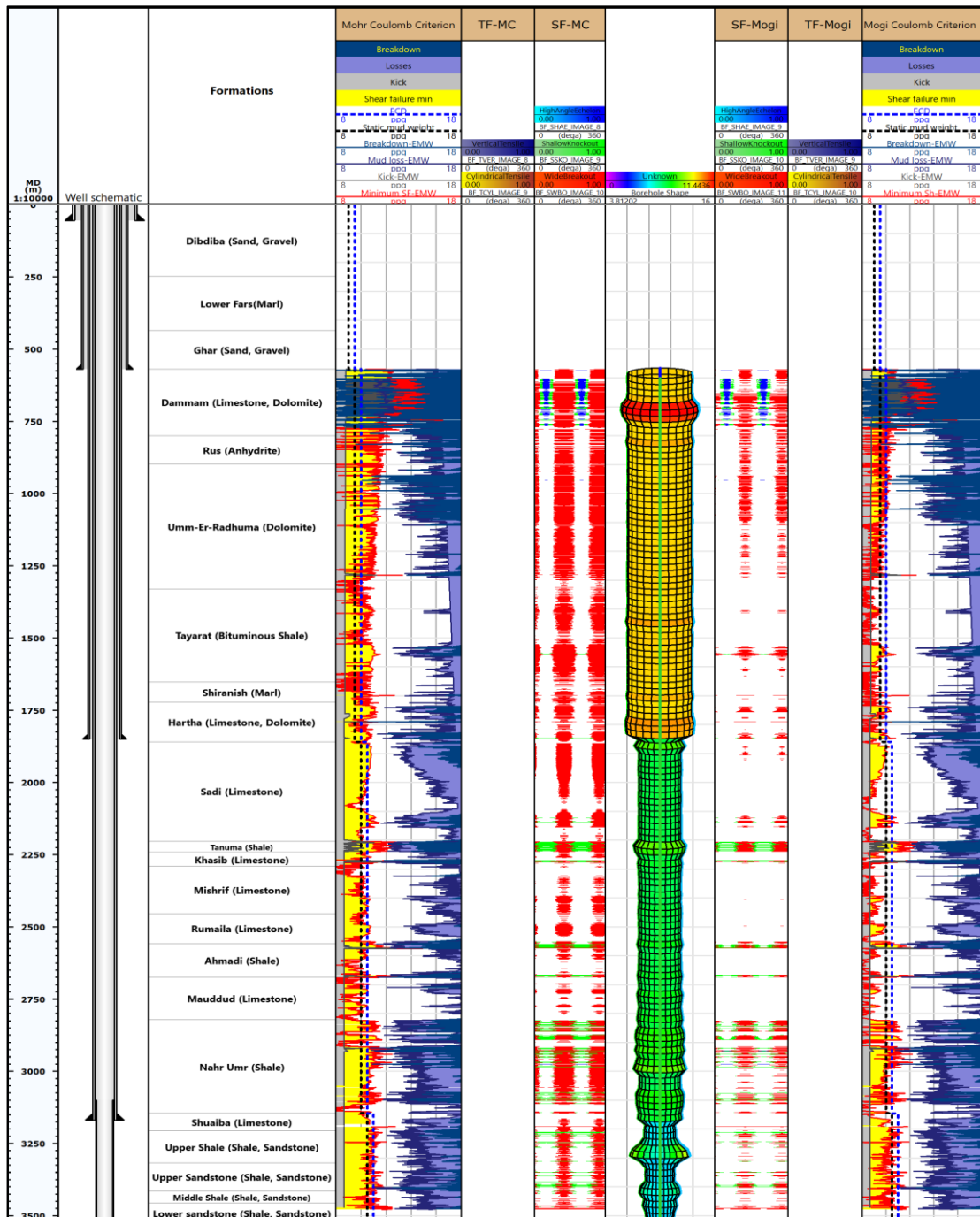


Figure 4. 27 Wellbore stability analysis with Mogi-Coulomb criterion versus Mohr Coulomb criterion, Published with Techlog 2020.1.1.

Mogi and Modified Lade were implemented and the results were nearly consistent. The three-dimensional Mogi-Coulomb criterion was selected for comparison purposes with the two-dimensional Mohr Coulomb criterion. Mogi is more applicable globally than Modified Lade, therefore it was adopted.

#### 4.4.1 Stability analysis with Mogi versus Mohr at Dammam

There was no difference between the two models in determining the high angle echelon shear failure, Figure 4.28. The tensile failure was diagnosed by both criteria and this is compatible with the well record, where mud loss was experienced while drilling as summarized in the Dammam Mohr section.

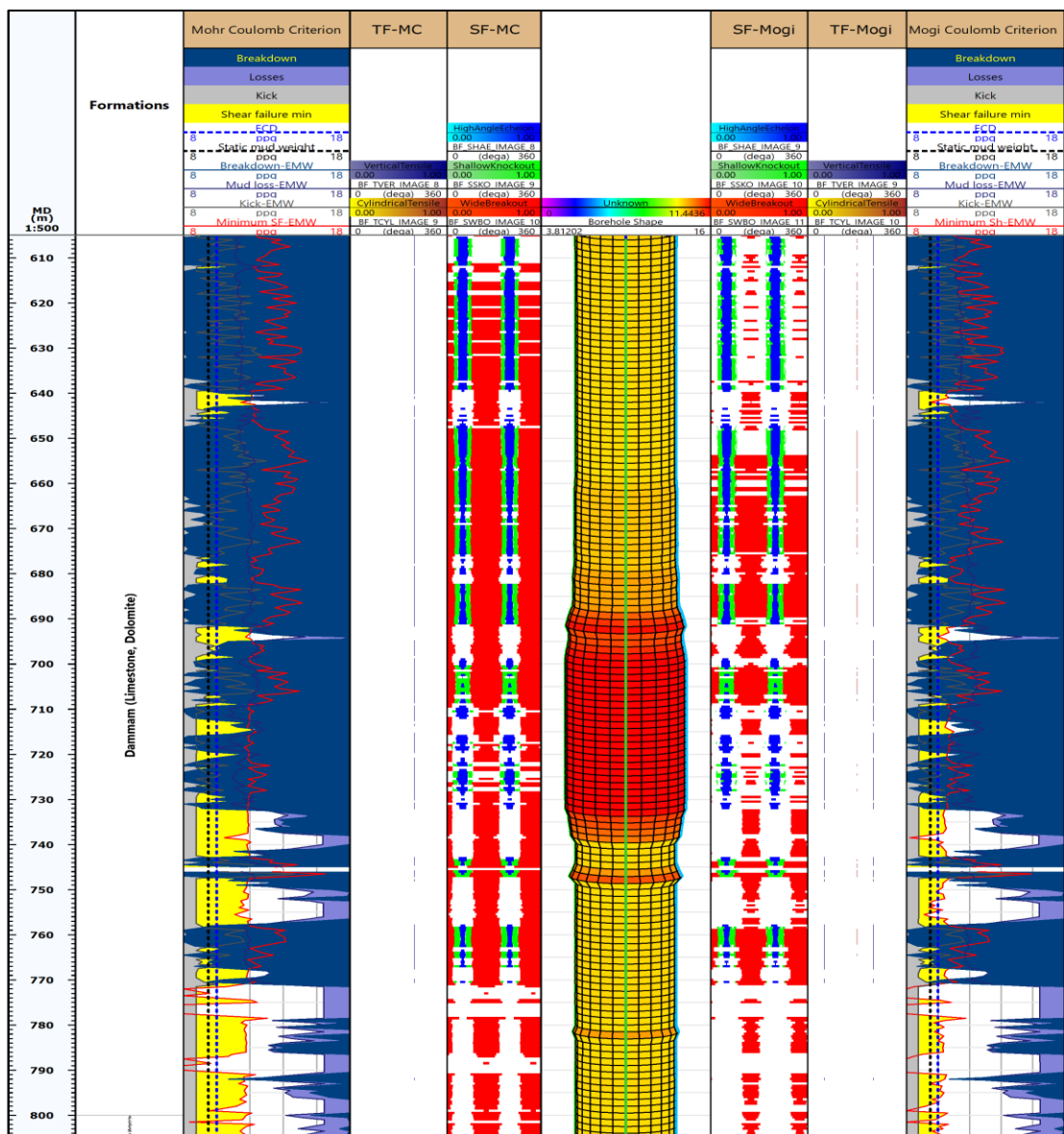
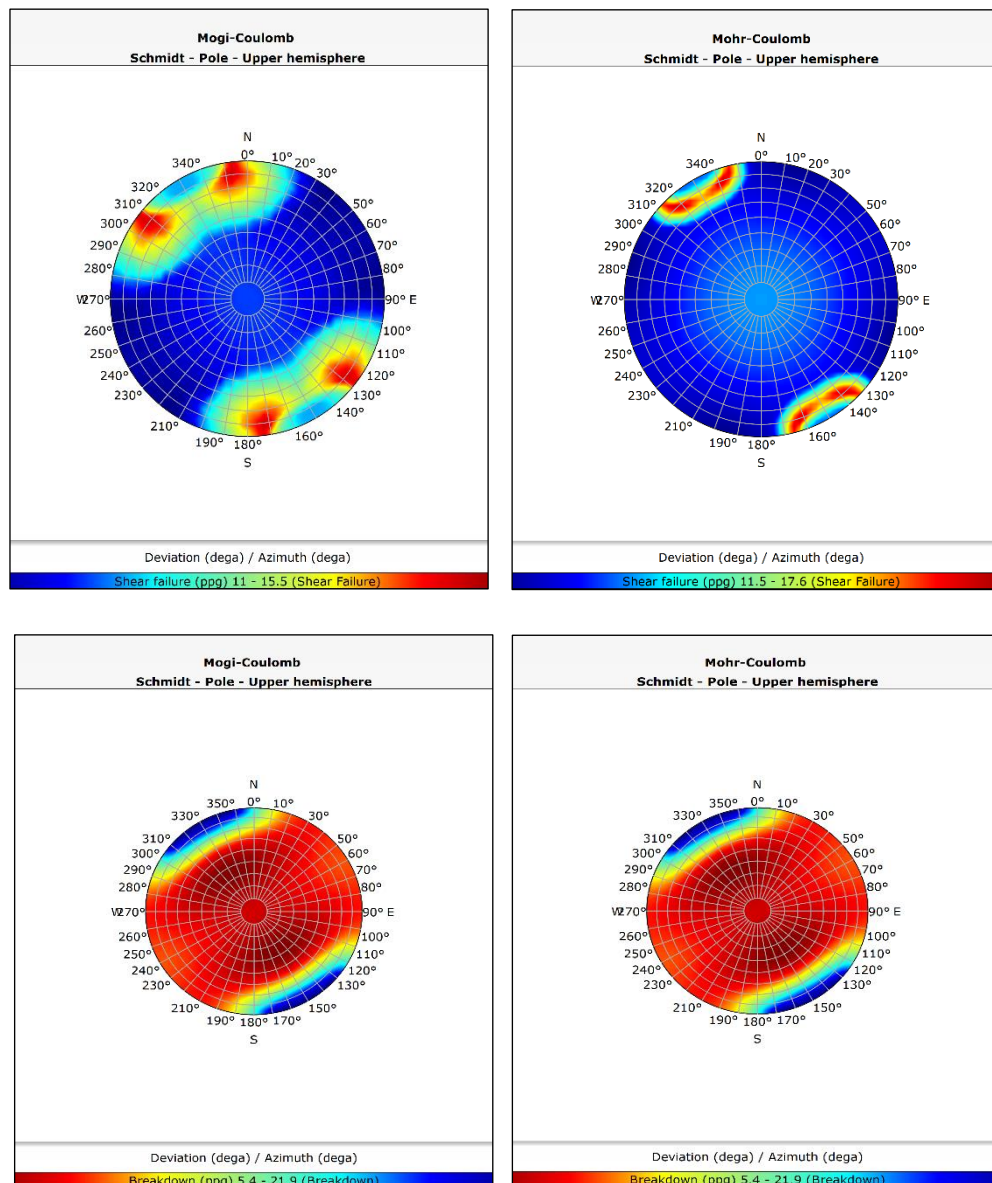


Figure 4. 28 Wellbore stability analysis with Mogi-Coulomb versus Mohr Coulomb criterion in Dammam formation, Published with Techlog 2020.1.1.

Additionally, Mogi agreed with Mohr in shallow knockout forecasting at most intervals. Other than that, there is considerable variation between the two criteria in detecting the common shear failure “Wide breakout”. Mohr exaggerated this kind of shear failure in the overall formation compared to the Mogi and caliper.



**Figure 4.29 Sensitivity analysis with Mogi-Coulomb versus Mohr Coulomb criterion in Dammam formation, Published with Techlog 2020.1.1.**

The sensitivity analysis displays distinction between the two models. Breakdown stereonets are totally compatible in both criteria. Whereas shear failure can be bypassed with lower drilling fluid density in Mogi as opposed to Mohr-Coulomb. To avoid shear in the deviated well, according to Mogi, mud weight should be elevated after 45 deg. of inclination in the  $\sigma_h$  direction. While mud density must be raised after 60 deg. in the same direction, according to Mohr, Figure 4.29.



The sensitivity analysis was carried out at 1790 m. This spot is the most sensitive along Hartha formation according to the stability analysis by both criteria, Figure 4.30. However, the breakdown versus deviation/azimuth demonstrated resemblance between Mogi and Mohr-Coulomb models. On the other hand, the stereonet plot of Mogi coulomb demonstrates that from the vertical to highly deviated well, with inclination of 70 deg. the required mud weight to avoid shear failure in all directions is the same. This is quite unlike the Mohr-Coulomb behavior because the mud weight that is desired to avert the breakdown is azimuthal dependent after 50 deg. of deviation.

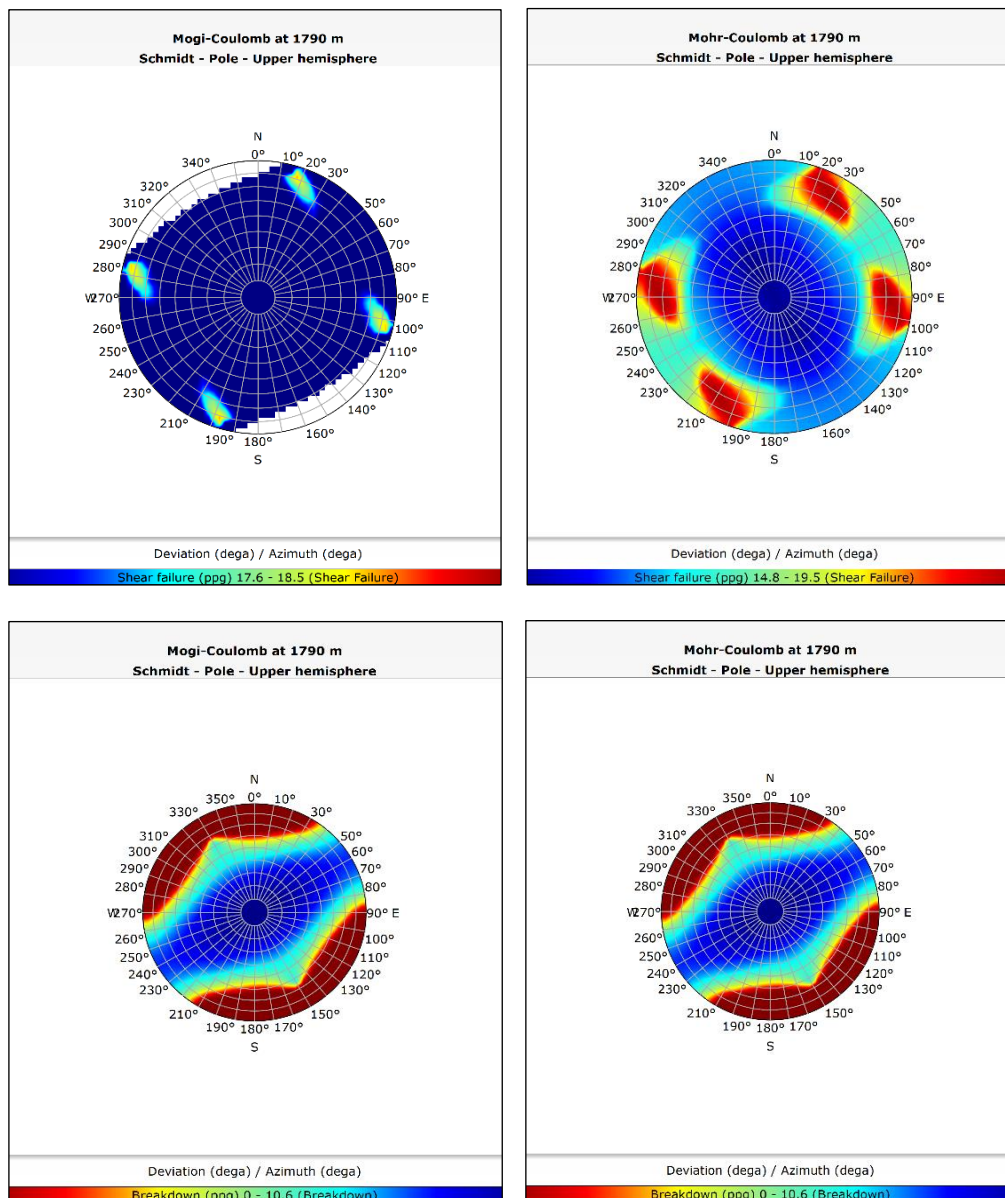


**Figure 4. 31 Sensitivity analysis with Mogi-Coulomb versus Mohr Coulomb criterion at Hartha formation, Published with Techlog 2020.1.1.**

### 4.4.3 Stability analysis with Mogi versus Mohr at Tanuma and Khasib Formations

Notable identification was verified in both Mogi and Mohr between predicted failures, whether wide breakout or shallow knockout, and borehole profile at Tanuma formation. Similarly, in Khasib zone from 2270 m to 2282m. In addition, Caliper log and Mogi are perfectly in agreement regarding the absence of breakout from 2240 to 2262 m, unlike Mohr which overvalued the failure existence.

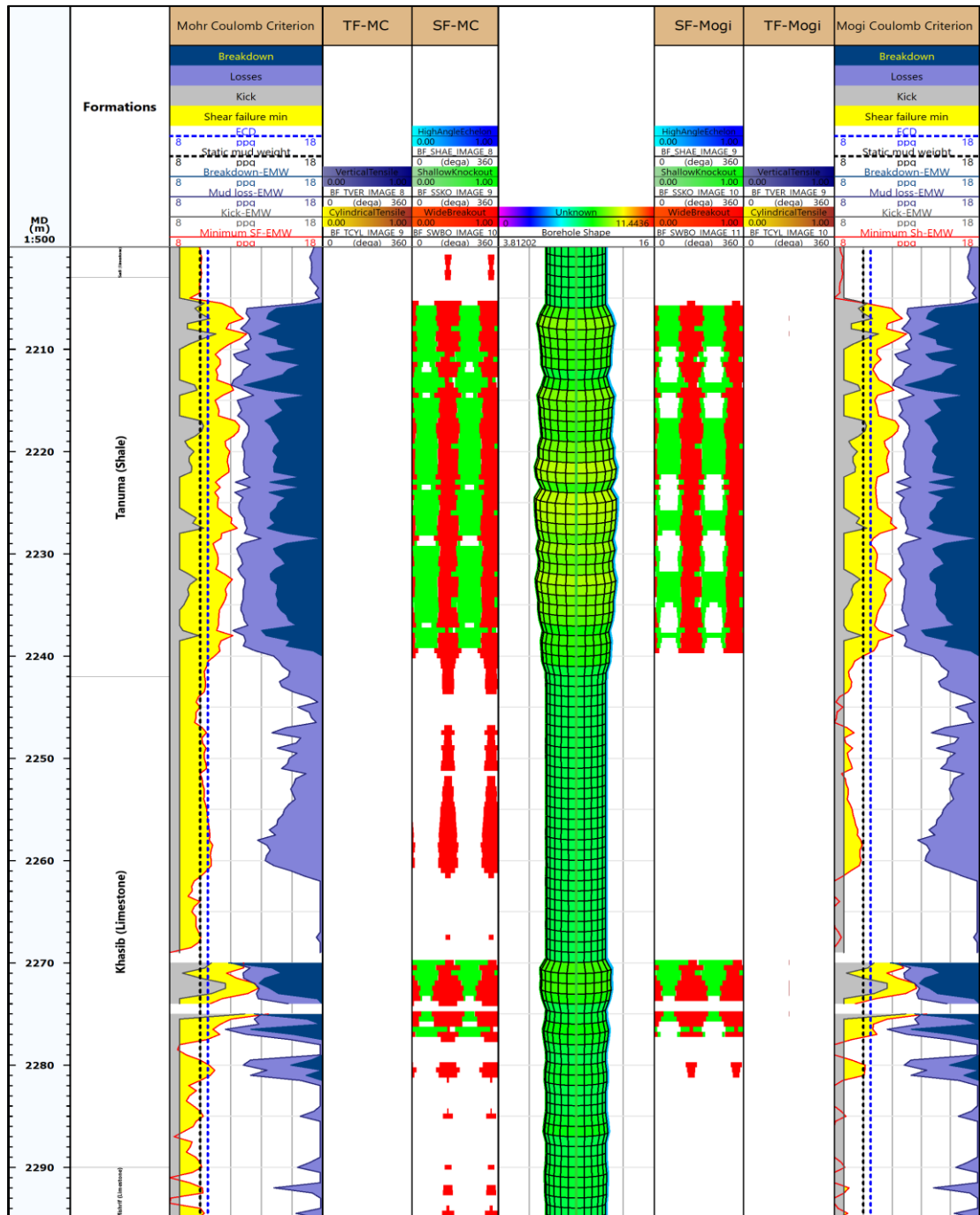
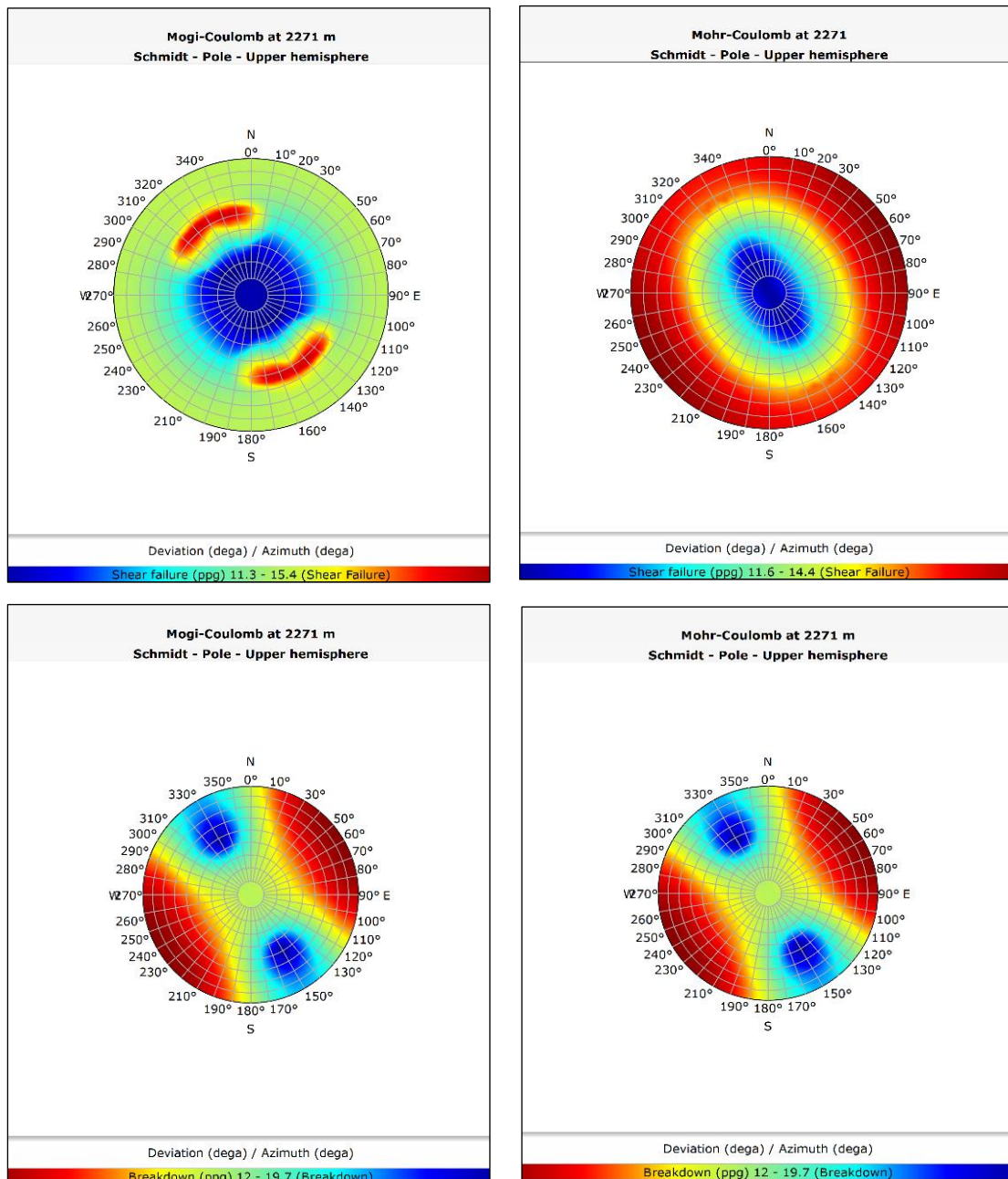


Figure 4. 32 Wellbore stability analysis with Mogi-Coulomb versus Mohr Coulomb in Tanuma and Khasib formation, Published with Techlog 2020.1.1.

Once again, the two models were identical in tensile failure estimation concerning the borehole inclination and azimuth, Figure 4.33. On the other side, the upper hemisphere of shear failure according to Mogi criterion is roughly dissimilar from Mohr. Hence, in the azimuth of minimum horizontal stress with inclination of 45- 60 deg., the mud weight is the highest to drill safely without shear failure. Whereas 60 deg. of deviation and higher parallel to  $\sigma_h$  desires elevated mud weight according to the Mohr criterion.



**Figure 4. 33 Sensitivity analysis with Mogi-Coulomb versus Mohr Coulomb criterion at Tanuma and Khasib formation, Published with Techlog 2020.1.1.**

#### 4.4.4 Stability analysis with Mogi versus Mohr at Mishrif

The lithology of Mishrif formation was described in the section on stability analysis with Mohr-Coulomb criterion. Hence, the compressive strength of this rock is rather high, Figure 4.18. Therefore, the borehole shape is in gauge with intangible enlargement in some intervals. This is concordant with the Mogi prediction, whereas Mohr-Coulomb amplified the failure prognosis.

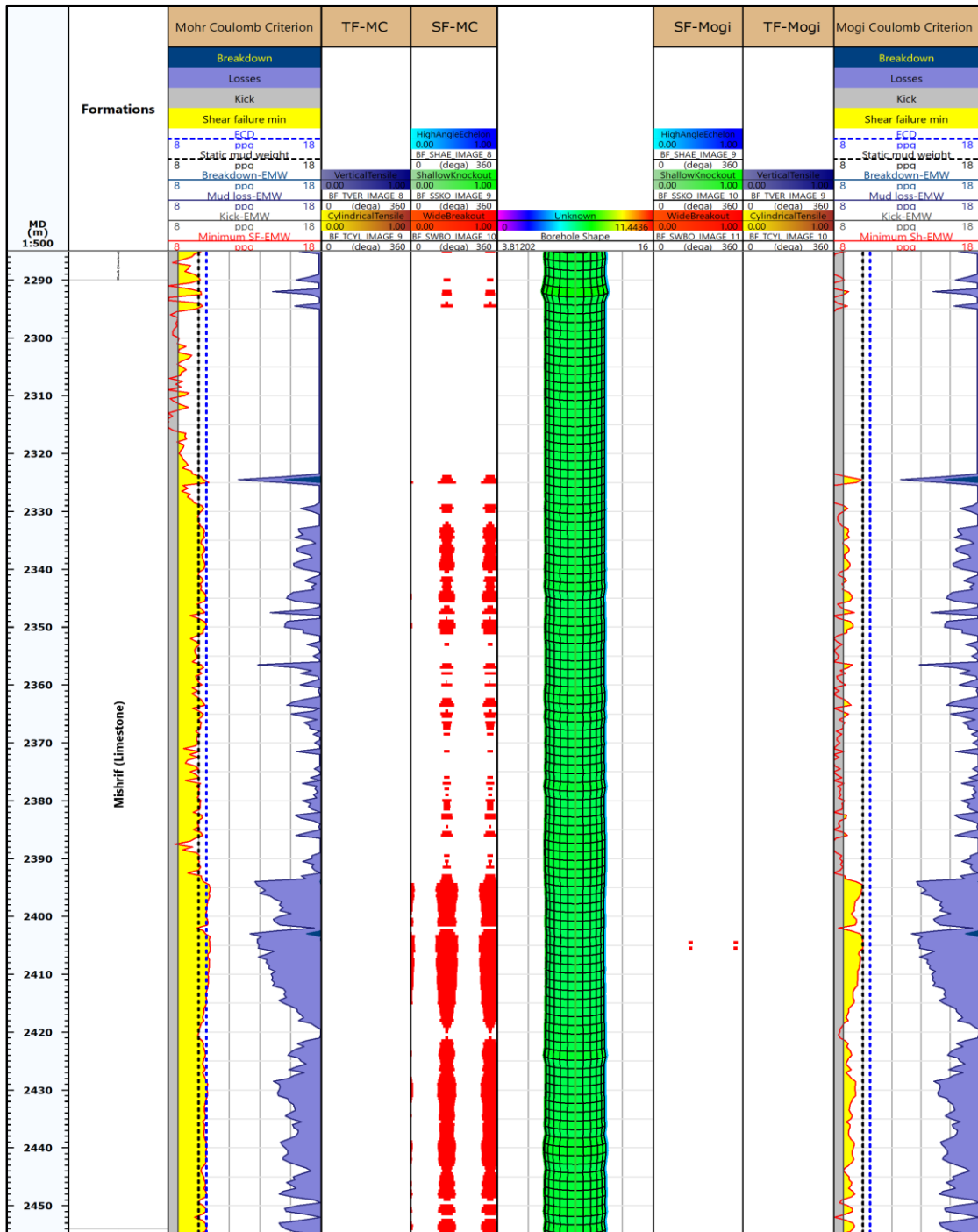
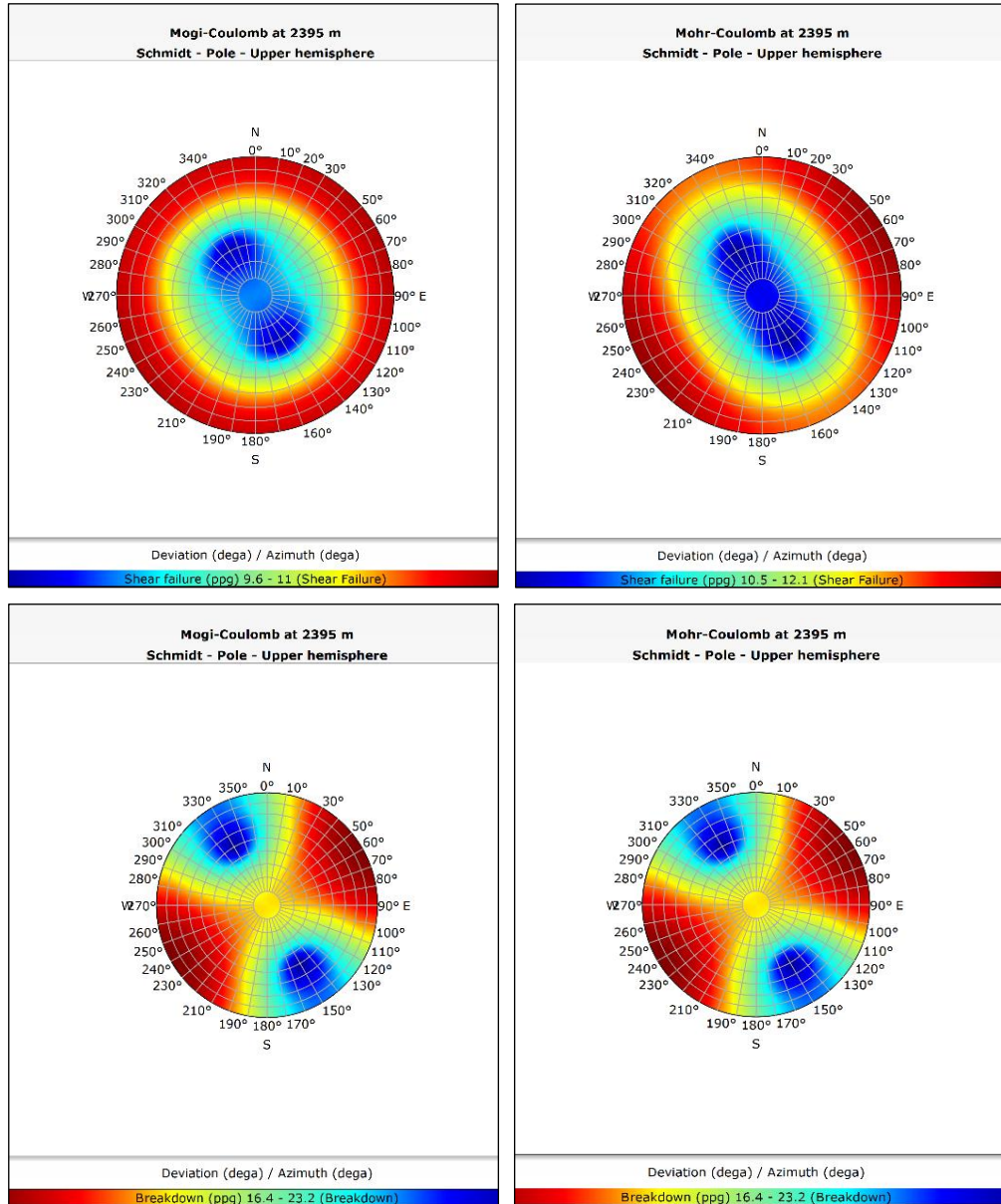


Figure 4. 34 Wellbore stability analysis with Mogi-Coulomb versus Mohr Coulomb criterion in Mishrif formation, Published with Techlog 2020.1.1.

Mogi and Mohr anticipated the same mud weight at which the drilling induced tensile fracture initiate. Accordingly, the breakdown may happen in the minimum horizontal direction with the highest mud weight. But the prolonged hydrocarbon production from this interval makes the tensile failure detection a troublesome task.



**Figure 4. 35 Sensitivity analysis with Mogi-Coulomb versus Mohr Coulomb criterion at Mishrif formation, Published with Techlog 2020.1.1.**

Breakout is differentiated in both models. Higher fluid density is required to avoid shear failure in the case of the Mohr-Coulomb criterion. Importantly, all plots exhibit similar behavior and follow the same direction, which in turn greatly facilitates the optimal choice of borehole trajectory.

#### 4.4.5 Stability analysis with Mogi versus Mohr at Nahr Umr

The farthest sorts of shear failure were clearly exposed from 2825 to 2995 m, with good acceptance between both models and the caliper log. However, the Mohr criterion contradicted the borehole shape in the sandstone section from 2997 to 3073 m, whereas Mogi indicated tolerable anticipations, Figure 4.6.

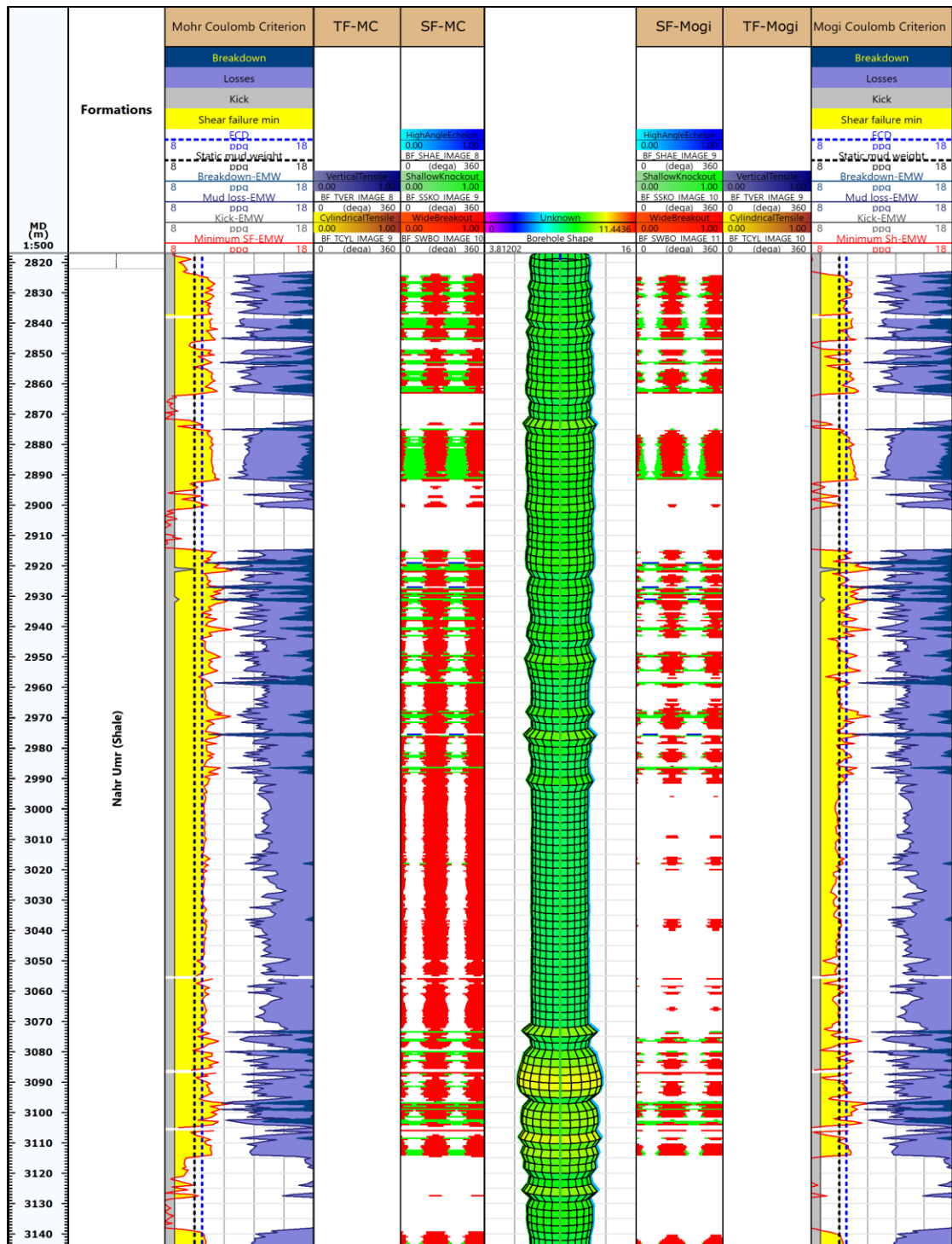
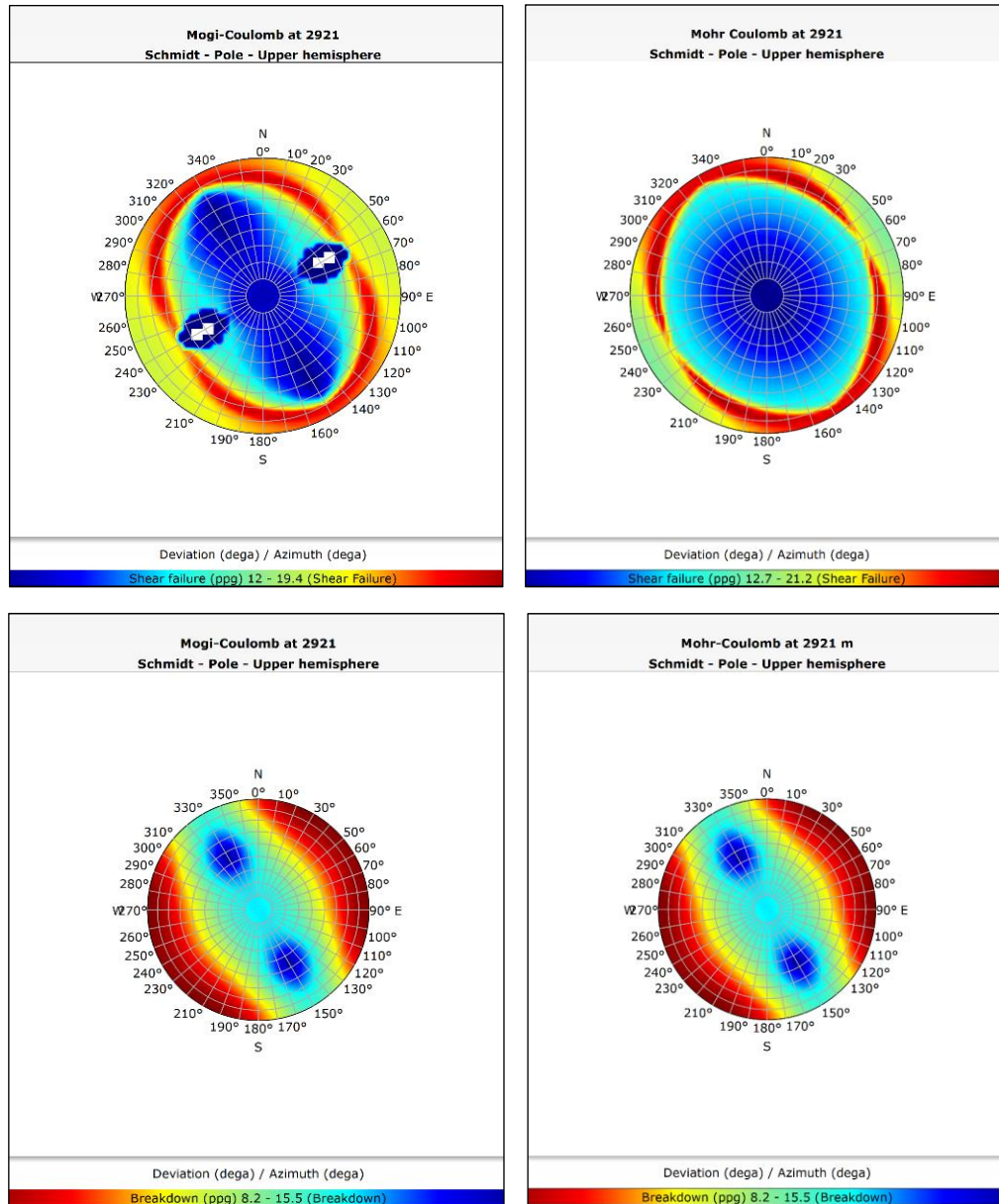


Figure 4.36 Wellbore stability analysis with Mogi-Coulomb versus Mohr Coulomb criterion in Nahr Umr formation, Published with Techlog 2020.1.1.

Mogi estimated trivial shear failures in some intervals of Nahr Umr formation, which were not detected by caliper log, Figure 4.36. Therefore, the mud logging report was revised. The report refers to the existence of thin layers of siltstone and shale that are characterized as weak rock, Figure 4.5.



**Figure 4. 37 Sensitivity analysis with Mogi-Coulomb versus Mohr Coulomb criterion at Nahr Umr formation, Published with Techlog 2020.1.1.**

In Figure 4.37 the breakdowns of Mogi and Mohr are the same and the only difference is in the shear failure. As usual Mohr-Coulomb underestimated the rock strength and consequently the shear failure was excessive and the desired mud weight to avoid breakout was higher than with Mogi.

#### 4.4.6 Stability analysis with Mogi versus Mohr at Zubair

Contrary to all the above, the only section where Mohr distinguished from Mogi in evaluating the development of shear failures is in the lithologies of Zubair members. The Mohr forecast in terms of borehole shape is better than Mogi, which underestimated the shear failure in several intervals from 3230 to 3500 m. There is no clear explanation for this difference except that Mohr-Coulomb may work better in transversely isotropic rocks.

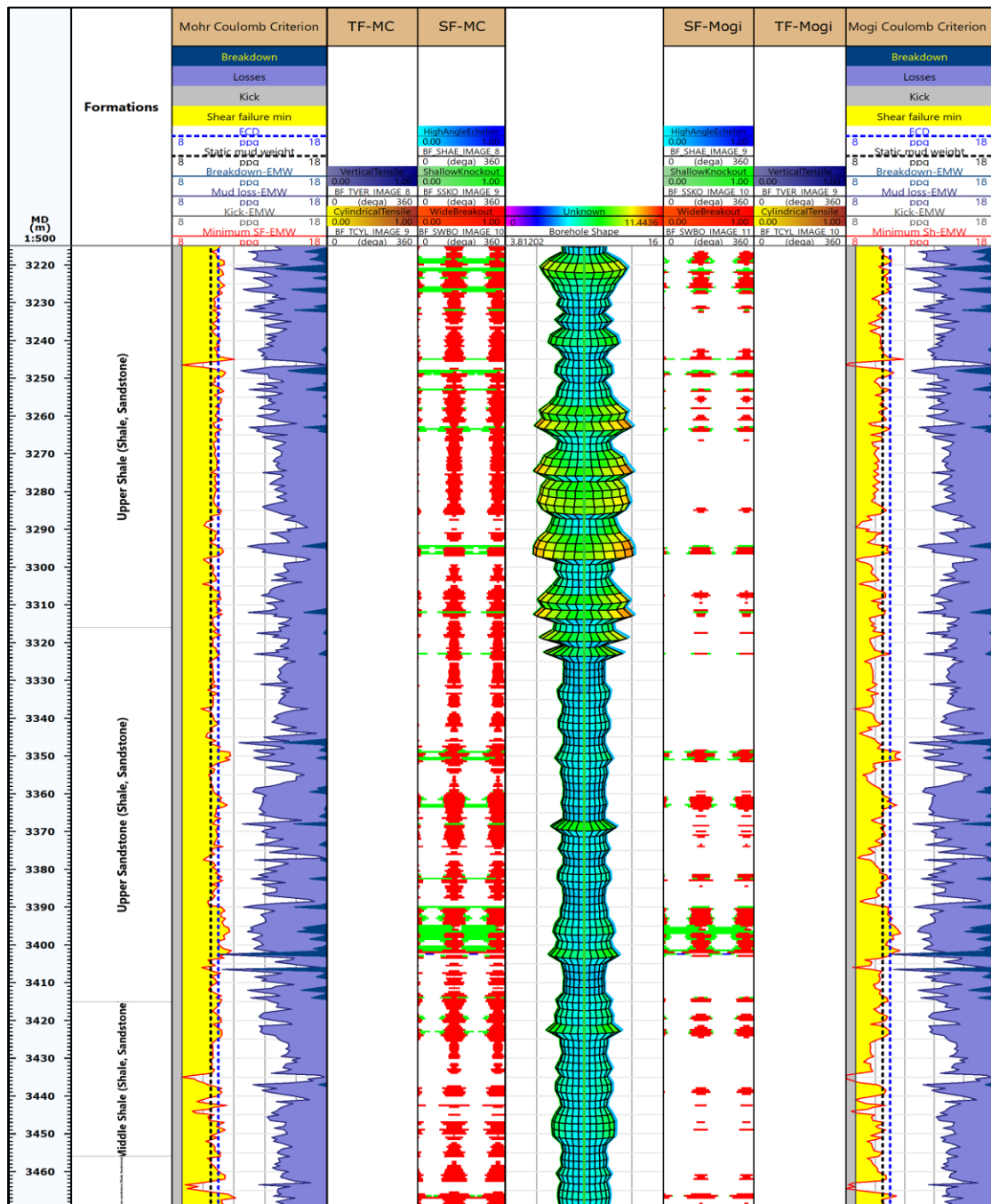
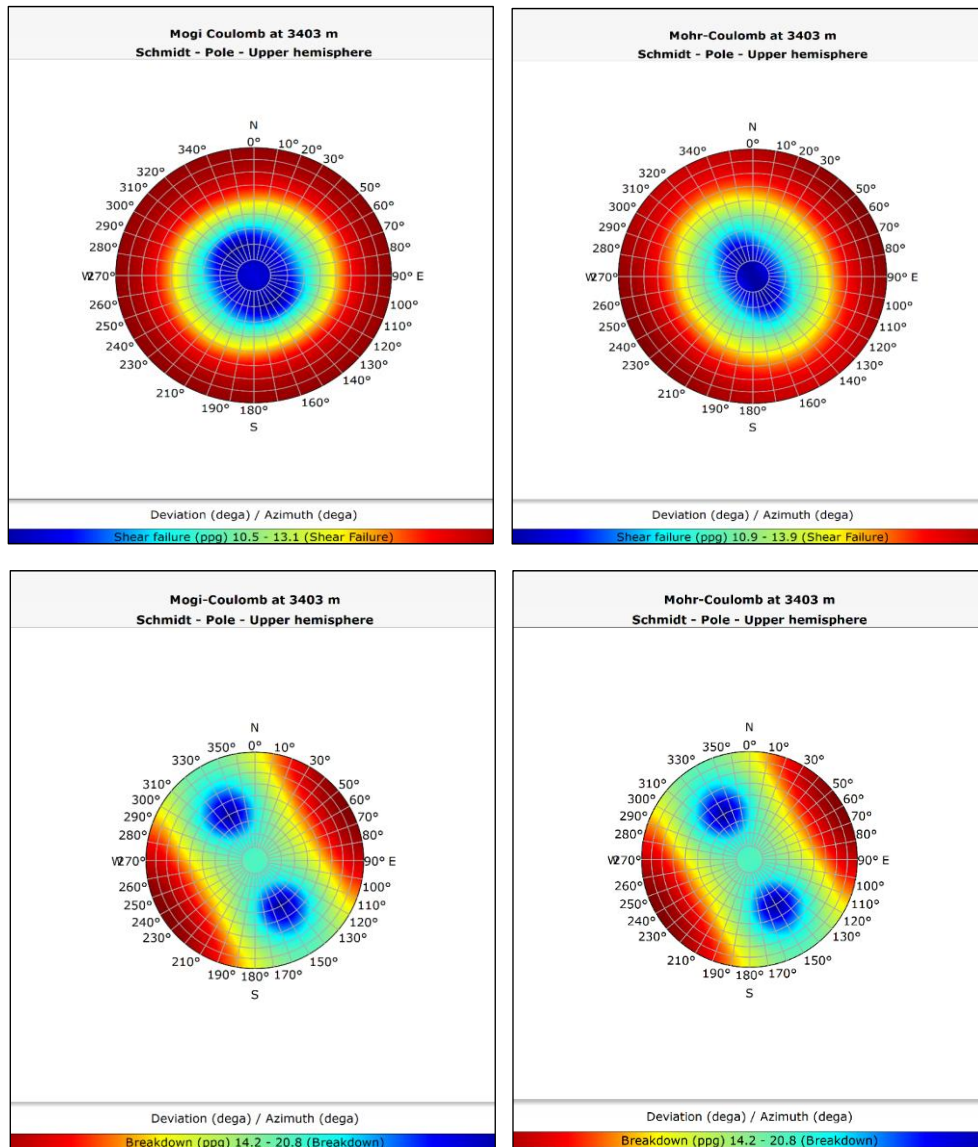


Figure 4. 38 Wellbore stability analysis with Mogi-Coulomb versus Mohr Coulomb in Zubair members formation, Published with Techlog 2020.1.1.

The stereonets of breakdown in both models are exactly the same as in the preceding sections. The only shear failure plots indicated a slight difference nearly in the direction of minimum horizontal stress, Figure 4.39. The analysis was implemented at 3403 m in the upper sandstone member.



**Figure 4. 39 Sensitivity analysis with Mogi-Coulomb versus Mohr Coulomb criterion at Zubair members formation, Published with Techlog 2020.1.1.**

## 4.5 Wellbore stability analysis with Drucker-Prager criterion

Drucker-Prager is a three-dimensional failure criterion based on Mohr–Coulomb criterion. (Alejano and Bobet 2012). Both types of Drucker-Prager, circumscribed and inscribed, were applied and compared with Mogi-Coulomb. Figure 4.40 depicts that the Drucker-Prager (circumscribed) overestimated the rock strength. Therefore, most of the

identified shear failures by caliper log were not anticipated by this criterion. Numerically, the model can be executed without difficulty, but the inaccuracy is immensely high.

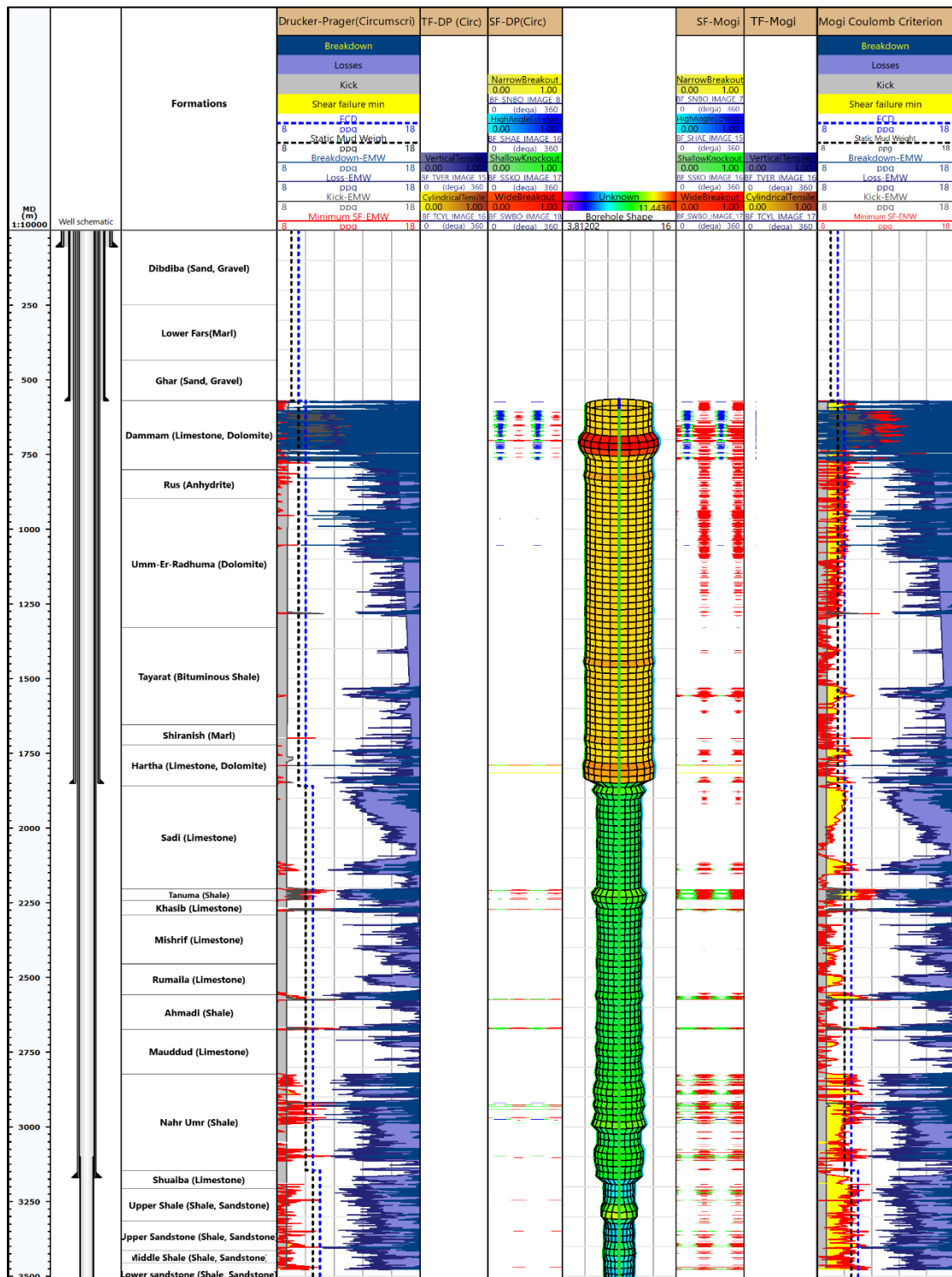


Figure 4. 40 Wellbore stability analysis with Drucker-Prager (circumscribed) versus Mogi Coulomb-Criterion, Published with Techlog 2020.1.1.

The behavior of Drucker-Prager (inscribed) is totally different from the circumscribed mode. The inscribed criterion underestimates the rock strength in exaggerated manner. Therefore, the whole constructed well is completely under shear failure, and this is far from the well circumstances, Figure 4.41.

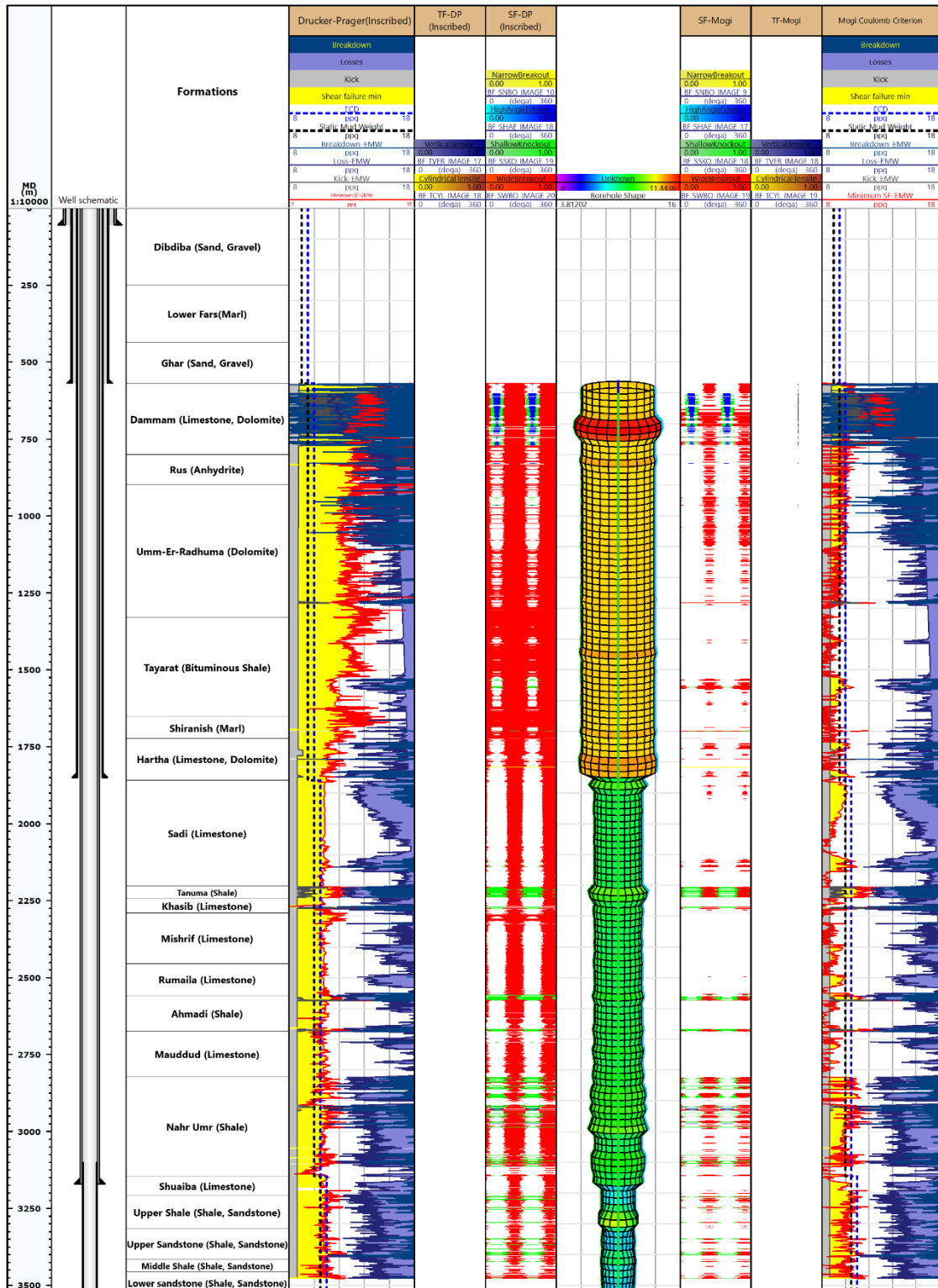


Figure 4. 41 Wellbore stability analysis with Drucker-Prager (inscribed) versus Mogi Coulomb-Criterion, Published with Techlog 2020.1.1.

## 4.6 Wellbore stability analysis with Stassi d'Alia Criterion

Stassi d'Alia is a simple strength criterion that yields the uniaxial compressive and uniaxial tensile strength (Wijk and Defence 2019). The equation of this criterion was just mentioned in *Fundamentals of Rock Mechanics* by Jaeger and Cook. Equation (4.34) was written by Stassi in 1967 (Åstrand 2015). Stassi d'Alia and Mogi behave similarly in the wellbore stability analysis of vertical well as denoted in Figure 4.42.

$$(\sigma_1 - \sigma_2)^2 + (\sigma_2 - \sigma_3)^2 + (\sigma_3 - \sigma_1)^2 = 2(C_0 - T_0)(\sigma_1 + \sigma_2 + \sigma_3) + 2C_0T_0 \quad 4.34$$

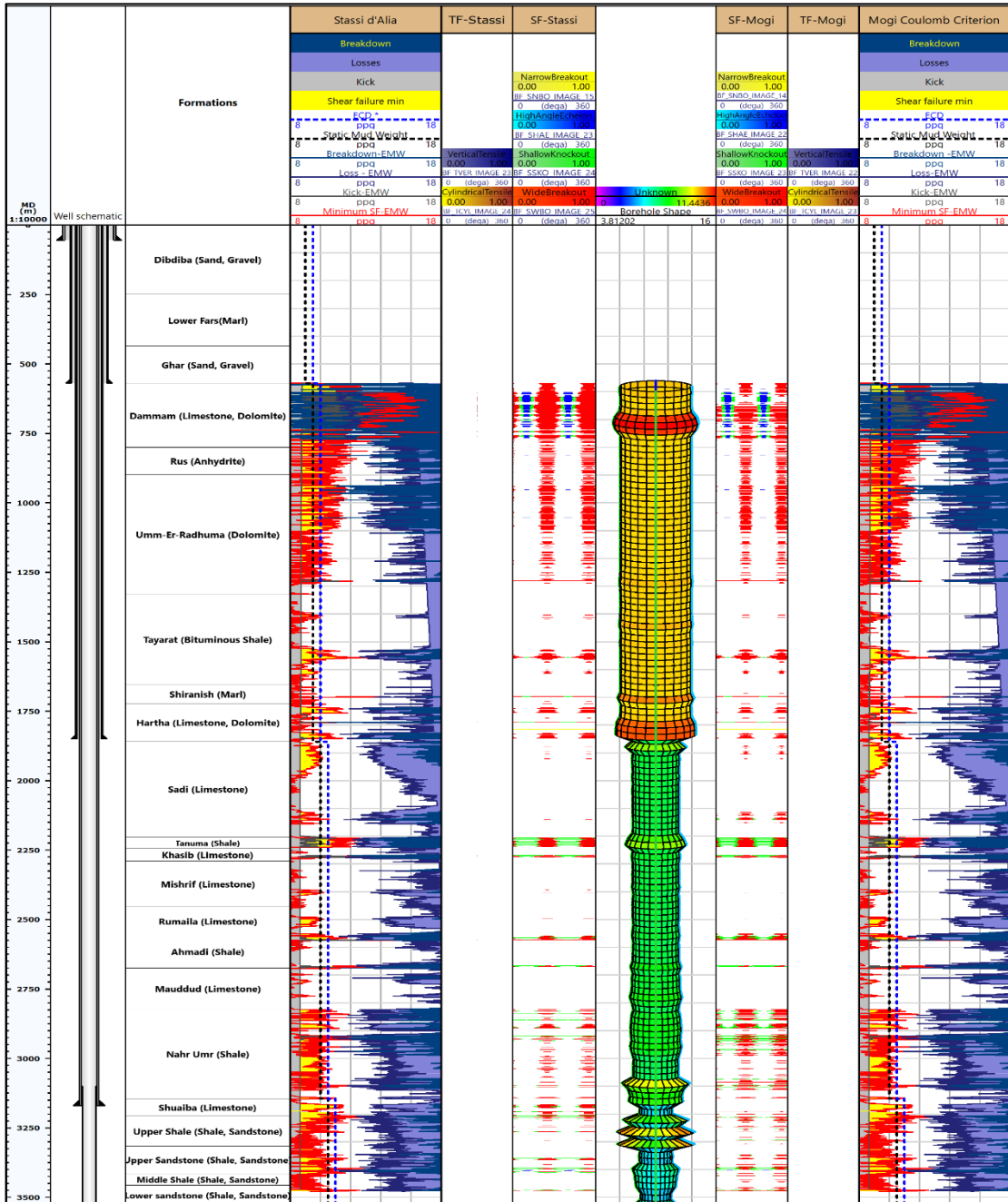


Figure 4. 42 Wellbore stability analysis with Stassi d'Alia versus Mogi-Coulomb Criterion, Published with Techlog 2020.1.1.

## 4.7 Horizontal Well Design

Nowadays, high percentages of produced oil and gas come from directional and horizontal wells around the world. Sometimes surface and subsurface conditions such as locations restrictions, environmental determinants and reservoir requirements necessitate drilling these kinds of well. At the beginning, horizontal wells extend just a few hundreds of meters horizontally. Then, extended reach drilling (ERD) can cover over 10000 m (F.Mitchell and Z.Miska 2011). ERD forms a horizontal or highly deviated well whose measured depth is at least twice its vertical depth (Agbaji 2010).

### 4.7.1 Well Trajectory

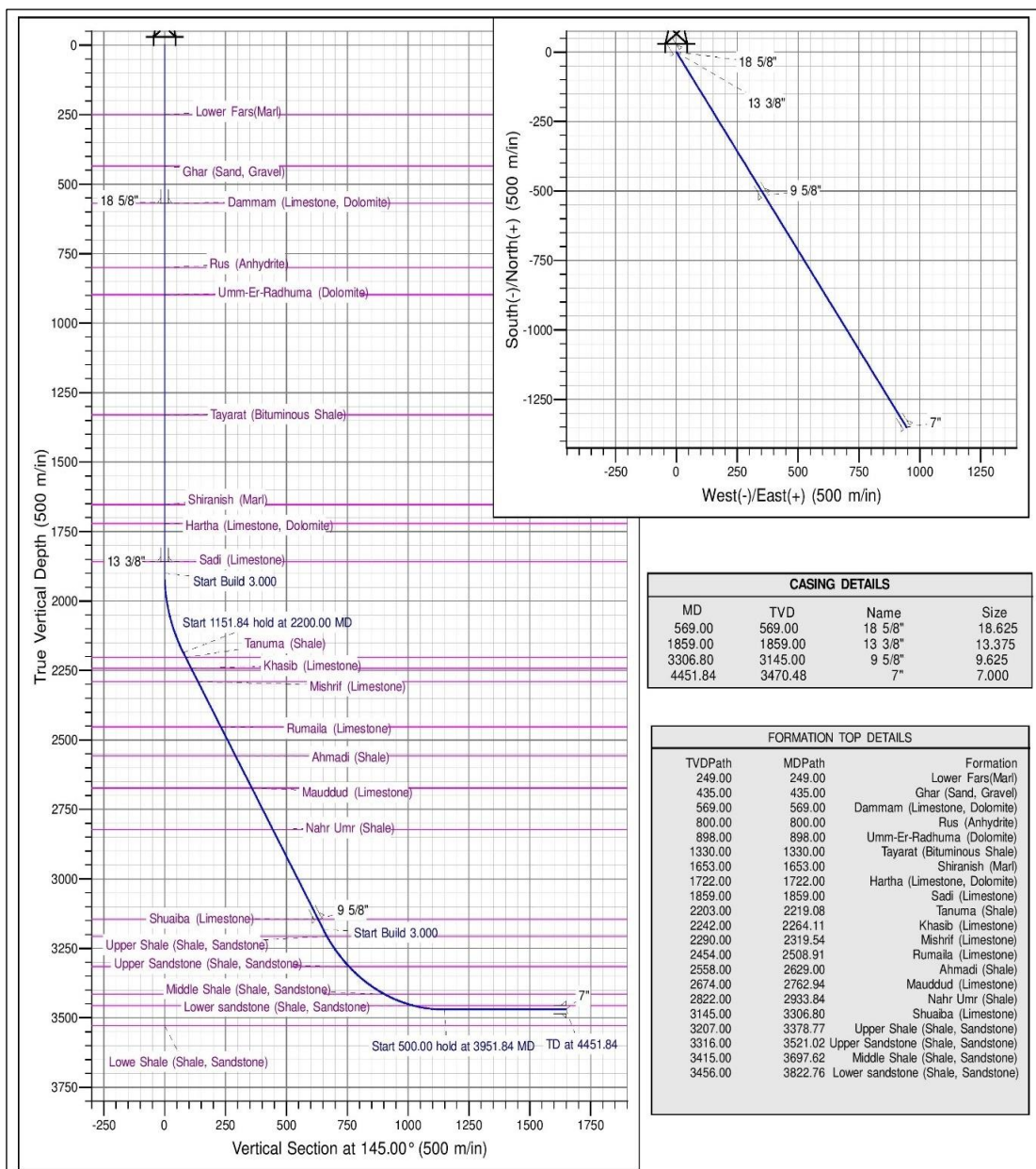
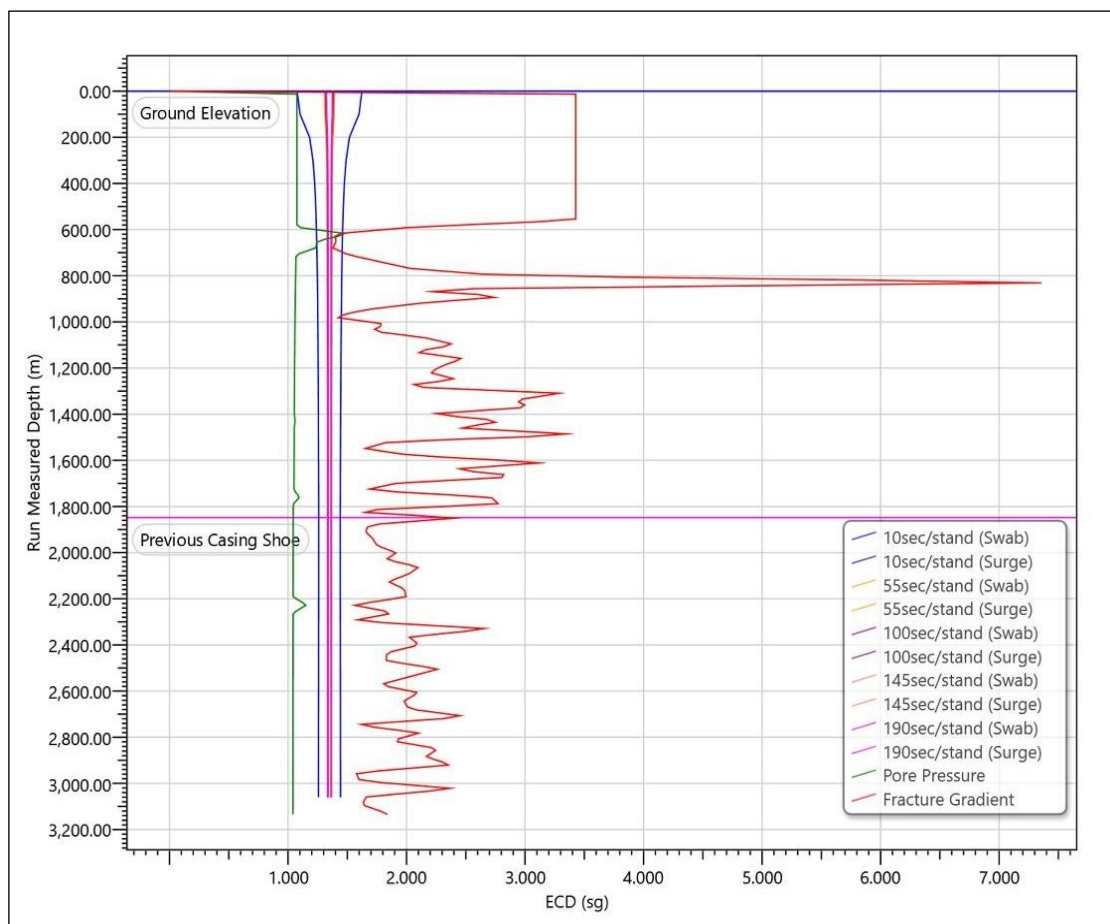


Figure 4. 43 Wellbore trajectory of Horizontal Well, Published with Landmark 5000.15

High precision in design is essential in horizontal wells due to the complexity, whether in hydraulic or geomechanical design, and consequently in the well plan. This study was dedicated for that purpose. Therefore, after finalizing the earth mechanical model with Mogi and Mohr Coulomb criterion, Mogi prediction of sensitivity analysis was selected. The analysis was used to define the mud weight for each selected critical lithology with optimized wellbore inclination and hole direction to 145 deg. Figure 4.43 represents the proposed horizontal wellbore trajectory with 4451 m measured depth and 500 m horizontal distance in the production zone.

#### 4.7.2 Equivalent circulation density in 12.25" hole section

In hydraulic design of a 12.25" hole section, all of the wellbore stability considerations were included, the shear failure possibility in equivalent static density (ESD) and the tensile failure in equivalent circulation density (ECD). Nahr Umr formation is the most critical interval with respect to the probability of shear failure according to the Mogi mud window.



**Figure 4. 44 Equivalent circulation density versus depth in 12.25", Published with Landmark 5000.15**

In a vertical or deviated well with up to 60 deg. of inclination in the minimum horizontal stress direction, a static mud weight of 1.44 g/cm<sup>3</sup> is desired to avoid breakout in Nahr Umr formation, Figure 4.45. On the other hand, the equivalent circulation density with 1.44 g/cm<sup>3</sup> is 1.48 g/cm<sup>3</sup>, a density which is unbearable by the depleted Mishrif formation in the same section. Therefore, daily drilling reports of more than 20 vertical and deviated wells have been revised; it was noticed that 1.25-1.35 g/cm<sup>3</sup> mud weight was utilized to drill this section. Since the behavior is the same in both vertical and deviated profiles, 1.35 g/cm<sup>3</sup> with ECD of 1.37 g/cm<sup>3</sup> has been selected.

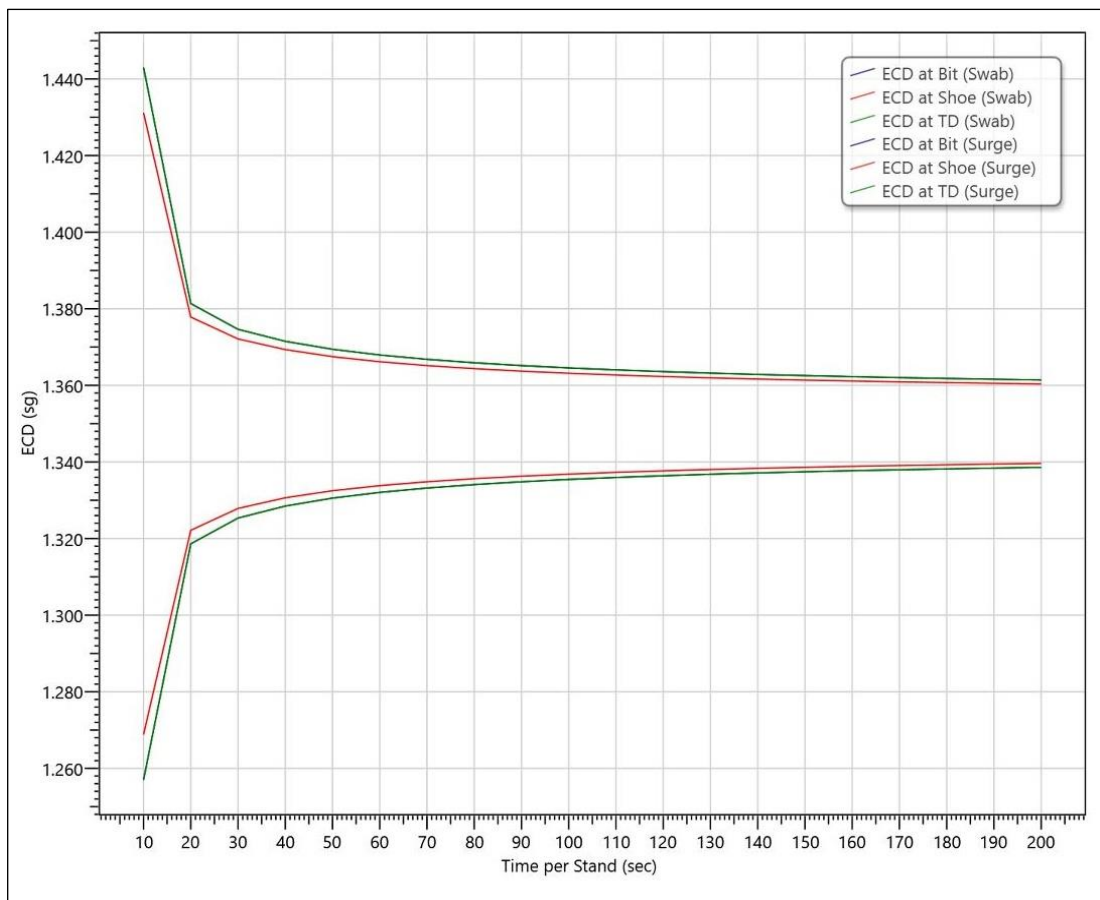


**Figure 4. 45 Equivalent circulation density versus trip time close ended in 12.25", Published with Landmark 5000.15**

### 4.7.3 Equevalent circulation density in 8.5" hole section

The specific hydraulic design in an 8.5" hole section can be implemented in all of the Zubair domes with the exception of Safwan, Figure 1.1. The reason is that the Shuaiba formation is composed of a porous vuggy dolomite, unlike the rest of the domes, and the lithology is compact limestone with high UCS. Therefore, the mud loss

in Shuaiba formation of Safwan dome is unavoidable. Figures 4.46 and 4.47 outline the circulation density with static mud weight of 1.57 g/cm<sup>3</sup>.

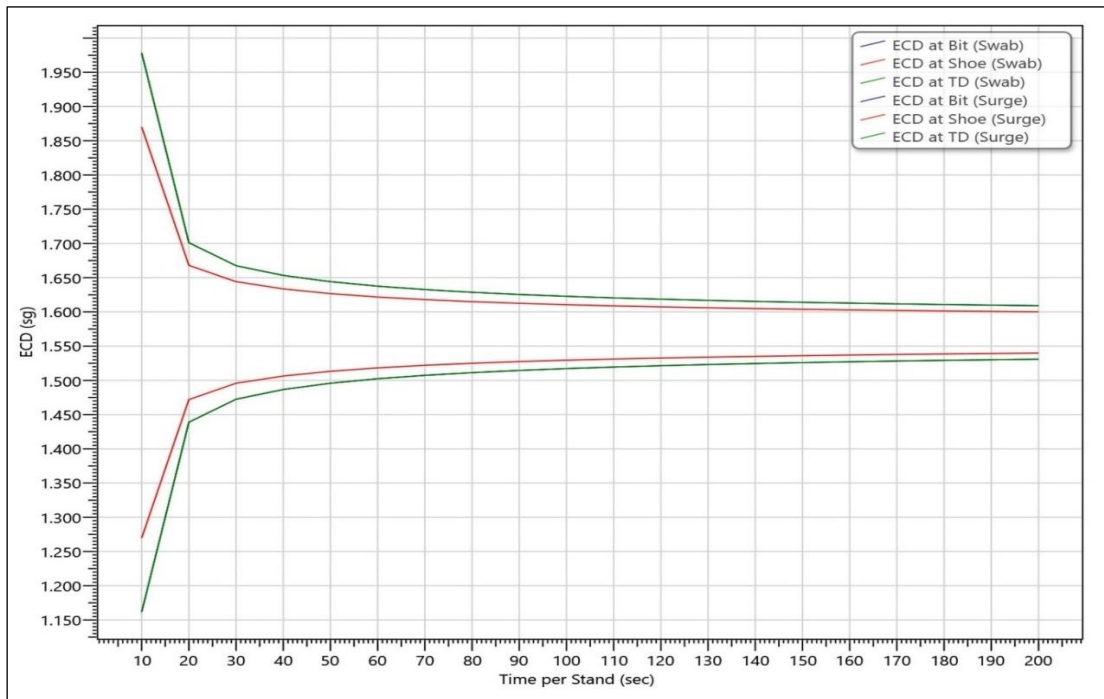


**Figure 4. 47 Equivalent circulation density versus trip time close ended in 8.5", Published with Landmark 5000.15**

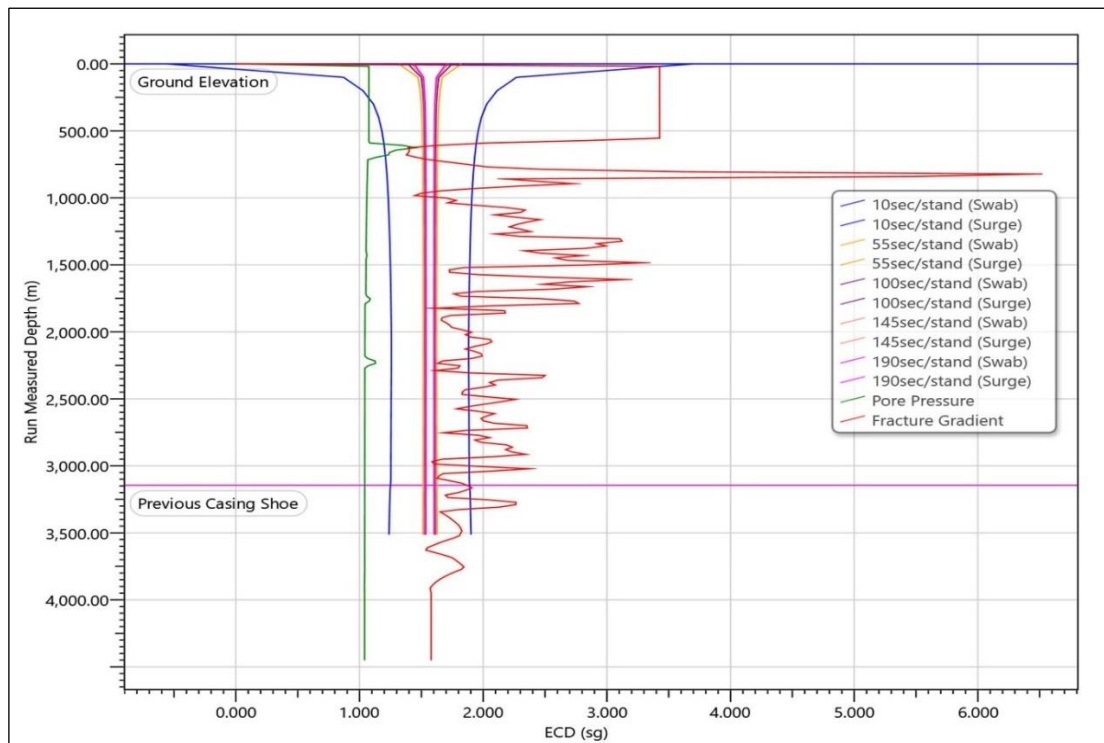


**Figure 4. 46 Equivalent circulation density versus depth in 8.5", Published with Landmark 5000.15**

## **Conclusions, Recommendations and Future Work**

### **5.1 Conclusions and recommendations**

The study was dedicated for wellbore stability analysis of highly deviated and horizontal wells in Zubair field. Real data of eleven development wells and one exploratory well have been employed to determine the rock mechanical strength, pore pressure and field in-situ stresses. Unluckily, the data on which the research was conducted starts from 569 m, not from the surface, otherwise the study would have been more comprehensive. The outcomes of calculations were then used to construct the MEM by means of the most common failure models, Mohr and Mogi-Coulomb criteria. The actual utilized mud weight in the ZB-233 and ZB-202 have been executed in both models to evaluate the Shear and Tensile failures, then the same were compared with the borehole shape. In addition, sensitivity analysis was implemented in the most critical intervals to define the required mud density for each inclination and azimuth. Thereafter, Mogi was placed versus Mohr-Coulomb and the conclusions are summarized below.

- Geophysical logs have been used from one exploratory well and one development well in order to cover most of the field's vertical section. In order to avoid uncertainty, this approach is not normally recommended, but the wells are located in the same area with exactly the same lithology and tectonic activity. For that reason, this process has been followed. On the other hand, the laboratory tests used were from the same development well.
- Any recorded uncertainty may relate to the hole conditions. The further the enlargement the higher the model uncertainty. Thus, the model was constructed based on mechanical properties and elastic data derived from sonic and density logs. Therefore, any over gauged hole will impact on the ultimate log readings and consequently maximize the results' unreliability.
- More Triaxial and Brazilian tests, as well as Hydro frac or extended leak-off test are indispensable to maximize the model's accuracy.
- Plausible correspondence was observed in most of the dynamic parameters that were calculated with logs data, except for some slight differences which were noticed here and there. The most obvious element that exhibited divergence between what was calculated and measured is the friction angle. The reason is that the measured values with Triaxial tests were somewhat exaggerated in the sedimentary rocks of the field.

- Horizontal stresses have been evaluated with two indirect methods, Poro-elastic and Mohr-Coulomb. The Poro-Elastic Horizontal Strain Model exhibited reasonable continuous profiles that are compatible with respect to the measured points of Hydro-Frac. Furthermore, the Anderson's fault classification was categorized as in agreement with the seismic interpretation of the field, unlike the Mohr-Coulomb stress model which failed to give reasonable results regarding Hydro-Frac or seismic data.
- The directions of Horizontal stresses were specified based on the Formation Micro Imager processing. Accordingly, the tensile fractures azimuth was on average consonant with the orientation of maximum horizontal stress in the world stress map field.
- In most investigated intervals, good acceptance was registered between shear failure predicted by Mogi-Coulomb criterion and borehole shape, while Mohr overvalued in shear failures prediction. Furthermore, Stassi d'Alia and Mogi-Coulomb acted similarly in the wellbore stability analysis of the vertical well.
- Mohr-Coulomb magnified the shear failure in the majority of geological sections, but there was outstanding anticipation of shear failure in the parts containing transversely isotropic rocks. Therefore, Mohr Coulomb modeled all kinds of breakout in a better way than Mogi in Zubair members' lithologies.
- Interestingly, drilling induced tensile fractures was identified excellently by both models in the Dammam formation which experienced mud loss while drilling. Moreover, the tensile fractures orientation in that formation was specified in two directions and both represent the maximum horizontal stress azimuth.
- High Angle Echelon shear failure expressed high resemblance for both criteria, whether in depth or severity. In the sensitivity analysis, the same similarity was noticed in breakdown mud window versus deviation / azimuth. All stereonet plots of tensile failures displayed the same results in both models.
- The horizontal well with 90 deg. in the Zubair members formation desired 1.57 g/cm<sup>3</sup> as static mud weight. Equivalent circulation density (ECD) with mud flow rate of 2000 LPM may reach 1.67 g/cm<sup>3</sup>, considering that the maximum allowable mud weight in this section is 1.70 g/cm<sup>3</sup> in Zubair formation, to avoid tensile failure. Furthermore, the depletion in the reservoirs of this section due to the prolonged hydrocarbon production must be considered.
- The shale formation of Zubair field is mechanically and chemically stressed shale. Subsequently, oil-based mud or water-based mud with appropriate shale control additives must be utilized in order to get away from water shale

interaction. Correspondingly, shale special tests such as X-Ray diffraction test (XRD), Linear Swell meter (LSM) and Cation exchange capacity (CEC) should be performed along shale sections to define the water reactivity.

- Particle size distribution analysis (PSD) is also important to define a suitable size of Lost Circulation Materials (LCM). Some kinds of LCM may help to increase the tensile strength of rocks and avoid loss, especially in depleted zones.
- Finally, drilling practice plays a major role in controlling the wellbore stability, particularly while tripping in and out.

## **5.2 Future Work**

Data of two wells have been employed to define the final model to represent the whole field. Lateral heterogeneity of the field must however be considered, because a one-dimensional mechanical earth model from a single well may not typify the entire field. Therefore, analysis of deterministic wellbore failure could be applied to consider slight discrepancies within the data. To achieve this, high quality geophysical logs with laboratory tests data from four wells on the same dome of the field are mandatory to build a three-dimensional mechanical earth model. Therefore, the required future work is construction of a 3D MEM with deepest investigation.

## REFERENCES

- Aadnøy, Bernt S., and Reza Looyeh. 2011. *Petroleum Rock Mechanics: Drilling Operations and Well Design*. ELSEVIER.
- Abdideh, Mohammad, and Sina Alisamir. 2018. "Analysis of Deep Stress Field Using Well Log and Wellbore Breakout Data: A Case Study in Cretaceous Oil Reservoir, Southwest Iran."
- Adebayo, Babatunde, Zacheus Olaniyan Opafulunso, and Jide Milliu Akande. 2010. "Drillability and Strength Characteristics of Selected Rocks in Nigeria." *Assumption University Journal of Technology* 14(1):56–60.
- Adham, Aidil. 2016. "Geomechanics Model for Wellbore Stability Analysis in Field 'X' North Sumatra Basin." 109.
- Agbaji, Armstrong Lee. 2010. "Optimizing the Planning, Design and Drilling of Extended Reach and Complex Wells." *Society of Petroleum Engineers - SPE/DGS Saudi Arabia Section Technical Symposium and Exhibition 2011* 841–53.
- Agharazi, Alireza. 2016. "Determining Maximum Horizontal Stress with Microseismic Focal Mechanisms – Case Studies in the Marcellus, Eagle Ford, Wolfcamp." in *SPE/AAPG/SEG Unconventional Resources Technology Conference 2016*.
- Al-Ajmi, A. M., and R. W. Zimmerman. 2006. "Stability Analysis of Deviated Boreholes Using the Mogi-Coulomb Failure Criterion, with Applications to Some Oil and Gas Reservoirs." *Proceedings of the IADC/SPE Asia Pacific Drilling Technology Conference 2006 - Meeting the Value Challenge: Performance, Deliverability and Cost 2006*(November):537–50.
- Al-Ameri, N. Jasim, and Wafa Al-Kattan. 2012. "Estimation of the Rock Mechanical Properties Using Conventional Log Data in North Rumaila Field." *Iraqi Journal of Chemical and Petroleum Engineering* 13(4):27–33.
- Al-Jafar, Methaq Kh, and Mohanad H. Al-Jaberi. 2019. "Well Logging and Electrofacies of Zubair Formation for Upper Sandstone Member in Zubair Oil Field, Southern Iraq." *Iraqi Geological Journal* 52(1):101–24.
- AL-Mutury, Wathiq, and Dawod Al-Mayahi. 2015. "Geometric and Genetic Structural Analysis of Zubair Oil Field, Southern Iraq." *AL-Qadisiya Journal For Science Vol* 15(N0.3).
- Alejano, Leandro R., and Antonio Bobet. 2012. "Drucker-Prager Criterion." *Rock Mechanics and Rock Engineering* 45(6):995–99.
- Ameen, Mohammed S., Brian G. D. Smart, J. Mc Somerville, Sally Hammilton, and Nassir A. Naji. 2009. "Predicting Rock Mechanical Properties of Carbonates from Wireline Logs (A Case Study: Arab-D Reservoir, Ghawar Field, Saudi Arabia)." *Marine and Petroleum Geology* 26(4):430–44.
- Aslannezhad, Masoud, Abbas Khaksar manshad, and Hossein Jalalifar. 2016. "Determination of a Safe Mud Window and Analysis of Wellbore Stability to Minimize Drilling Challenges and Non-Productive Time." *Journal of Petroleum Exploration and Production Technology* 6(3):493–503.
- Åstrand, Gustaf Johan. 2015. "Borehole Stability: Comparing the Deviation Sensibility of Different Failure Criteria." *Master's Thesis, NTNU* (June):127.
- Azadpour, Morteza, and Navid Shad Manaman. 2015. "Determination of Pore Pressure from Sonic Log: A Case Study on One of Iran Carbonate Reservoir Rocks." *Iranian Journal of Oil and Gas Science and Technology*, 4(3):37–50.
- Bailey, Adam H. E., Rosalind C. King, Simon P. Holford, and Joshua M. Sage. 2015. "Variation of Natural Fracture Orientations in the Carnarvon Basin's Rankin

- Platform and Dampier Sub-Basin, NWS, Western Australia.” *ASEG Extended Abstracts* 2015(1):1–4.
- Beeler, N. M., Greg Hirth, and Amanda Thomas. 2016. “Effective Stress, Friction, and Deep Crustal Faulting.” *Journal of Geophysical Research: Solid Earth* 121(2):767–87.
- Bewick, R. P., P. K. Kaiser, and F. Amann. 2019. “Strength of Massive to Moderately Jointed Hard Rock Masses.” *Journal of Rock Mechanics and Geotechnical Engineering* 11(3):562–75.
- Bradford, I. D. R., J. Fuller, P. J. Thompson, and T. R. Walsgrove. 1998. “Benefits of Assessing the Solids Production Risk in a North Sea Reservoir Using Elastoplastic Modelling.” *SPE/ISRM Rock Mechanics in Petroleum Engineering. Society of Petroleum Engineers*.
- Briševac, Zlatko, Trpimir Kujundžić, and Sandi Čajić. 2015. “Sadašnje Spoznaje o Ispitivanju Vlačne Čvrstoće Stijena Uporabom Brazilskoga Testa.” *Rudarsko Geolosko Naftni Zbornik* 30(2):101–14.
- Celerier, Bernard. 2008. “Seeking Anderson’s Faulting in Seismicity: A Centennial Celebration.” *Reviews of Geophysics* (2007):1–34.
- Chang, Chandong, Mark D. Zoback, and Abbas Khaksar. 2006. “Empirical Relations between Rock Strength and Physical Properties in Sedimentary Rocks.” *Journal of Petroleum Science and Engineering* 51(3–4):223–37.
- Civan, Faruk. 2020. “Effective-Stress Coefficients of Porous Rocks Involving Shocks and Loading/Unloading Hysteresis.” *SPE Journal* (September 2019):1–24.
- Claesson, J., and B. Bohloli. 2002. “Brazilian Test: Stress Field and Tensile Strength of Anisotropic Rocks Using an Analytical Solution.” *International Journal of Rock Mechanics and Mining Sciences* 39(8):991–1004.
- D. Zoback, Mark. 2007. “Reservoir Geomechanics.” in *Reservoir Geomechanics*. Cambridge: Cambridge University Press.
- Das, Troyee, and Soumyajit Mukherjee. 2020. “Pore Pressure Determination Methods.” *Sediment Compaction and Application in Petroleum Geoscience* (January).
- Deangeli, Chiara, and Omoruyi Omoman Omwanghe. 2018. “Prediction of Mud Pressures for the Stability of Wellbores Drilled in Transversely Isotropic Rocks.” *Energies* 11(8).
- Donald, J. A., E. J. Wielemaker, F. Karpfinger, F. Gomez, X. Liang, and M. Tingay. 2015. “Qualifying Stress Direction from Borehole Shear Sonic Anisotropy.” *49th US Rock Mechanics / Geomechanics Symposium 2015* 1(December):784–93.
- Dusseault, Maurice B., Vincent Maury, Francesco Sanfilippo, and Frédéric J. Santarelli. 2004. “Drilling around Salt: Risks, Stresses, and Uncertainties.” *Gulf Rocks 2004 - 6th North America Rock Mechanics Symposium, NARMS 2004*
- Eide, H.S., Cecilie. 2012. “Understanding Drilling Induced Fractures Spring.” *Master’s Thesis, University of Stavanger, Norway* (June).
- Ezati, Mohsen, and Bahman Soleimani. 2014. “Fracture and Horizontal Stress Analysis of Dalan Formation Using FMI Image Log in One of Southwestern Iranian Oil Wells Mohsen Ezati\* 1 , Bahman Soleimani 1 , Mohamad Safarkhan Moazeni 1 1-.” *Journal of Tethys*, 2(1), 1-8. 2(1):1–8.
- F.Mitchell, Robert, and Stefan Z.Miska. 2011. *Fundamentals of Drilling Engineering*. Vol. 12.
- Fallahzadeh, Seyed Hassan, Md Mofazzal Hossain, Ashton James Cornwell, and Vamegh Rasouli. 2017. “Near Wellbore Hydraulic Fracture Propagation from Perforations in Tight Rocks: The Roles of Fracturing Fluid Viscosity and Injection Rate.” *Energies* 10(3).

- FEMI-OYEWOLE, Damilola FEMI-OYEWOLE. 2018. "Politecnico Di Torino." *Master Thesis, Politecnico Di Torino* (March):157.
- Fjaer, E., R. M. Holt, P. Horsrud, A. M. Raaen, and R. Risnes. 2008. *Petroleum Related Rock Mechanics*. Vol. 33. Elsevier.
- García, Ricardo Andrés, Néstor Fernando Saavedra, Zuly Calderón-Carrillo, and Darwin Mateus. 2008. "Development of Experimental Correlations between Indentation Parameters and Unconfined Compressive Strength (UCS) Values in Shale Samples." *CTyF - Ciencia, Tecnología y Futuro* 3(4):61–81.
- Gholami, R., A. Moradzadeh, V. Rasouli, and J. Hanachi. 2014. "Practical Application of Failure Criteria in Determining Safe Mud Weight Window in Drilling Operation."
- Gong, Fengqiang, Song Luo, Ge Lin, and Xibing Li. 2020. "Evaluation of Shear Strength Parameters of Rocks by Preset Angle Shear, Direct Shear and Triaxial Compression Tests." *Rock Mechanics and Rock Engineering* 53(5):2505–19.
- Guangzhi, Yin, Li He, and Xian Xuefu. 1988. "The Effect of the Stress Path on Strength of Rock." *29th U.S. Symposium on Rock Mechanics, USRMS 1988* 95–101.
- Haimson, Bezalel, and Charles Fairhurst. 1967. "Initiation and Extension of Hydraulic Fractures in Rocks." *Society of Petroleum Engineers Journal* 7(03):310–18.
- Hayavi, Mohammad Tabach, and Mohammad Abdideh. 2016. "Estimation of In-Situ Horizontal Stresses Using the Linear Poroelastic Model and Minifrac Test Results in Tectonically Active Area." *Russian Journal of Earth Sciences* 16(4):1–9.
- Himmelberg, Nevan Christopher. 2014. "Numerical Simulations for Wellbore Stability and Integrity for Drilling and Completion." *Petroleum Engineering Msc*:173.
- Horsrud, Per. 2001. "Estimating Mechanical Properties of Shale From Empirical Correlations." *SPE Drilling & Completion*, 16(02), 68-73. (June).
- Hubbert, M. KING, and DAVID G. WILLIS. 1957. "Mechanics of Hydraulic Fracturing." *Zentralblatt Fur Chirurgie* 103(16):1052–54.
- Ibrahim, Ahmed Farid, and Hisham Nasr-El-Din. 2018. "Evaluation of the Breakdown Pressure to Initiate Hydraulic Fractures of Tight Sandstone and Shale Formations." *Society of Petroleum Engineers - SPE Trinidad and Tobago Section Energy Resources Conference 2018* (July).
- Islam, M. A., P. Skalle, A. M. Al-Ajmi, and O. K. Søreide. 2010. "Stability Analysis in Shale through Deviated Boreholes Using the Mohr and Mogi-Coulomb Failure Criteria." *44th US Rock Mechanics Symposium - 5th US/Canada Rock Mechanics Symposium* (June).
- Jaeger, J. C., N. G. W. Cook, and R. W. Zimmerman. 2007. *Fundamentals of Rock Mechanics*.
- John Lander Ichenwo, Adewale Dosunmu. 2017. "Estimation of Horizontal Stresses and Stress Directions from Inversion of Leak-off Test Data-A Computer Approach." *International Journal of Engineering Research and Technology (IJERT)* 4(4):199–206.
- K. Sissakian, Varoujan, Ayda D. Abdul Ahad, Nadhir Al-Ansari, and Sven Knutsson. 2017. "Geomorphology, Geology and Tectonic of Jabal Sanam, Southern Iraq." 17.
- Khaksar, A., P. G. Taylor, Z. Fang, T. Kayes, A. Salazar, and K. Rahman. 2009. "Rock Strength from Core and Logs: Where We Stand and Ways to Go." *Society of Petroleum Engineers - EUROPEC/EAGE Conference and Exhibition 2009* (June):8–11.
- Kidambi, Tapan, and G. Suresh Kumar. 2016. "Mechanical Earth Modeling for a Vertical Well Drilled in a Naturally Fractured Tight Carbonate Gas Reservoir in

- the Persian Gulf.” *Journal of Petroleum Science and Engineering* 141:38–51.
- Komurlu, Eren, and Aysegul Durmus Demir. 2018. “Determination of Cohesion Values of Rock Materials Using Double Shear Jaws.” *Periodica Polytechnica Civil Engineering* 62(4):881–92.
- Konietzky, Heinz, and Mohamed Ahmed Ismael. 2018. “Failure Criteria for Rocks.” *Introduction into Geomechanics* (March):20.
- Krupnick, Alan J., and Isabel Echarte. 2017. “Induced Seismicity Impacts of Unconventional Oil and Gas Development.” *Resources for the Future* (June).
- Kundan, Ashani, and Souvik Sen. 2015. “Analysis of Wellbore Breakouts and Determination of Horizontal Stress Direction from Four Arm Calipers – A Study from Gulf of Kutch , Western Offshore Basin.” *In 11th Biennial International Conference & Exposition, SPG, Jaipur, India. Paper ID (Vol. 37)*. (June 2016):0–
- Lang, James, Shuling Li, and Jincai Zhang. 2011. “Wellbore Stability Modeling and Real-Time Surveillance for Deepwater Drilling to Weak Bedding Planes and Depleted Reservoirs.” *SPE/IADC Drilling Conference, Proceedings* 1:145–62.
- Li, Diyuan, and Louis Ngai Yuen Wong. 2013. “The Brazilian Disc Test for Rock Mechanics Applications: Review and New Insights.” *Rock Mechanics and Rock Engineering* 46(2):269–87.
- Lin, Huasheng, Joung Oh, Hossein Masoumi, Ismet Canbulat, and Chengguo Zhang. 2018. “A Review of In Situ Stress Measurement Techniques.” *Coal Operators’ Conference* (February):95–102.
- Lin, Weiren, Koji Yamamoto, Hisao Ito, Hideki Masago, and Yoshihisa Kawamura. 2008. “Estimation of Minimum Principal Stress from an Extended Leak-off Test Onboard the Chikyu Drilling Vessel and Suggestions for Future Test Procedures.” *Scientific Drilling* (6, July 2008):43–47.
- MACAULAY, EKHALIALU OGIE, UKPONG ANIEDIOBONG JONAH, Ogidi Anthony Odama, A. S. I. M. A. Y. Okah, and Osung Wilson Edet. 2016. “Stratigraphic Characterization of Parts of the Awi Formation , Calabar Flank , South Eastern Nigeria.” 2(11):50–70.
- Markou, Nikolaos, and Panos Papanastasiou. 2018. “Petroleum Geomechanics Modelling in the Eastern Mediterranean Basin: Analysis and Application of Fault Stress Mechanics.” *Oil and Gas Science and Technology* 73(January).
- Mashinsky, E. I. 2003. “Differences between Static and Dynamic Elastic Moduli of Rocks: Physical Causes.” *Geologiya i Geofizika* 44(9):953–59.
- Nauroy, Jean-François. 2011. *Geomechanics Applied to the Petroleum Industry*. Editions Technip.
- Pašić, Borivoje. 2007. “Wellbore Instability: Causes and Consequences.”
- Peng, Suping, and Jincai Zhang. 2007. *Engineering Geology for Underground Rocks*. edited by S. S. & B. Media. Springer Science & Business Media.
- Raaen, A. M., P. Horsrud, H. Kjørholt, and D. Økland. 2006. “Improved Routine Estimation of the Minimum Horizontal Stress Component from Extended Leak-off Tests.” *International Journal of Rock Mechanics and Mining Sciences* 43(1):37–48.
- Rahimi, Reza. 2014. “The Effect of Using Different Rock Failure Criteria in Wellbore Stability Analysis.” *Masters Theses* 72.
- Rana, Rakesh Roshan, and C. Chandrashekhara. 2015. “Pore Pressure Prediction a Case Study in Cambay Basin.” *Geohorizons* (January):38–46.
- Russell, B., Tad Smith, and a Hampson-Russell. 2007. “The Relationship between Dry Rock Bulk Modulus and Porosity—an Empirical Study.” *CREWES Research Report* 19:1–14.

- Schlemmer, R., J. E. Friedheim, F. B. Growcock, J. B. Bloys, J. A. Headley, and S. C. Polnaszek. 2002. "Membrane Efficiency in Shale - An Empirical Evaluation of Drilling Fluid Chemistries and Implications for Fluid Design." *IADC/SPE Drilling Conference. Society of Petroleum Engineers*. (February).
- Schlunegger, Fritz, and Philippos Garfalakis. 2018. "Clast Imbrication in Coarse-Grained Mountain Streams and Stratigraphic Archives as Indicator of Deposition in Upper Flow Regime Conditions." *Earth Surface Dynamics* 6(3):743–61.
- Selvadurai, Patrick, Paul A. Selvadurai, and Morteza Nejati. 2019. "A Multi-Phasic Approach for Estimating the Biot Coefficient for Grimsel Granite." *Solid Earth* 10(6):2001–14.
- Sen, S., J. Corless, S. Dasgupta, C. Maxwell, and M. Kumar. 2017. "Issues Faced While Calculating Overburden Gradient and Picking Shale Zones to Predict Pore Pressure." *First EAGE Workshop on Pore Pressure Prediction (Pp. Cp-506). European Association of Geoscientists & Engineers* (March).
- Song, I., and B. C. Haimson. 1997. "Polyaxial Strength Criteria and Their Use in Estimating in Situ Stress Magnitudes from Borehole Breakout Dimensions." *International Journal of Rock Mechanics and Mining Sciences & Geomechanics Abstracts* 34(3–4):498.
- Song, Lisa. 2012. "Measurement of Minimum Horizontal Stress from Logging and Drilling Data in Unconventional Oil and Gas." *Master's Thesis, Graduate Studies* 53(9):1689–99.
- Tang, Xiao Ming, Sugar Land, and Douglas J. Patterson. 2008. "IMAGING NEAR-BOREHOLE REFLECTORS USING SHEAR WAVE REFLECTIONS FROM A MULTI-COMPONENT ACOUSTIC TOOL CROSS-REFERENCES." *U.S. Patent Application No. 11/961,349*. 1(19).
- Tiwari, R. R. 2013. "Recognizing Horizontal Stress Orientation for Optimizing Well Placement and Well Completion Jobs." *10th Biennial International Conference & Exposition P*.
- Vavryčuk, Václav. 2014. "Earthquake Mechanisms and Stress Field Václav." *Encyclopedia of Earthquake Engineering* 1–21.
- Wang, Xiaoyang, Mian Chen, Yang Xia, Yan Jin, and Shunde Yin. 2019. "Transient Stress Distribution and Failure Response of a Wellbore Drilled by a Periodic Load." *Energies* 12(18).
- Wijk, Gunnar, and Swedish Defence. 2019. "STRENGTH CRITERIA." *Swedish Defence Research Agency* (January).
- Xu, Hao, Wen Zhou, Runcheng Xie, Lina Da, Christopher Xiao, Yuming Shan, and Haotian Zhang. 2016. "Characterization of Rock Mechanical Properties Using Lab Tests and Numerical Interpretation Model of Well Logs." *Mathematical Problems in Engineering* 2016.
- Zhang, H. Q., D. D. Tannant, H. W. Jing, S. Nunoo, S. J. Niu, and S. Y. Wang. 2015. "Evolution of Cohesion and Friction Angle during Microfracture Accumulation in Rock." *Natural Hazards* 77(1):497–510.
- Zhang, J., W. B. Standifird, K. Adesina, and G. Keaney. 2006. "Wellbore Stability with Consideration of Pore Pressure and Drilling Fluid Interactions." *Proceedings of the 41st U.S. Rock Mechanics Symposium - ARMA's Golden Rocks 2006 - 50 Years of Rock Mechanics* (January 2006).
- Zhang, Jincai. 2011. "Pore Pressure Prediction from Well Logs: Methods, Modifications, and New Approaches." *Earth-Science Reviews* 108(1–2):50–63.
- Zhang, Yushuai, and Jincai Zhang. 2017. "Lithology-Dependent Minimum Horizontal Stress and in-Situ Stress Estimate." *Tectonophysics* 703–704(March):1–8.

## Appendix A: Stress Polygon of Tanuma formation

```

close all
clear all
clc
get(gca,'fontname') % shows you what you are using.
set(gca,'fontname','times') % Set it to times
Sv = 6824; % vertical stress
Pp = 3313; % pore pressure
Fang1 = 32.7;
Fang2 = (Fang1.*pi)./180
mu = tan (Fang2) % coefficient of friction
RHS= (((mu^2)+1)^0.5)+mu).^2 % Right hand side of faulting equations
SHmaxUpperLimit=(RHS.*(Sv-Pp))+Pp
ShminLowerLimitNormalFaulting=((Sv-Pp)./RHS)+Pp
% coefficient values
WBOD=180; % breakout width
WBOR = (WBOD.*pi)./180 % breakout width rad
T0=872; %Rock Strength in Tension
Ucs = 14527; % Effective rock compressive strength.
deltaP = 1104;% Additional pore pressure from drilling mud weight
sigmaDeltaT = 0;% T no thermal stresses
twoTimesThetaB = pi-WBOR
% find where Tensile failure line intersects lower limit of Shmin
lowerSHmaxTensileFailure =(3.*ShminLowerLimitNormalFaulting) - (2.*Pp)...
    - deltaP - T0 - sigmaDeltaT
upperSHminTensileFailure =(SHmaxUpperLimit + (2.*Pp) + deltaP ...
    + T0 + sigmaDeltaT)./3
% now rearrange to solve for Shmin
% % now rearrange to solve for Shmin given SHMax
rightBoundShminBreakouts=-((SHmaxUpperLimit *(1-2.*cos(twoTimesThetaB)))- ...
    (Ucs + 2.*Pp+deltaP + sigmaDeltaT))./(1+2.*cos(twoTimesThetaB)) % now find where
the red and blue lines cross,
shminOfIntersectionRedAndBlue=(((Ucs+2.*Pp + deltaP +sigmaDeltaT)./...
    (1-2.*cos(twoTimesThetaB)))+2.*Pp +deltaP +T0 +sigmaDeltaT).*(1-(3.*(1-
2.*cos(twoTimesThetaB)))+(1+2.*cos(twoTimesThetaB))))
figure (1)
dim1 = [.30 .28 .3 .3];
str1 = 'SSF';
annotation('textbox',dim1,'String',str1,'FitBoxToText','on','fontsize',30,'EdgeColor',
'none');
dim2 = [.27 .07 .3 .3]
str2 = 'NF';
annotation('textbox',dim2,'String',str2,'FitBoxToText','on','fontsize',30,'EdgeColor',
'none');
dim3 = [.6 .45 .3 .3];
str3 = 'RF';
annotation('textbox',dim3,'String',str3,'FitBoxToText','on','fontsize',30,'EdgeColor',
'none');
plot([Sv,Sv], [Sv,upperSHminTensileFailure], 'k-', 'Linewidth', 2);
hold on
plot([ShminLowerLimitNormalFaulting,ShminLowerLimitNormalFaulting],
[lowerSHmaxTensileFailure,ShminLowerLimitNormalFaulting],'k-', 'Linewidth', 2);
hold on
plot([ShminLowerLimitNormalFaulting,upperSHminTensileFailure],
[lowerSHmaxTensileFailure,rightBoundShminBreakouts], 'b--', 'Linewidth', 2);

```

```

hold on
plot([upperSHminTensileFailure,rightBoundShminBreakouts],
[rightBoundShminBreakouts,SHmaxUpperLimit], 'r--', 'Linewidth', 2);
hold on
plot([rightBoundShminBreakouts,SHmaxUpperLimit], [SHmaxUpperLimit,SHmaxUpperLimit],
'k-', 'Linewidth', 2);
hold on
plot([SHmaxUpperLimit,ShminLowerLimitNormalFaulting],
[SHmaxUpperLimit,ShminLowerLimitNormalFaulting], 'k-', 'Linewidth', 2);
hold on
plot([ShminLowerLimitNormalFaulting,ShminLowerLimitNormalFaulting],
[Sv,lowerSHmaxTensileFailure], 'k-', 'Linewidth', 2);
hold on
plot([Sv,ShminLowerLimitNormalFaulting], [Sv,Sv], 'k-', 'Linewidth', 2);
hold on
plot([Sv,Sv], [Sv,SHmaxUpperLimit], 'k-', 'Linewidth', 2);
hold on
plot([ShminLowerLimitNormalFaulting,Sv], [Sv,SHmaxUpperLimit], 'k-', 'Linewidth', 2);
hold on
plot([Sv,rightBoundShminBreakouts], [SHmaxUpperLimit,SHmaxUpperLimit], 'k-',
'Linewidth', 2);
set(gca, 'FontSize',18,'xLim',[2000 30000])
set(gca, 'xTick',2000:2000:30000)
set(gca, 'yLim',[2000 30000])
set(gca, 'yTick',2000:2000:30000)
ax = gca
ax.YAxis.Exponent = 0;
ax.XAxis.Exponent = 0;
xlabel('Sh min (psi)', 'FontSize',24, 'FontWeight', 'bold', 'Color', 'k')
ylabel('SH max (psi)', 'FontSize',24, 'FontWeight', 'bold', 'Color', 'k')

```

[\*Published with MATLAB® R2019b\*](#)

## Appendix B: Stress Polygon of middle shale formation

```

close all
clear all
clc
get(gca,'fontname') % shows you what you are using.
set(gca,'fontname','times') % Set it to times
Sv = 10675; % vertical stress
Pp = 4984; % pore pressure
Fang1 = 37.85;
Fang2 = (Fang1.*pi)./180
mu = tan (Fang2) % coefficient of friction
RHS= (((mu^2)+1)^0.5)+mu).^2 % Right hand side of faulting equations
SHmaxUpperLimit=(RHS.*(Sv-Pp))+Pp
ShminLowerLimitNormalFaulting=((Sv-Pp)./RHS)+Pp
% coefficient values
WBOD=155; % breakout width
WBOR = (WBOD.*pi)./180 % breakout width rad
T0=590; %Rock Strength in Tension
Ucs = 9846; % Effective rock compressive strength.
deltaP = 1661;% Additional pore pressure from drilling mud weight
sigmaDeltaT = 0;% T no thermal stresses
twoTimesThetaB = pi-WBOR
% find where Tensile failure line intersects lower limit of Shmin
lowerSHmaxTensileFailure =(3.*ShminLowerLimitNormalFaulting) - (2.*Pp)...
    - deltaP - T0 - sigmaDeltaT
upperSHminTensileFailure =(SHmaxUpperLimit + (2.*Pp) + deltaP ...
    + T0 + sigmaDeltaT)./3
% now rearrange to solve for Shmin
% % now rearrange to solve for Shmin given SHMax
rightBoundShminBreakouts=-((SHmaxUpperLimit .* (1-2.*cos(twoTimesThetaB))))- ...
    (Ucs + 2.*Pp+deltaP + sigmaDeltaT))./(1+2.*cos(twoTimesThetaB)) % now find where
the red and blue lines cross,
shminOfIntersectionRedAndBlue=(((Ucs+2.*Pp + deltaP +sigmaDeltaT)./...
    (1-2.*cos(twoTimesThetaB)))+2.*Pp +deltaP +T0 +sigmaDeltaT).*(1-(3.*(1-
    2.*cos(twoTimesThetaB)))+(1+2.*cos(twoTimesThetaB))))
figure (1)
dim1 = [.30 .28 .3 .3];
str1 = 'SSF';
annotation('textbox',dim1,'String',str1,'FitBoxToText','on','fontsize',30,'EdgeColor',
'none');
dim2 = [.27 .07 .3 .3]
str2 = 'NF';
annotation('textbox',dim2,'String',str2,'FitBoxToText','on','fontsize',30,'EdgeColor',
'none');
dim3 = [.6 .45 .3 .3];
str3 = 'RF';
annotation('textbox',dim3,'String',str3,'FitBoxToText','on','fontsize',30,'EdgeColor',
'none');
plot([Sv,Sv], [Sv,upperSHminTensileFailure], 'k-', 'Linewidth', 2);
hold on
plot([ShminLowerLimitNormalFaulting,ShminLowerLimitNormalFaulting],
[lowerSHmaxTensileFailure,ShminLowerLimitNormalFaulting],'k-', 'Linewidth', 2);
hold on

```

```

plot([ShminLowerLimitNormalFaulting,upperSHminTensileFailure],
[lowerSHmaxTensileFailure,rightBoundShminBreakouts], 'b--', 'Linewidth', 2);
hold on
plot([upperSHminTensileFailure,rightBoundShminBreakouts],
[rightBoundShminBreakouts,SHmaxUpperLimit], 'r--', 'Linewidth', 2);
hold on
plot([rightBoundShminBreakouts,SHmaxUpperLimit], [SHmaxUpperLimit,SHmaxUpperLimit],
'k-', 'Linewidth', 2);
hold on
plot([SHmaxUpperLimit,ShminLowerLimitNormalFaulting],
[SHmaxUpperLimit,ShminLowerLimitNormalFaulting], 'k-', 'Linewidth', 2);
hold on
plot([ShminLowerLimitNormalFaulting,ShminLowerLimitNormalFaulting],
[Sv,lowerSHmaxTensileFailure], 'k-', 'Linewidth', 2);
hold on
plot([Sv,ShminLowerLimitNormalFaulting], [Sv,Sv], 'k-', 'Linewidth', 2);
hold on
plot([Sv,Sv], [Sv,SHmaxUpperLimit], 'k-', 'Linewidth', 2);
hold on
plot([ShminLowerLimitNormalFaulting,Sv], [Sv,SHmaxUpperLimit], 'k-', 'Linewidth', 2);
hold on
plot([Sv,rightBoundShminBreakouts], [SHmaxUpperLimit,SHmaxUpperLimit], 'k-',
'Linewidth', 2);
set(gca, 'FontSize',18,'xLim',[2000 30000])
set(gca, 'xTick',2000:2000:30000)
set(gca, 'yLim',[2000 30000])
set(gca, 'yTick',2000:2000:30000)
ax = gca
ax.YAxis.Exponent = 0;
ax.XAxis.Exponent = 0;
xlabel('Sh min (psi)', 'FontSize',24, 'FontWeight', 'bold', 'Color', 'k')
ylabel('SH max (psi)', 'FontSize',24, 'FontWeight', 'bold', 'Color', 'k')

```

[Published with MATLAB® R2019b](#)